# Quantifying Atmospheric Trace Element Deposition over the Ocean on a Global Scale with Satellite rainfall products

David Charles Kadko[1], William Michael Landing[2], and Clifton Buck[3]

[1]Florida International University
[2]FloridaStateUniv (USA))
[3]University of Georgia

November 21, 2022

## Abstract

Atmospheric input of trace element micronutrients to the oceans is difficult to determine as even with collection of high-quality aerosol chemical concentrations such data by themselves cannot yield deposition rates. To transform these concentrations into rates, a method of determining flux by applying an appropriate deposition velocity is required. A recently developed method based on the natural radionuclide Be has provided a means to estimate the bulk (wet + dry) deposition velocity (V) required for this calculation. Here, water column Be inventories and aerosol Be concentrations collected during the 2018 US GEOTRACES Pacific Meridional Transect are presented. We use these data together with those from other ocean basins to derive a global relationship between rain rate (m/y) and bulk depositional velocity (m/d), such that V= 999±96 x Rain rate + 1040±136 (R=0.81). Thus with satellite -derived rainfall estimates, a means to calculate aerosol bulk deposition velocities is provided.

## Hosted file

`supplementary table1.docx` available at https://authorea.com/users/528722/articles/596926-quantifying-atmospheric-trace-element-deposition-over-the-ocean-on-a-global-scale-with-satellite-rainfall-products

# Quantifying Atmospheric Trace Element Deposition over the Ocean on a Global Scale with Satellite rainfall products

David Kadko[1], William Landing[2], Clifton Buck[3]

[1] Florida International University, Applied Research Center, Miami, FL, USA
[2] Department of Earth, Ocean and Atmospheric Science, Florida State University, Tallahassee, FL, USA
[3] Skidaway Institute of Oceanography, University of Georgia, Savannah, GA, USA

**Corresponding author: David Kadko (dkadko@fiu.edu)**

Key Points:

1. Aerosol input of trace element micronutrients is difficult to determine as aerosol chemical concentration alone cannot yield deposition rate

2. The natural radionuclide $^{7}$Be provides a means to estimate the bulk deposition velocity ($V_b$) required for this calculation

3. We use new $^{7}$Be data from the Pacific with data from other ocean basins to derive a global relationship between rain rate and $V_b$

Key words

Trace elements, GEOTRACES, aerosols, bulk deposition velocity

**Abstract**

Atmospheric input of trace element micronutrients to the oceans is difficult to determine as even with collection of high-quality aerosol chemical concentrations such data by themselves cannot yield deposition rates. To transform these concentrations into rates, a method of determining flux by applying an appropriate deposition velocity is required. A recently developed method based on the natural radionuclide $^{7}$Be has provided a means to estimate the bulk (wet + dry) deposition velocity ($V_b$) required for this calculation. Here, water column $^{7}$Be inventories and aerosol $^{7}$Be concentrations collected during the 2018 US GEOTRACES Pacific Meridional Transect are presented. We use these data together with those from other ocean basins to derive a global relationship between rain rate (m/y) and bulk depositional velocity (m/d), such that $V_b$ = 999±96 x Rain rate + 1040±136 ($R^2$=0.81). Thus with satellite -derived rainfall estimates, a means to calculate aerosol bulk deposition velocities is provided.

**Plain Language Summary**

Atmospheric input of trace element micronutrients to the global ocean such as iron (Fe), cobalt (Co) and Zinc (Zn) is difficult to determine. Even with collection of high-quality aerosol chemical concentrations such data by themselves cannot yield rates of deposition. A recently developed method based on the natural radionuclide $^{7}$Be which is deposited to the surface ocean has provided a means to estimate the bulk (wet + dry) deposition velocity ($V_b$) required for this calculation. In this work, water column $^{7}$Be inventories and aerosol $^{7}$Be concentrations collected during the 2018 US GEOTRACES Pacific Meridional Transect are presented. We use these data together with those from other ocean basins to derive a global relationship between rain rate (m/y) and bulk depositional velocity (m/d), such that $V_b$ = 999xRain rate + 1040 (R2=0.81). Thus given a global rain product, a means to estimate deposition velocities based on rainfall is provided. This information is a critical for evaluating limitations on phytoplankton growth and the strength of the Biological Carbon Pump, and represents an important input to ocean biogeochemical models.

## 1. INTRODUCTION

As the base of most marine food webs, phytoplankton productivity affects growth and success at all other trophic levels in the oceans. Phytoplankton growth rates are controlled in part by macro and micronutrient supply rates, which in turn are controlled by physical environmental factors (atmospheric deposition, vertical mixing, upwelling, and horizontal advection) which vary over (and often define) different oceanic regimes. The magnitude of these fluxes will therefore vary significantly across ocean basins (e.g. Buck et al., 2019; Kadko et al., submitted). The Biological Carbon Pump (BCP), one of the

dominant mechanisms for sequestering atmospheric carbon to the deep ocean (Volk and Hoffert, 1985), is related to the interplay between different limiting factors such as the concentrations of available macronutrients (silicon, Si; phosphorus, P; nitrogen, N) and essential micronutrients like manganese (Mn), iron (Fe), cobalt (Co), nickel (Ni), copper (Cu), zinc (Zn), and cadmium (Cd). Understanding the factors that control the sources and distributions of bioactive trace elements (TEs) is crucial for predicting their effects on the BCP.

Atmospheric input to the oceans can be significant for many chemical species (e.g., Duce et al., 1991; Prospero, 1996, 2002). TE micronutrients delivered to the open ocean by dust deposition may, in some areas, relieve TE limitation on phytoplankton growth and promote nitrogen fixation (e.g. Martin et al., 1990, Coale et al., 1996; Falkowski, 1997; Falkowski et al., 1998; Moore et al., 2009; 2013; Krishnamurthy et al., 2009; Jickells et al., 2014; Baker and Jickells, 2016; Okin et al. 2011) and can play an important role in controlling biogeochemical processes in the ocean (e.g. Morel et al., 2003; Morel and Price, 2003). For these reasons, considerable effort has been made to evaluate the supply of dust to the ocean (e.g. Anderson et al., 2016; Baker et al., 2016) including consideration of dust supply in global biogeochemical models (e.g. Mahowald et al., 2005; Tagliabue et al., 2009; 2015).

Despite these efforts, the determination of the dust flux, particularly in remote ocean regions, is difficult (Anderson et al., 2016; Baker et al., 2016). While direct collection of atmospheric aerosols is relatively straightforward there is limited availability of island sampling locations and limited time that aerosols can be collected during a research cruise. Furthermore, even with high-quality aerosol chemical concentrations obtained from shipboard or land-based aerosol samples, such concentration data by themselves cannot yield the deposition rate of TEs. To transform these concentrations into rates, a method of determining flux by applying an appropriate deposition velocity is required. Similarly, models may be inaccurately configured (or "poorly constrained") regarding the parameterization of atmospheric deposition processes. If such parameters could be accurately assessed, then the chemical concentrations in aerosol samples could be converted into actual estimates of flux.

A recently developed method based on the natural radionuclide $^{7}$Be (half-life 53.3 days), has shown promise as a way to estimate atmospheric deposition fluxes (Kadko et al., 2015). This method has been used to derive TE atmospheric fluxes for sites in the Atlantic (Kadko et al., 2015; Anderson et al., 2016; Shelley et al., 2017), the Pacific (Buck et al., 2019; Kadko et al., submitted) and the Arctic (Kadko et al., 2016; 2019; Marsay et al., 2018) oceans. $^{7}$Be is produced in the upper atmosphere from cosmic ray spallation, quickly attaches to aerosol particles, and is transported to the lower troposphere by atmospheric mixing processes and removed mainly by precipitation. In this work, water column $^{7}$Be inventories and aerosol $^{7}$Be concentrations collected during the 2018 US GEOTRACES Pacific Meridional Transect (PMT; GEOTRACES section GP15) are presented. We use these data together with

data from other ocean basins to derive a global relationship between rain rate and aerosol bulk deposition velocity. Thus given a global rain product, a means to estimate deposition velocities based on rainfall is provided.

## 2. Background

The bulk flux for aerosol TEs ($F_{TE}$) is estimated from the concentration of trace elements in aerosols ($C_{TE}$) and the bulk deposition velocity ($V_b$) which includes dry + wet deposition, such that

$$F_{TE} = V_b \times C_{TE} \qquad \text{Eqn. 1}$$

Based on $^7$Be, $V_b$ can be derived from:

$$V_b = \frac{[\,^7\text{Be flux}\,]}{(^7\text{Be})_{aerosol}} \qquad \text{Eqn. 2}$$

Furthermore, it has been shown that the integrated rate of decay of $^7$Be in the upper ocean (i.e. the $^7$Be inventory in the water column multiplied by the radioactive decay constant for $^7$Be) is equal to its flux to the ocean by wet and dry deposition (Aaboe et al., 1981; Kadko and Prospero, 2011; Kadko et al., 2015; Kadko et al., 2019) under steady-state conditions, such that:

$$V_b = (\text{Inventory } ^7\text{Be} \times \lambda) / (^7\text{Be})_{aerosol} \qquad \text{Eqn. 3}$$

where $\lambda$ is the $^7$Be decay constant (0.013 $d^{-1}$). This observation provides a key linkage between the atmospheric concentrations of chemical species and their deposition to the oceans; the flux from the atmosphere to the surface ocean of any material having a deposition velocity similar to that of $^7$Be can be calculated from its atmospheric concentration and the $^7$Be-derived bulk deposition velocity (Young and Silker, 1980).

This method was tested at the BATS (Bermuda Atlantic Time Series) site in the Sargasso Sea (Kadko et al., 2015), where TE fluxes based on the $^7$Be method were compared with 24 months of continuous aerosol and rainfall sampling at the BIOS (Bermuda Institute of Ocean Sciences) station on Bermuda. The atmospheric fluxes of total aerosol TEs (Fe, Mn, Co, Ni, Cu, Zn, Cd, and Pb), calculated using the bulk deposition velocity determined from the $^7$Be data, were comparable (50% to 95%) to fluxes derived from measured wet deposition plus estimated dry deposition (assuming $V_d$ = 1000m/day) for samples collected on Bermuda. This method was also tested during the 2015 US Arctic GEOTRACES cruise by comparing $^7$Be-derived TE fluxes to the measured TE accumulation in recently deposited snow.

Given the variability in snow and aerosol TE concentration observed over the expedition, and the limited timescale of the observations, agreement between the two methods was reasonable.

Because it is associated with sub-micrometer aerosols, the deposition of aerosol $^{7}$Be is dominated by rainfall scavenging, and it has been observed that $^{7}$Be deposition rates correlate with the rate of precipitation (e.g. Young and Silker, 1980; Olsen et al., 1985; Uematsu et al., 1994; Kim et al., 1999; Kadko and Prospero, 2011; Peng et al., 2019). The $^{7}$Be-derived bulk deposition velocity from the Arctic (low rainfall region) was 1190 m/d (Kadko et al 2016; 2019) and from Bermuda (high rainfall region) was 2600 m/d (Kadko et al., 2015). These are plotted against rain-fall rate in Supplemental Figure 1. Obviously, a trend cannot be based on only two points, but the zero-rainfall intercept does correspond to the dry deposition velocity of 1000 m/d generally assumed for dust (e.g. Duce et al., 1991). These results are suggestive of a relationship between $V_b$ and rain rate that will be further explored here.

## 3. Study area and Methods

The US GEOTRACES Pacific Meridional Transect (PMT, cruise GP15) was carried out on the R/V Roger Revelle from September 25 to November 25, 2018. The cruise mainly followed a north-to-south track along 152° W between Alaska and Tahiti (Figure 1), designed to examine, among other things, the influence of strong margin chemical fluxes, atmospheric dust deposition, oxygen minimum zones, equatorial upwelling, and some of the lowest-nutrient waters in the world ocean in the South Pacific gyre at 20°S. This transect crossed large gradients in rain rate (Figure 1) affording an opportunity to test the $V_b$ and rain rate relationship.

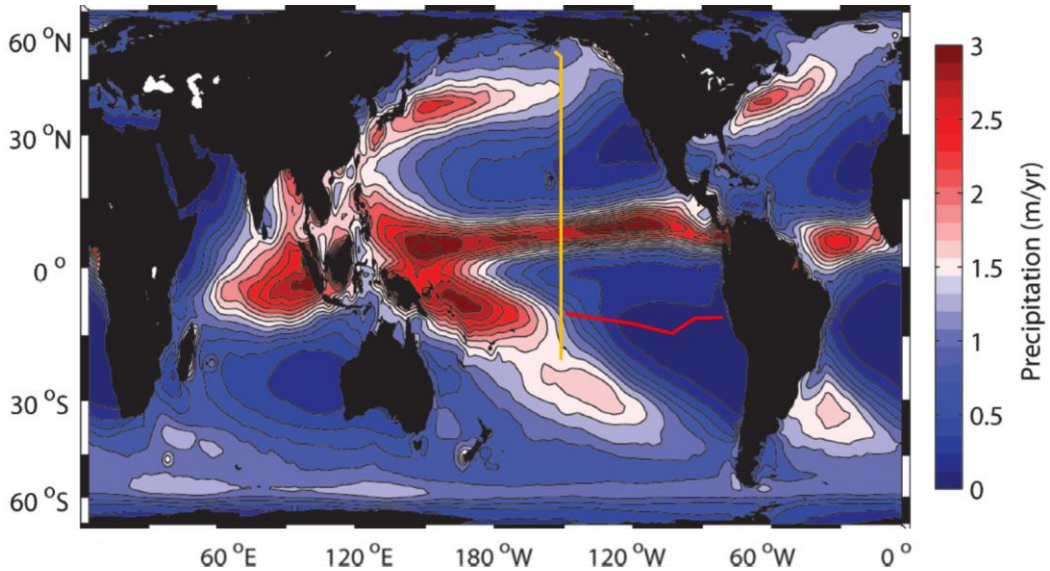


Figure 1. The track (yellow line) of the 2018 GEOTRACES PMT (GP15) cruise superimposed over a climatological map of precipitation, from Schanze et al. (2010). Also shown is the track (red line) of the 2013 GEOTRACES GP16 (East Pacific Zonal Transect; Kadko et al., submitted)

**3.1. $^{7}$Be water column analysis**: Details of sample collection are described in Kadko (2017). Briefly, samples were collected at selected depths by pumping 400–700 L of seawater via a ~4 cm hose into large plastic barrels on deck. From these barrels, the seawater was then pumped through iron impregnated acrylic fibers at ~10 L/min to extract the $^{7}$Be from seawater (Lal et al., 1988; Krishnaswami et al., 1972; Lee et al., 1991). On land, the fibers were dried and then ashed. The ash was subsequently pressed into a pellet (5.8 cm diameter) and placed on a low background germanium gamma detector. The isotope $^{7}$Be has a readily identifiable gamma peak at 478 keV. The detector was calibrated for the pellet geometry by adding a commercially prepared mixed solution of known gamma activities to an ashed fiber, pressing the ash into a pellet, and counting the activities to derive a calibration curve. The uncertainty of the extraction efficiency (4%) and the detector efficiency (2%) was in all cases smaller than the statistical counting error and the uncertainty in the blank.

**3.2. Aerosol $^{7}$Be**: Details of the aerosol collection methods are presented in Buck et al., (2019). Briefly, bulk aerosol samples were collected on 12-replicate acid-washed 47 mm Whatman 41(W41) ash-less filter discs mounted in Advantec-MFS polypropylene inline filter holders (PP47). When the wind was directed from the bow, air was pumped through the filters using a high-volume aerosol sampler (model 5170V-BL, Tisch Environmental) at approximately 100 L min$^{-1}$ through each filter. The sampler was mounted on the forward rail of the 03-deck approximately 16 m above sea level and forward of both the ship's superstructure and exhaust stacks. Each collection period lasted approximately three days. For $^{7}$Be, Whatman-41 aerosol filters were stacked three-high in a plastic Petri dish and counted by gamma spectroscopy. This configuration was calibrated with a commercially prepared mixed solution of known gamma activities.

**3.3. Rainfall analysis.** Rainfall data was derived from the Global Precipitation Climatology Project (GPCP). The GPCP monthly product provides a consistent analysis of global precipitation from an integration of various satellite data sets over land and ocean and gauge data from land sites http://gpcp.umd.edu/. The rainfall rates used in the following discussions were based on the weighted average at each location which included the rain rate for the month of sampling, and the prior three months each diminished by an exponential term containing the decay constant of $^{7}$Be; that is, weighted against the decay lifetime of $^{7}$Be deposited during each month.

$$\text{Average rain rate} = \Sigma\, RR_i \cdot f_i \exp(-\lambda t_i) / \Sigma\, f_i \exp(-\lambda t_i) \qquad \text{Eqn. 4}$$

where $RR_i$ is the rainfall rate for month (i) taken from the GPCP data set, $f_i$ ($0 \leq f_i \leq 1$) is the fraction of the month during the month of sampling (e.g. November 15 corresponds to f = 0.5), and $t_i$ is the time in days between the sampling date and any previous monthly rain (i).

## 4.0 Results and Discussion

Water column $^{7}$Be activities are presented in Supplemental Table 1. The $^{7}$Be inventories are shown in Table 1 and plotted against latitude with the weighted average rainfall rates (Eqn. 4) in Figure 2a. The gradients in the climatological rain rates from Figure 1 are reflected in those of the cruise with the peak in rainfall corresponding to the Intertropical Convergence Zone (ITCZ). Generally the $^{7}$Be inventories follow the trend in rainfall, the exception occurring at the zone of equatorial upwelling. There, the observed $^{7}$Be inventory does not reflect atmospheric input, but rather upwelling of deep, $^{7}$Be-deficient water. This observation has been used to derive upwelling rates (Kadko and Johns, 2011; Haskell et al., 2014; Kadko, 2017). In Figure 2b, the $^{7}$Be inventories are plotted against rain rate. The two parameters are correlated, with higher inventories occurring within zones of high rainfall. The $^{7}$Be inventories at upwelling stations fall well below the trendline.

**Table 1. $^{7}$Be Data from the PMT (GP15) cruise**

| **Water column $^{7}$Be inventories** | | | **Aerosol $^{7}$Be Activities** | | |
|---|---|---|---|---|---|
| station | Lat ($^{0}$N) | $^{7}$Be Inventory (dpm/m$^{2}$) | Aerosol Deployment | Latitude (sample midpoint) | $^{7}$Be Activity (dpm/m$^{3}$) |
| 4 | 54.66 | 23390 | 3 | 54.9 | 0.0184±0.0066 |
| 5 | 53.68 | 21520 | 4 | 53.3 | 0.0366±0.0015 |
| 6 | 52.0 | 24750 | 1 | 49.5 | 0.0622±0.0094 |
| 8 | 47.0 | 25460 | 5 | 51.1 | 0.1567±0.0054 |
| 10 | 42.0 | 22580 | 6 | 45.75 | 0.2660±0.0079 |
| 12 | 37.0 | 22470 | 7 | 43.25 | 0.2935±0.0089 |
| 14 | 32.0 | 22460 | 8 | 39.5 | 0.1232±0.0053 |
| 16 | 27.0 | 19980 | 9 | 35.75 | 0.2730±0.0076 |
| 18 | 22.0 | 15860 | 10 | 33.25 | 0.1818±0.0073 |
| 19 | 17.5 | 21900 | 11 | 29.5 | 0.2770±0.0083 |
| 21 | 11.0 | 18240 | 12 | 24.5 | 0.1754±0.0075 |
| 23 | 7.5 | 29830 | 13 | 18.1 | 0.0975±0.0106 |
| 25 | 5.0 | 28880 | 14 | 14.25 | 0.0792±0.0084 |
| 27 | 2.5 | 15550 | 15 | 8.8 | 0.0413±0.0046 |
| 29 | 0 | 4015 | 16 | 5.725 | 0.0984±0.0059 |
| 31 | -2.5 | 8020 | 17 | 3.45 | 0.1848±0.0079 |
| 33 | -5.0 | 1730 | 18 | 0.415 | 0.1373±0.0053 |
| 35 | -10.5 | 16640 | 19 | -3.1 | 0.1222±0.0105 |
| 37 | -15 | 21610 | 20 | -7.75 | 0.1492±0.0074 |
| 39 | -20 | 23320 | 21 | -12.75 | 0.1080±0.0076 |
| | | | 22 | -17.5 | 0.1482±0.0066 |
| | | | 23 | -19.6 | 0.2147±0.0133 |

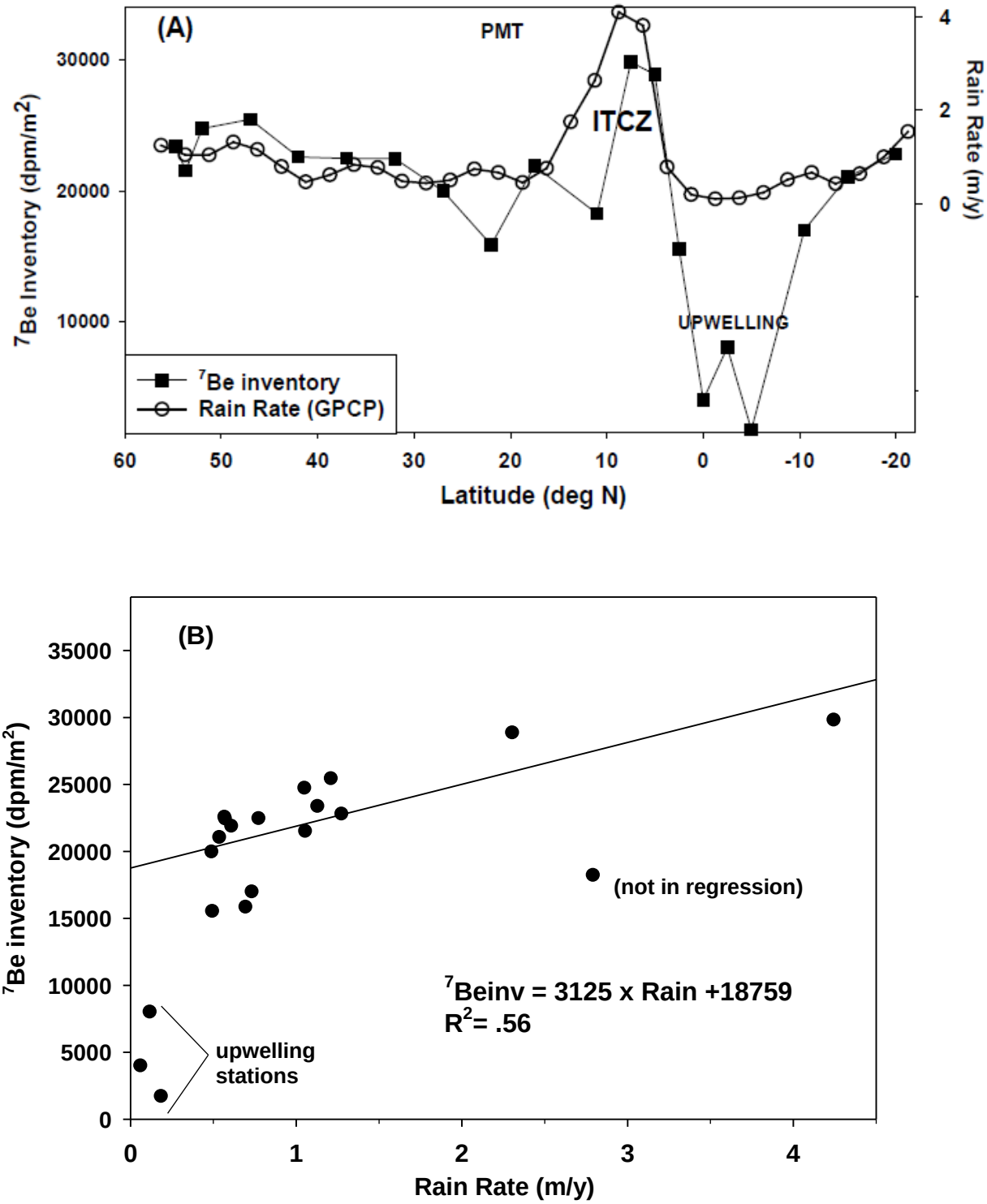


Figure 2. (A) The $^7$Be inventories (squares) and the weighted average rain rate (circles) plotted against latitude for the PMT transect. The locations of the ITCZ and upwelling region are indicated. (B) The $^7$Be inventories plotted against rain rate. The upwelling stations fall well below the trendline.

The $^{7}$Be aerosol activities are shown in Table 1 and plotted against latitude with the weighted average rain rate (Eqn. 4) in Figure 3a. There is no obvious relationship between the $^{7}$Be aerosol activities and the rain rate with the exception of aerosols collected within the ITCZ. There the persistent high rainfall maintains a low aerosol $^{7}$Be activity (e.g. Feely et al, 1989). This is shown in Figure 3b, where in a plot of $^{7}$Be aerosol concentration against rain rate the ITCZ samples represent a separate relationship from the other samples. The average $^{7}$Be aerosol activity of the three ITCZ samples is 0.073 ± 0.029 dpm/m$^{3}$, and that for the other 19 samples is 0.157 ± 0.075 dpm/m$^{3}$.

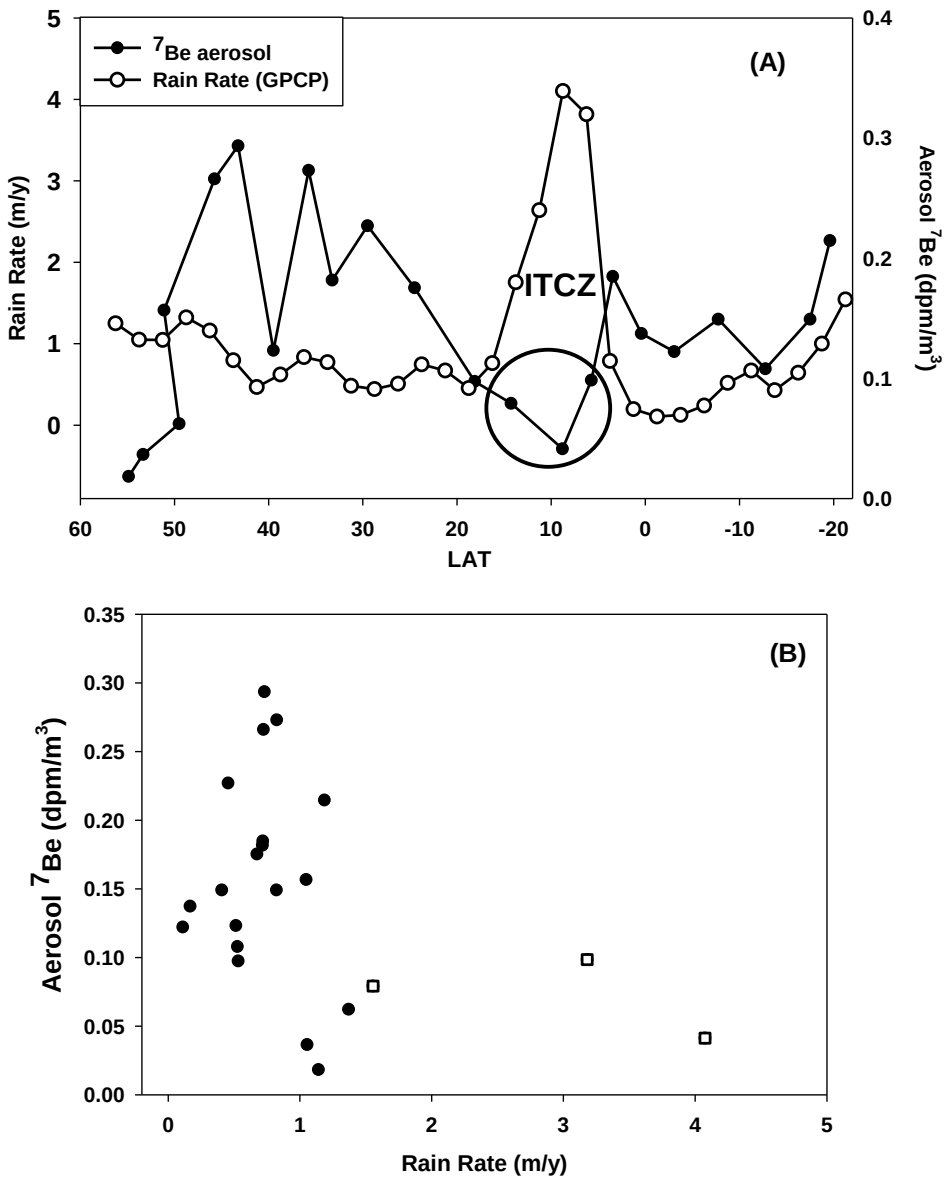


Figure 3. (A) The $^{7}$Be aerosol activities (black circles) and weighted average rain rate (open circles) plotted against latitude for the PMT cruise track. The location of the ITCZ is indicated and aerosol samples collected within the ITCZ are circled. (B) The $^{7}$Be aerosol activities plotted against rain rate. The aerosol samples collected within the ITCZ are indicated (open squares).

To derive the bulk deposition velocities ($V_b$), the $^7$Be inventories (Table 1) are combined with the aerosol $^7$Be activities (Eqn. 3; Table 1). The $^7$Be inventories integrate deposition over the mean life (77 days) of the isotope, and the rain rate is based on monthly averages. However, each aerosol sample is collected over a period of only several days, and atmospheric transport is temporally and spatially sporadic such that variability in aerosol $^7$Be activity rather than variability in the upper ocean inventory would drive variability in $V_b$. For this reason we use an average aerosol $^7$Be activity rather than the "snapshot" aerosol observations to calculate the bulk deposition velocities. Values of $V_b$ derived in this manner for the PMT cruise are plotted against rain rate in Figure 4. Across the PMT transect $V_b$ and rainfall are well correlated ($R^2$=0.81), and the results from Bermuda and the Arctic Ocean (Kadko et al., 2015; Kadko et al., 2016; 2019) fall on the PMT trendline.

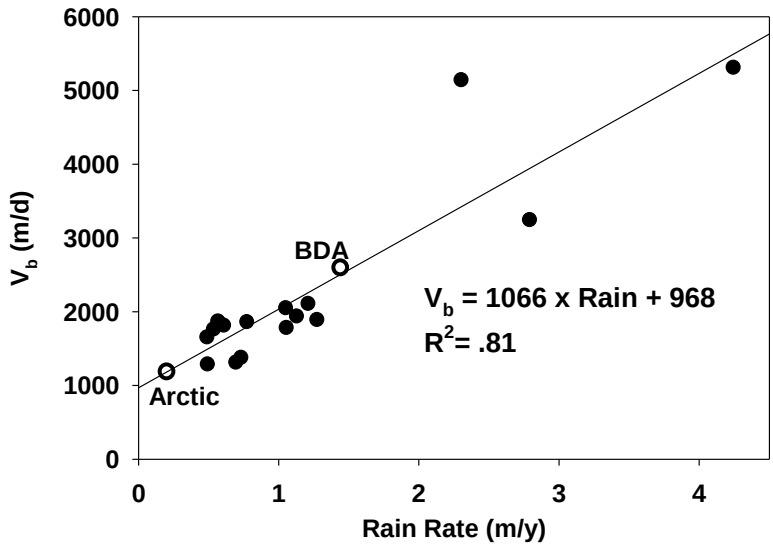


Figure 4. The bulk deposition velocity ($V_b$) plotted against rain rate for the PMT transect (black symbols). The Bermuda and Arctic results are shown for comparison.

The $^7$Be inventories from this work (PMT) are plotted with those from several earlier studies, against rainfall in Figure 5a. The general trend of increasing inventory with rainfall is observed. Dividing these data by the approriate aerosol $^7$Be concentrations yields a set of $V_b$ values that are plotted against rain rate in Figure 5b. A high correlation between $V_b$ and rain rate is observed across several ocean basins. Scatter in the inventory plot (Fig 5a) is reduced in Figure 5b as high inventories (e.g. Bermuda), are driven by high aerosol concentration, while low inventories (e.g. Arctic) are driven by low aerosol concentrations. The resulting relationship is

$$V_b \text{ (m/d)} = 999\pm96 \text{ x RainRate} + 1040\pm136 \qquad \text{Eqn. 5}$$

The y- intercept indicates a dry deposition velocity of 1040 m/d.

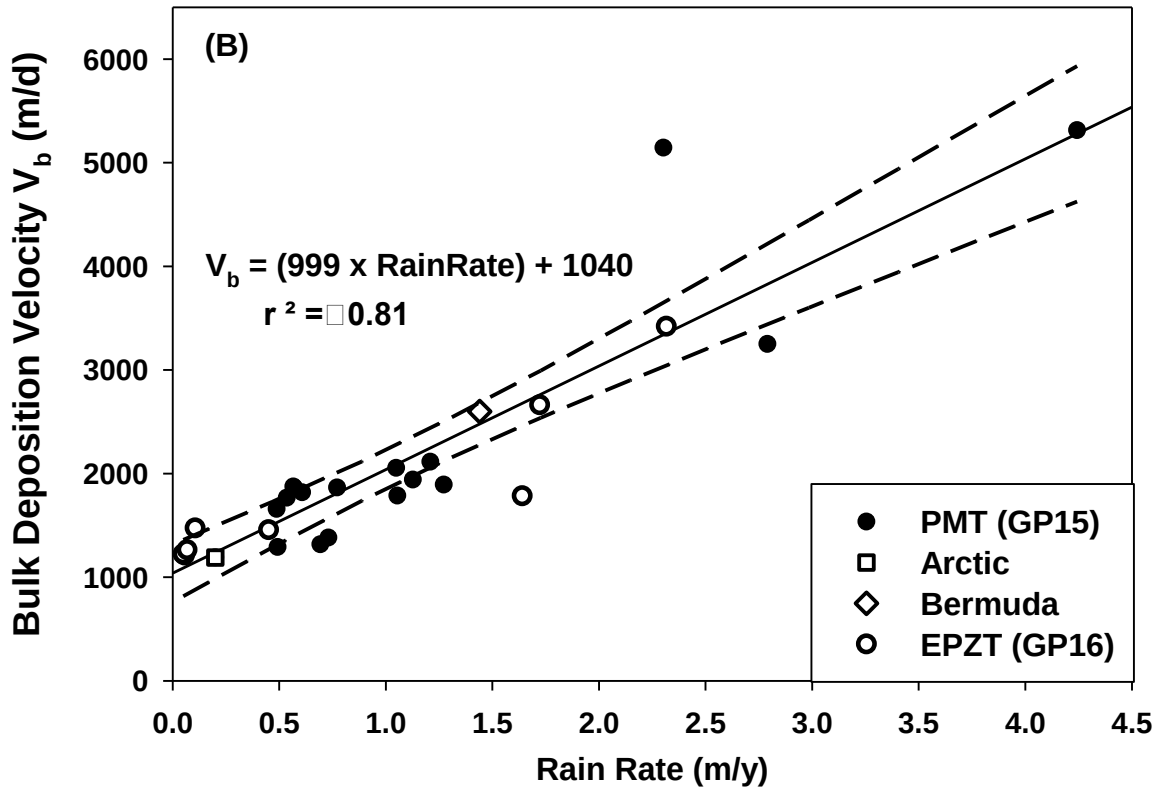


Figure 5 (A). The $^{7}$Be inventories plotted against rain rate for the PMT cruise (black circles); the EPZT (open circles, Kadko et al., in review); Bermuda (diamond, Kadko et al.; 2015) and the Arctic (square, Kadko et al., 2016; 2019). B) $V_b$ plotted against rain rate for these same locations. The upper and lower 95% confidence intervals (dashed lines) around the linear regression trend line are shown.

**5.0 Conclusions**

In this work, ocean $^{7}$Be inventories and aerosol $^{7}$Be concentrations collected during the GEOTRACES Pacific Meridional Transect were used with data from other ocean basins to derive a global relationship between rainfall rate (m/y) and aerosol bulk deposition velocity (m/d), where $V_b$ = 999±96 x Rain rate + 1040±136 ($R^2$=0.81). Future work can further test whether the bulk deposition velocities derived using this relationship, based on aerosol $^{7}$Be, can be used to reliably calculate the fluxes of other TEs. This has been tested at Bermuda and the Arctic with good success. With this relationship, the fluxes of soluble aerosol bioactive elements to the surface ocean can be calculated by multiplying the aerosol bulk deposition velocities times the aerosol TE concentrations and solubilities, (e.g. Buck et al., 2019; Kadko et al., 2019). This information is critical for evaluating limitations on phytoplankton growth and the strength of the Biological Carbon Pump, and represents an important constraint on ocean biogeochemical models.

**Acknoweldgements**

This work was upported by NSF grants OCE-1736319 to DK, OCE-1756104 to WML, and OCE-1756103to CSB. Data have been submitted to the Biological and Chemical Oceanography Data Management Office (BCO-DMO) (https://www.bco-dmo.org/dataset/781794 and https://www.bco-dmo.org/dataset/781806) and will appear in future GEOTRACES data products. We thank Drs. Mark Stephens and Chris Marsay for their technical assistance.

**References**

Anderson, R. F., H. Cheng, R. L. Edwards, M. Q. Fleisher, C. T. Hayes, K.-F. Huang, D. Kadko, P. J. Lam, W. M. Landing, Y. Lao, Y. Lu, C. I. Measures, P. L. Morton, S. B. Moran, D. C. Ohnemus, L. F. Robinson, R. U. Shelley (alphabetical order) (2016), How well can we quantify dust deposition to the ocean? Philosophical Transactions of the Royal Society A 374, DOI: 10.1098/rsta.2015.0285.

Baker, A.R. and T.D. Jickells. (2016). Atmospheric deposition of soluble trace elements along the Atlantic Meridional Transect (AMT). Prog. Oceanogr. doi:10.1016/j.pocean.2016.10. 002.

Baker A. R., Landing W. M., Bucciarelli E., Cheize M., Fietz S., Hayes C. T., Kadko D., Morton P. L., Rogan N., Sarthou G., Shelley R. U., Shi Z., Shiller A. and van Hulten M. M. P. (2016). Trace element and isotope deposition across the air–sea interface: progress and research needs. Philosophical Transactions of the Royal Society A: Mathematical, Physical and Engineering Sciences. http://doi.org/10.1098/rsta.2016.0190.

Buck., C.S., A. Aguilar-Islas, C. Marsay, D. Kadko and W. Landing (2019) Trace element concentrations, elemental ratios, and enrichment factors observed in aerosol samples collected during the US GEOTRACES eastern Pacific Ocean transect (GP16). Chem. Geo., 511, 212-224.

Coale K.H., K.S. Johnson, S.E. Fitzwater, R. M. Gordon, S. Tanner, F. P. Chavez, L. Ferioli, C. Sakamoto, P. Rogers, F. Millero, P. Steinberg, P. Nightingale, D. Cooper, W. P. Cochlan, M. R. Landry, J.Constantinou, G. Rollwagen, Trasvina A. and R. Kudela. (1996) A massive phytoplankton bloom induced by an ecosystem-scale iron fertilization experiment in the equatorial Pacific Ocean. Nature 383, 495 - 501; doi:10.1038/3834

Duce, R.A., P. S. Liss J. T. Merrill E. L. Atlas P. Buat, Menard B. B. Hicks J. M. Miller J. M. Prospero R. Arimoto T. M. Church W. Ellis J. N. Galloway L. Hansen T. D. Jickells A. H. Knap K. H. Reinhardt B. Schneider A. Soudine J. J. Tokos S. Tsunogai R. Wollast M. Zhou. (1991). The atmospheric input of trace species to the world ocean. Global Biogeochem. Cycles 5, 193-259, doi:10.1029/91GB01778.

Falkowski, P. (1997) Evolution of the nitrogen cycle and its influence on the biological sequestration of CO2 in the ocean, Nature 387, 272 - 275, doi:10.1038/387272a0.

Falkowski, P.G., R.T. Barber, and V. Smetacek (1998) Biogeochemical controlsand feedbacks on ocean primary production. Science 281, 200-206.

Feely, H.W., R. J. Larsen & C, G. Sanderson (1989) Factors That Cause Seasonal Variations in Beryllium-7 Concentrations in Surface Air. I. Environ. Radioactivity 9, 223-249

Haskell W.Z., D. Kadko, D.E. Hammond, M.G. Prokopenko, W.M. Berelson, A.N. Knapp and D. Capone (2015) Upwelling velocities and eddy diffusivity from 7Be measurements used to compare vertical nutrient fluxes to export POC flux in the Eastern Tropical South Pacific. Marine Chemistry. doi:10.1016/j.marchem.2014.10.004. 168, 140–150.

Jickells, T.D., P. Boyd, K.A. Hunter. (2014). Biogeochemical impacts of dust on the global carbon cycle. In: Knippertz, P., Struut, J.-B.W. (Eds.), Mineral Dust. Springer Heidelberg

Kadko, D., and J. Prospero (2011), Deposition of 7Be to Bermuda and the regional ocean: Environmental factors affecting estimates of atmospheric flux to the ocean, J. Geophys. Res., 116, C02013, doi:10.1029/2010JC006629.

Kadko, D., and W. Johns (2011) Inferring upwelling rates in the equatorial Atlantic using 7Be measurements in the upper ocean. Deep-Sea Res. I, 58, 247-257, doi:10.1016/j.dsr.2011.03.004

Kadko D., W. M. Landing, and R. U. Shelley (2015) A novel tracer technique to quantify the atmospheric flux of trace elements to remote ocean regions. Journ. Geophy. Res. Oceans, 119, doi:10.1002/2014JC010314.

Kadko D., B. Galfond, W. M. Landing, and R. U. Shelley (2016) Determining the Pathways, Fate, and Flux of Atmospherically Derived Trace Elements in the Arctic Ocean/Ice System. Marine Chemistry. 182, 38-50, doi:10.1016/j.marchem.2016.04.006.

Kadko, D. (2017) Upwelling and Primary Production during the U.S. GEOTRACES East Pacific Zonal Transect. Global Biogeochem. Cycles. 31, doi:10.1002/2016GB005554.

Kadko D., A. Aguilar-Islas, C. Bolt, C.S. Buck, J. N. Fitzsimmons, L. T. Jensen, W.M. Landing, C.M. Marsay, R. Rember, A. M. Shiller, L. M. Whitmore, and R. F. Anderson (2019) The residence times of trace elements determined in the surface Arctic Ocean during the 2015 US Arctic GEOTRACES expedition. Mar. Chem. 208, 56-69. doi.org /10.1016/ j.marchem. 2018.10.011.

Kadko, D., A. Aguilar-Islas, C. S. Buck, J. N. Fitzsimmons, W. M. Landing, A. Shiller, C.P. Till, K.W. Bruland, E.A. Boyle, R.F. Anderson (in review) Sources, Fluxes and Residence Times of Trace Elements measured during the U.S. GEOTRACES East Pacific Zonal Transect. Mar Chem.

Kim, G., L. Alleman, and T. Church (1999) Atmospheric depositional fluxes of trace elements, $^{210}$Pb and $^{7}$Be into the Sargasso Sea. Global Biogeochem. Cycles, 13, 1183-1192.

Krishnamurthy A., J.K. Moore, N. Mahowald, C. Luo, S.C. Doney, K. Lindsay and C. S. Zender. (2009). Impacts of increasing anthropogenic soluble iron and nitrogen deposition on ocean biogeochemistry. Global Biogeochemical Cycles, 23, doi:10.1029/2008GB003440.

Mahowald, N. M., A. R. Baker, G. Bergametti, N. Brooks, R. A. Duce, T. D. Jickells, N. Kubilay, J. M. Prospero, and I. Tegen (2005), Atmospheric global dust cycle and iron inputs to the ocean, Global Biogeochem. Cycles,19, GB4025,doi:10.1029/2004GB002402.

Marsay, C.M., D. Kadko, W. M. Landing, P. L. Morton, B.A. Summers and C. S. Buck (2018) Concentrations, provenance and flux of aerosol trace elements during US GEOTRACES Western Arctic cruise GN01, Chem. Geol., 502, 1-14.

Martin, J.H., S. E. Fitzwater and R. M. Gordon. (1990). Iron deficiency limits phytoplankton growth in Antarctic waters, Global Biogeochem. Cycl., 4: 5-12.

Moore, C.M., et al. 2009 Large-scale distribution of Atlantic nitrogen fixation controlled by iron availability. *Nature Geoscience* **2**, 867-871.

Moore, C.M., et al. 2013 Processes and patterns of oceanic nutrient limitation. *Nature Geoscience* **6**, 701-710.

Moore, J.K., S.C. Doney, D.M. Glover, and I.Y. Fung 2002 Iron cycling and nutrient-limitation patterns in surface waters of the World Ocean. *Deep-Sea Research Part II-Topical Studies in Oceanography* **49**, 463-507.

Morel, F.M.M. and Price, N.M. (2003). The biogeochemical cycles of trace metals in the oceans. Science, 300: 944-947.

Morel, F.M.M., Milligan, A.J. and Saito, M.A., (2003). Marine bioinorganic chemistry: The role of trace metals in the oceanic cycles of major nutrients. In The Oceans and Marine Geochemistry. Treatise on Geochemistry (ed. H. Elderfield), pp. 113-143.Oxford: Elsevier.

Okin, G.S., et al. 2011 Impacts of atmospheric nutrient deposition on marine productivity: Roles of nitrogen, phosphorus, and iron. *Global Biogeochemical Cycles* **25**.

Olsen, C.R., Larsen, I.L., Lowry, P.D., Cutshall, N.H., Todd, J.F., (1985). Atmospheric fluxes and marsh-soil inventories of 7Be and 210Pb. J. Geophys. Res. 90 (10), 487–495.

Peng, A., G. Liu, Z. Jiang, G. Liu, M. Liu (2019) Wet depositional fluxes of 7Be and 210Pb and their influencing factors at two characteristic cities of China. Applied Radiation and Isotopes, 147, 21-30.

Prospero J.M. (1996) Saharan Dust Transport Over the North Atlantic Ocean and Mediterranean: An Overview. In: Guerzoni S., Chester R. (eds) The Impact of Desert Dust Across the Mediterranean. Environmental Science and Technology Library, vol 11. Springer, Dordrecht.

Prospero J.M. (2002) The Chemical and Physical Properties of Marine Aerosols: An Introduction. In: Gianguzza A., Pelizzetti E., Sammartano S. (eds) Chemistry of Marine Water and Sediments. Environmental Science. Springer, Berlin, Heidelberg.

Schanze, J.J., R. W. Schmitt, and L. L. Yu (2010) The global oceanic freshwater cycle: A state-of-the-art quantification. Journal of Marine Research, 68, 569–595.

Shelley, R.U., M. Roca-Martí, M.Castrillejo, V. Sanial, P. Masqué., W. M. Landing, P. van Beek, H. Planquette, G. Sarthou (2017) Quantification of trace element atmospheric deposition fluxes to the Atlantic Ocean ( > 40°N; GEOVIDE, GEOTRACES GA01) during spring 2014.

Tagliabue, A., L. Bopp, O. Aumont (2009) Evaluating the importance of atmospheric and sedimentary iron sources to Southern Ocean biogeochemistry. GEOPHYSICAL RES. LET. 36, L13601, doi:10.1029/2009GL038914.

Tagliabue, A., O. Aumont, R. DeAth, J. P. Dunne, Stephanie Dutkiewicz, E. Galbraith, K. Misumi, J K. Moore, A. Ridgwell, E. Sherman, C. Stock, M. Vichi, C.Völker, Andrew Yool (2015) How well do global ocean biogeochemistry models simulate dissolved iron distributions? Global Biogeochem. Cycles,30, 149–174,doi:10.1002/2015GB005289.

Uematsu, M., R. A. Duce and J. M. Prospero (1994) Atmosphere beryllium-7 concentrations over the Pacific Ocean. Geophy. Res. Lett. 21, 561-564.

Volk, T. and Hoffert, M.I. (1985) Ocean carbon pumps: Analysis of relative strengths and efficiencies in ocean-driven atmospheric CO2 changes, in: Sundquist, E.T., Broecker, W.S. (Eds.), The Carbon Cycle and Atmospheric CO2: Natural Variations Archean to Present. American Geophysical Union, Washington, D. C., pp. 99-110.

Young, J. A., and W. B. Silker (1980), Aerosol deposition velocities on the Pacific and Atlanic Oceans calculated from 7Be measurements, Earth Planet. Sci. Lett., 50, 92–104, doi:10.1016/ 0012-821X(80)90121-1.

Marine Chemistry

# Sources, Fluxes and Residence Times of Trace Elements measured during the U.S. GEOTRACES East Pacific Zonal Transect.

--Manuscript Draft--

| | |
|---|---|
| **Manuscript Number:** | |
| **Article Type:** | Research Paper |
| **Keywords:** | Trace elements; residence times; East Pacific Ocean; GEOTRACES |
| **Corresponding Author:** | David Kadko<br>Florida International University<br>Miami, FL United States |
| **First Author:** | David Kadko |
| **Order of Authors:** | David Kadko |
| | Ana Aguilar-Islas |
| | Clifton S. Buck |
| | Jessica N. Fitzsimmons |
| | William M. Landing |
| | Alan Shiller |
| | Claire P. Till |
| | Kenneth.W. Bruland |
| | Edward.A. Boyle |
| | Robert F. Anderson |
| **Abstract:** | Trace element (TE) fluxes and their residence times (Fe, Mn, Cu, Pb, Cd, and V) within the surface ocean were determined along the GEOTRACES East Pacific Zonal Transect (GP16/EPZT) and found to reflect the diverse physical and geochemical conditions encountered across the track. The TE flux from atmospheric deposition, vertical mixing, and upwelling into the mixed layer and into the particle production zone (PPZ) along the GEOTRACES EPZT transect were evaluated with 7 Be-based methods developed in earlier works. A horizontal input flux is driven from east to west by the South Equatorial Current (SEC), and estimated advection velocities were applied to horizontal gradients in the distributions of several TEs to approximate this term. There is a minimum in atmospheric deposition in the central gyre, with higher fluxes to the east due to large near-shore aerosol TE loadings, and higher to the west due to greater precipitation-driven deposition velocities (V b ). The 7 Be-derived vertical diffusion (K z ) values range from 2.5 to 39 m 2 /d (0.29 x 10 -4 to 4.5 x 10 -4 m 2 /s) with higher values generally within the nearshore upwelling region and the lowest values within the stratified central gyre. Manganese displayed a well-defined gradient extending from the nearshore stations into the central gyre such that the advective term is a major component of the total input flux, particularly within the central gyre. Relative to other inputs the atmospheric input of soluble Mn is only of minor importance. Unlike Mn, there is no discernable horizontal gradient in the dissolved Fe data and therefore, there is no horizontal component of flux. Nearshore removal processes are more intense for dissolved Fe than for dissolved Mn and as a result, dissolved Mn remains elevated much farther offshore than does dissolved Fe. For the stratified mid-ocean gyre stations, the total input of Fe from all sources is relatively small compared to the inshore stations, and atmospheric deposition becomes the dominant mode of input. Aerosol Fe solubility determined by a 25% acetic acid leach with hydroxylamine hydrochloride was much greater than that derived from a leach using ultra-pure deionized water. This led to significant differences in the residence time of Fe calculated for the mid-ocean gyre using these different solubilities. Generally, each element displays relatively short (days-weeks) residence times within the nearshore region of robust upwelling, reflecting large input terms and rapid removal. Moving offshore, total input fluxes decrease and the residence times of the |

Dr. T.S. Bianchi
Editor in Chief
Marine Chemistry

September 8, 2019

Dear Tom

I am submitting a research paper for consideration in Marine Chemistry: "Sources, Fluxes and Residence Times of Trace Elements measured during the U.S. GEOTRACES East Pacific Zonal Transect". This involves quite a few authors and is a synthesis of many data sets from the expedition.

Suggested Editors: Adina Paytan did a good job on my last submission

Thank you for your consideration.

Sincerely,

David Kadko
Professor and Assoc. Director
Applied Research Center
Florida International University
10555 W Flagler Street, EC 2100
Miami FL, 33174
Phone: (305)348-5016
E-mail: dkadko@fiu.edu
Web: https://arc.fiu.edu/staff/david-c-kadko/

Highlights

- Trace element fluxes to the surface ocean were determined along the GEOTRACES EPZT
- Trace element residence times in the surface ocean were determined along the transect
- Trace element properties reflected diverse physical and geochemical conditions

# Sources, Fluxes and Residence Times of Trace Elements measured during the U.S. GEOTRACES East Pacific Zonal Transect.

David Kadko[a*], Ana Aguilar-Islas[b], Clifton S. Buck[c], Jessica N. Fitzsimmons[d], William M. Landing[e], Alan Shiller[f], Claire P. Till[g], Kenneth.W. Bruland[h], Edward.A. Boyle[i], Robert F. Anderson[j]

[a]Florida International University, Applied Research Center, Miami, FL, USA

[b]College of Fisheries and Ocean Sciences, University of Alaska Fairbanks, Fairbanks, AK, USA

[c]Skidaway Institute of Oceanography, University of Georgia, Savannah, GA, USA

[d]Department of Oceanography, Texas A&M University, College Station, TX, USA

[e]Department of Earth, Ocean and Atmospheric Science, Florida State University, Tallahassee, FL, USA

[f]Department of Marine Science, University of Southern Mississippi, Stennis Space Center, MS, USA

[g]Department of Chemistry, Humbolt State University, Arcata, CA 95521

[h]Ocean Sciences Department, UC Santa Cruz, Santa Cruz CA 95064

[i]Department of Earth, Atmospheric and Planetary Sciences, Massachusetts Institute of Technology, Cambridge, MA 02139.

[j]Lamont-Doherty Earth Observatory, Columbia University, NY, USA

*corresponding author: dkadko@fiu.edu

David Kadko, Florida International University, Applied Research Center, 10555 W. Flagler St., Suite 2100, Miami, FL., 33174, USA

**Keywords:** *Trace elements; residence times; East Pacific Ocean; GEOTRACES*

**ABSTRACT**

Trace element (TE) fluxes and their residence times (Fe, Mn, Cu, Pb, Cd, and V) within the surface ocean were determined along the GEOTRACES East Pacific Zonal Transect (GP16/EPZT) and found to reflect the diverse physical and geochemical conditions encountered across the track. The TE flux from atmospheric deposition, vertical mixing, and upwelling into the mixed layer and into the particle production zone (PPZ) along the GEOTRACES EPZT transect were evaluated with $^{7}$Be-based methods developed in earlier works. A horizontal input flux is driven from east to west by the South Equatorial Current (SEC), and estimated advection velocities were applied to horizontal gradients in the distributions of several TEs to approximate this term. There is a minimum in atmospheric deposition in the central gyre, with higher fluxes to the east due to large near-shore aerosol TE loadings, and higher to the west due to greater precipitation-driven deposition velocities ($V_b$). The $^{7}$Be-derived vertical diffusion ($K_z$) values range from 2.5 to 39 $m^2/d$ (0.29 x $10^{-4}$ to 4.5 x $10^{-4}$ $m^2/s$) with higher values generally within the nearshore upwelling region and the lowest values within the stratified central gyre. Manganese displayed a well-defined gradient extending from the nearshore stations into the central gyre such that the advective term is a major component of the total input flux, particularly within the central gyre. Relative to other inputs the atmospheric input of soluble Mn is only of minor importance. Unlike Mn, there is no discernable horizontal gradient in the dissolved Fe data and therefore, there is no horizontal component of flux. Nearshore removal processes are more intense for dissolved Fe than for dissolved Mn and as a result, dissolved Mn remains elevated much farther offshore than does dissolved Fe. For the stratified mid-ocean gyre stations, the total input of Fe from all sources is relatively small compared to the inshore stations, and atmospheric deposition becomes the dominant mode of input. Aerosol Fe solubility determined by a 25% acetic acid leach with hydroxylamine hydrochloride was much greater than that derived from a leach using ultra-pure deionized water. This led to significant differences in the residence time of Fe calculated for the mid-ocean gyre using these different solubilities. Generally, each element displays relatively short (days-weeks) residence times within the nearshore region of robust upwelling, reflecting large input terms and rapid removal. Moving offshore, total input fluxes decrease and the residence times of the TEs increase markedly until the western edge of the transect. There, relaxation of ocean stratification permits greater upward turbulent flux and greater rainfall leads to greater atmospheric input of TEs.

## 1.0 Introduction

The International GEOTRACES Program was established to identify processes and quantify fluxes that control the distributions of key trace elements (TEs) in the ocean as these chemical species play important roles as nutrients, as tracers of current and past oceanographic processes, and as contaminants derived from human activity (GEOTRACES Planning Group, 2006). Their biogeochemical cycling has relevance to the carbon cycle, climate change, and ocean ecosystems. To accomplish these goals, the

Program established a global series of basin-scale transects to undertake comprehensive TE measurements in the water column and air. One of these was the 2013 U.S. GEOTRACES East Pacific Zonal Transect (EPZT, US GEOTRACES cruise GP16) (Moffett and German, 2018) which originated within the highly productive upwelling region of the Peru Margin and extended westward across the Central South Pacific Ocean to Tahiti, crossing some of the most remote and oligotrophic open-ocean waters on Earth (Figure 1).

The Southeast Pacific Ocean along the EPZT transect (10-18°S) is an especially interesting region to study trace metal fluxes to the surface ocean because low dust input supports only a very low supply of trace metals to the open ocean (Wagener et al. 2008), and it has been suggested that mixing processes might therefore dominate metal fluxes to the surface ocean (Fitzsimmons et al. 2016; Buck et al. 2019). In the upwelling region near South America horizontal mixing and advection are especially important and upwelling drives the ETSP (Eastern Tropical South Pacific) OMZ (Oxygen Minimum Zone) (Karstensen et al. 2008) which results in unique metal signatures (Scholz et al. 2011, 2014) and biological communities (Ohnemus et al. 2017).

Metal fluxes to the surface ocean are critical drivers of primary production, and the EPZT transect is situated on the edge of several biological gradients: 1) the lowest productivity waters in the entire global ocean in the South Pacific subtropical gyre (centered at 25-30°S; Claustre et al. 2008), 2) some of the highest productivity waters in the ocean along the South American continent (e.g. Carr 2001), and 3) the Fe-limited Equatorial Pacific Region (Martin et al. 1994). Sampling across such diverse oceanographic settings would be expected to manifest different sources, sinks, distributions and residence times of trace elements, which must be well constrained to predict or estimate biological responses.

The GEOTRACES program affords the opportunity to extensively sample TEs in the water column and aerosols, including the determination of aerosol solubilities and tracer measurements such as the isotope $^{7}$Be, a cosmi-ray producted isotope (half-life = 53.3. days) that is deposited into the surface ocean and used to study the atmospheric fluxes of TEs and their transport in the upper ocean (e.g. Young and Silker, 1980; Kadko and Olson, 1996; Kadko and Johns; 2011; Haskell et al., 2015; Kadko et al., 2015; Shelley et al., 2016). In this work we utilize the extensive dissolved TE, $^{7}$Be tracer, and aerosol concentration and solubility datasets from EPZT to calculate TE fluxes into the ocean mixed layer and the Particle Production Zone (PPZ; depth where fluorescence reaches 10% of maximum fluorescence) across the transect; from this, we evaluate the residence time of TEs in the upper ocean of this region.

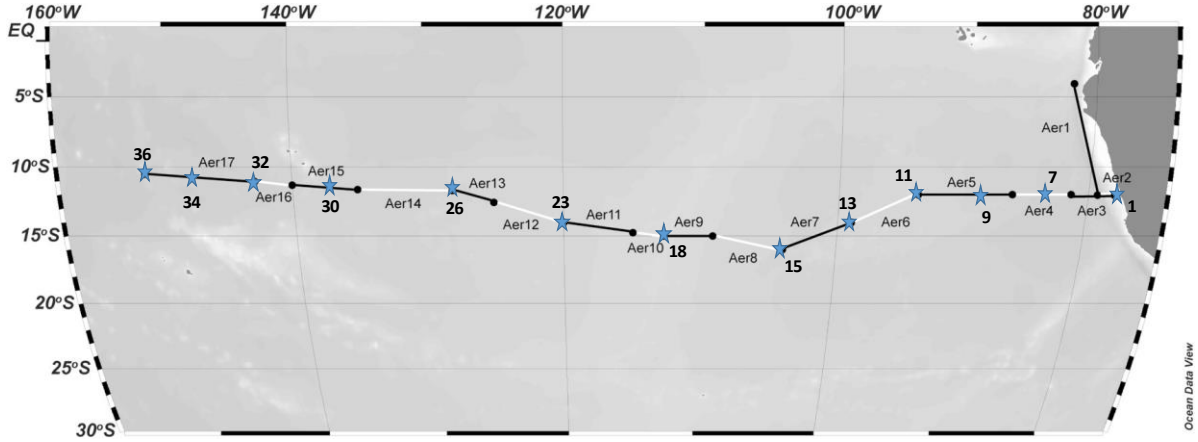


**Figure 1. The 2013 US GEOTRACES EPZT cruise track with aerosol sample deployment locations marked as alternating black and white lines; recovery location of each sample coincides with the deployment location of the next sample (details in Buck at al., 2019). The water sampling stations are indicated by a blue star and the station number; these did not always coincide with aerosol collection deployments.**

## 2.0 Methods

**2.1 Sample Collection**- Seawater and aerosol samples were collected during the U.S. GEOTRACES EPZT (Eastern Pacific Zonal Transect -GEOTRACES cruise GP16) expedition on the R/V Thomas G. Thompson (TGT303, 25 October 2013 - 20 December 2013, Manta, Ecuador - Papeete, Tahiti) along the cruise track shown in Fig. 1.

***2.1.1. Aerosols:*** Details of the aerosol collection methods have been presented in prior work (Buck et al., 2019). Briefly, bulk aerosol samples were collected on 12-replicate acid-washed 47 mm Whatman 41 (W41) ash-less filter discs mounted in Advantec-MFS polypropylene inline filter holders (PP47). When the wind was directed from the bow, air was pumped through the filters using a high-volume aerosol sampler (model 5170V-BL, Tisch Environmental) at approximately 100 L min-1 through each filter. The sampler was mounted on the starboard rail of the 03-deck approximately 16 m above sea level and forward of both the ship's superstructure and exhaust stacks. Each collection period lasted approximately three days.

***2.1.2. Water samples for trace elements***: Seawater was collected following established GEOTRACES sample collection protocols (Cutter and Bruland 2012) using a trace metal-clean CTD mounted on an epoxy-coated aluminum rosette housing 24 GO-Flo bottles (12 L each) on a Vectran conducting cable. Seawater was filtered in a clean sampling van under ~0.5 atm of filtered air through 0.2 µm Acropak-200 polyethersulfone capsule filters (Pall) into pre-cleaned bottles following three 10% volume rinses. Samples were acidified to pH 2 with ultrapure hydrochloric acid (Optima grade, Fisher Scientific) or pH ~1.7 with quartz-distilled hydrochloric acid (Bruland lab) and stored at least 3 months prior to analysis.

***2.1.3. Water column $^{7}$Be***: Details of sample collection for this expedition have been presented in Kadko, (2017). Briefly, samples were collected at selected depths by pumping 400–700 L of seawater via a ~4cm hose into large plastic barrels on deck. From these barrels, the seawater was then pumped through iron impregnated acrylic fibers at ~10 L/min (Lal et al., 1988; Krishnaswami et al., 1972; Lee et al., 1991) to extract the $^{7}$Be from seawater.

## 2.2 Analytical methods

***2.2.1. Aerosol samples:*** Total trace metal concentrations in the samples were determined at the University of Alaska Fairbanks by inductively couple plasma mass spectrometry (ICPMS) using a Thermo Element-2 ICP mass spectrometer following digestion with concentrated nitric and hydrofluoric acids. Method fitness was tested by digesting three reference materials and quantifying elemental recoveries. Details can be found in Buck et al. (2019). For $^{7}$Be, the Whatman-41 aerosol filters were stacked three-high in a plastic Petri dish and counted by gamma spectroscopy. This configuration was calibrated with a commercially prepared mixed solution of known gamma activities.

Soluble TE concentrations were measured in both ultrapure deionized water (DI water; 18.2 MΩ·cm) after Buck et al. (2006), and in ammonium acetate solution with a reducing agent after modifications to one of the methods ("$HAc_{T*+R,}$") as described in Berger et al. (2008). Three filters from each deployment were extracted by each treatment producing triplicate DI water soluble aerosol samples and triplicate acetic acid soluble aerosol samples which will be called "HAc" samples from this point forward.

Then DI water method produces a lower-limit of elemental solubility and the HAc method an upper limit such that a "solubility window" for each element is provided (Shelley et al., 2018). The HAc leach treatment is designed to extract TEIs associated with biogenic material, carbonates, most forms of Fe and Mn (oxyhydr)oxides and those adsorbed to clay minerals. The reducing conditions may simulate the conditions particles experience during passage through a zooplankton gut or inside a fecal pellet or organic aggregate while the low pH (2.1) serves to prevent any reprecipitation or adsorption artifacts.

All sample handling was performed under Class-100 laminar flow conditions and all filters were stored frozen prior to processing. Extractions with DI water took place while at sea, while extractions with HAc took place at the University of Alaska Fairbanks. The W41 filter discs were extracted with 100 mL of ultrapure DI water (>18 MΩ cm) under a vacuum. The extract flowed through a Teflon-PFA filter holder (Savillex) loaded with an acid-washed 0.4 µm Nuclepore backing filter and directly into an acid-washed 100 mL 100% LDPE receiving bottle. Samples were immediately acidified with Teflon-distilled 6M hydrochloric acid to a final concentration was 0.024M HCl. DI water soluble aerosol TE concentrations were determined by inductively coupled plasma mass spectrometry (Perkin Elemer Nexion 300D) at the Skidaway Institute of Oceanography. This quadrupole ICP-MS utilizes $NH_3$ as a reaction gas to eliminate polyatomic interferences. Additionally, the analytes were concentrated on an in-line chelating

resin (Nobias PA-1) prior to introduction to the plasma (ESI seaFAST S3 system). Instrument detection limits were determined by measuring the reagent blank of the system multiple times during each run and calculating three times the standard deviation of those analyses. Deployment filter blank extracts were prepared at sea with W41 discs that had been deployed in the aerosol samplers for 1 h while not in operation. Three replicate blanks were extracted each time a group of samples were extracted thereby accounting for any variability in the quality of the ship-provided DI water.

For the determination of HAc soluble aerosol trace element loadings, the thawed W41 filter discs were folded twice into a wedge and transferred to acid cleaned centrifuge tubes. Extractions were carried out following the "$HAc_{T*+R}$," procedure described in Berger et al., 2008, which includes a reducing agent and a heating step. We modified the method by adding a centrifugation step to prevent transfer of unextracted particulate trace elements. Briefly, 1mL of 25% acetic acid with 0.02M hydroxlamine hydrocholoride was added to the folded filters, which were immediately placed in a 90 $^{o}$C hot water bath for 10 minutes, then left to cool for 2 hours. Samples were centrifuged, and the solution was carefully transferred into Teflon beakers. Filters were then rinsed 3 times with 500µl of ultra-pure DI water, with a centrifugation step after each rinse and careful transfer into the corresponding Teflon beaker. The solutions on the beakers were set to dry on a hot plate down to a pearl. The residue was then reconstituted with 1mL of Optima grade concentrated nitric acid and decanted into an acid-washed, wide-mouth, 30 ml polyethylene bottle (Nalgene). Each beaker was rinsed 3 times with 5ml of 0.1 % v/v Optima grade nitric acid, with rinses decanted into the corresponding 30 ml bottle. All sample handling was performed under Class 100 laminar flow conditions. Deployment blanks were processed in the same manner as samples. HAc soluble aerosol trace metal concentrations were determined by inductively coupled plasma mass spectrometry (Thermo Element 2) using external standard curves. Indium was added to standards and samples to track instrument fluctuations. Prior to direct injection, sample solutions were diluted as needed by a factor of 2 to 20 with 1 M Optima grade nitric acid, and deployment blank solution were diluted by a factor of 2. Analysis took place at the University of Alaska Fairbanks.

#### *2.2.2. Dissolved trace metals*

The dissolved metal data used in this paper have been culled from the GEOTRACES Intermediate Data Product (IDP) 2017 (Schlitzer et al. 2018) and from several published papers (Resing et al. 2015 for Mn; Fitzsimmons et al. 2017 and John et al. 2018 for Fe; Roshan and Wu 2018 for Cu; Ho et al., 2019 for V); the details of these methods can be found in these publications. Dissolved Fe, Mn, Cu, Pb, and Cd were also measured using established methods (Biller and Bruland 2012; Parker et al. 2016) after UV irradiation and preconcentration onto Nobias PA1 chelating resin, followed by ICP-MS analysis and comparison to matrix-matched standard curves. Dissolved Pb was also analyzed across the transect using isotope dilution ICP-MS with $^{206}$Pb on a quadrupole ICP-MS (Fisons PQ+; Lee et al. 2011). These

datasets were all rigorously intercalibrated by the originating labs, and the intercalibration procedures were reviewed and approved by the GEOTRACES Standards & Intercalibration Committee before being published in the GEOTRACES IDP 2017.

***2.2.3. Water column $^{7}$Be*** – Details of the $^{7}$Be analysis for this expedition are presented in Kadko (2017). On land, the fibers were dried and then ashed. The ash was subsequently pressed into a pellet (5.8 cm diameter) and placed on a low background germanium gamma detector. The isotope $^{7}$Be has a readily identifiable gamma peak at 478 keV. The detector was calibrated for the pellet geometry by adding a commercially prepared mixed solution of known gamma activities to an ashed fiber, pressing the ash into a pellet, and counting the activities to derive a calibration curve. The uncertainty of the extraction efficiency (4%) and the detector efficiency (2%) was in all cases smaller than the statistical counting error and the uncertainty in the blank.

2.3 Flux calculations.

The flux of TEs into the mixed layer and the PPZ along the GEOTRACES EPZT transect are composed of four components: i) atmospheric deposition ii) vertical mixing from below, iii) upwelling if present, and iv) horizontal advection from east to west driven by the South Equatorial Current (SEC) if horizontal gradients in the TE distribution exist. In the Northern Equatorial Pacific, Landing and Bruland (1987) reported rapid off- shore advective transport from the eastern boundary by the North Pacific Equatorial Current, indicating the importance of this transport term in any TE mass budget calculation.

i) *Atmospheric deposition*. The bulk atmospheric flux for aerosol trace elements ($F_{atm}$) is estimated from the concentration of trace elements in the aerosols ($C_{TE}$) and the bulk deposition velocity ($V_b$) which includes dry + wet deposition, such that

$$F_{atm} = C_{TE} \times V_b \qquad \text{Eqn 1}$$

It has been shown that $V_b$ can be derived from the upper ocean inventory of $^{7}$Be and the aerosol $^{7}$Be activity (Young and Silker, 1980):

$$V_b = (Inventory^{7}Be \times \lambda)/\left(\,^{7}Be\right)_{aerosol} \qquad \text{Eqn 2}$$

where λ is the $^{7}$Be decay constant (0.013 $d^{-1}$).

This method has been used to derive the TE atmospheric flux for sites in the Atlantic (Kadko et al., 2015; Anderson et al., 2016; Shelley et al., 2017), the Pacific (Buck et al., 2019), and the Arctic (Kadko et al., 2016; 2019; Marsay et al., 2018) oceans.

The most biogeochemically relevant fraction of atmospheric flux is that which is operationally

defined as soluble. We adjust Eq. (1) to account for the elemental aerosol fractional solubility, β such that the atmospheric flux of soluble TE equals the product of the bulk atmospheric flux and the measured fractional solubility determined for each element:

$$F_{atm} = C_{TE} \times V_b \times \beta \qquad \text{Eqn. 3}$$

In this paper we will consider the atmospheric flux of soluble TEs based on the solubilities determined by both the DI and HAc leach approaches.

ii) *Vertical diffusion*. Diffusive transport below the mixed layer is described by $F_D = K_z\, dC/dz$, where $K_z$ is the turbulent diffusion coefficient and dC/dZ is the vertical gradient in TE concentration. The shape of the $^7$Be profile below the ocean mixed layer can be used to derive vertical diffusion rates (Kadko and Olsen, 1996; Kadko and Johns, 2011; Haskell et al., 2015; Kadko, 2017):

$$C(z) = C_0\, e^{\alpha(z-H)} \qquad \text{Eqn 4a}$$

where C(z) is the $^7$Be activity at depth z and H is the depth of the mixed layer and

$$\alpha = \frac{w}{2K_z} + \frac{1}{2}\left\{\left(\frac{w}{K_z}\right)^2 + \frac{4\lambda}{K_z}\right\}^{\frac{1}{2}} \qquad \text{Eqn 4b}$$

where $w$ is the upwelling rate (m/d). In the absence of upwelling ($w$=0),

$$C(z) = \exp[-(\lambda/K_z)^{1/2} \cdot Z] \qquad \text{Eqn 5}$$

where Z is the depth below the mixed layer H.

iii). *Upwelling*. Within regions of upwelling the dilution of the water column $^7$Be inventory by deep, $^7$Be-free upwelled water provides a means to infer upwelling rates quantitatively (Kadko and Johns, 2011; Haskell et al., 2015; Kadko 2017). The upwelling flux is calculated using Eqn. 6, where $w$ is the upwelling rate either at the base of the mixed layer or the base of the PPZ, and C is the trace element concentration at that horizon:

$$\text{Upwelling flux } F_U = w\,[C] \qquad \text{Eqn 6.}$$

The results and discussion for the upwelling stations of the EPZT transect (stations 1-15) have been presented elsewhere (Kadko, 2017).

iv). Horizontal advection. Near-surface east-to-west currents, calculated from satellite-tracked drogued drifter velocities, are in the range 0.1-0.5m/s for the EPZT region (Lumpkin and Johnson, 2013). The timescale of transport from nearshore to the central gyre (~5000 km) would then be in the range 580 – 116 days respectively, with the upper end of this range more likely as the velocity for the entire mixed layer would be lower than that determined for the near-surface. Surface $^{228}$Ra data (Sanial et al., 2018)

provide additional insight into the rate of offshore transport from the continental margin. The continental shelf is a source of $^{228}$Ra which subsequently decays with a 5.75 y radioactive half-life upon transport offshore. The open water activities of the central gyre are ~ half the near-shore values. Based on radioactive decay, the transport timescale would be ~ 2000 days, equivalent to a horizontal velocity of 0.03 m/s. This is not consistent with the Lumpkin and Johnson (2013) observations and likely is an underestimate, as $^{228}$Ra dilution and loss due to surface uptake and particle settling were ignored in this simple calculation. In the discussions that follow, the effect of horizontal transport upon the TE distributions will be considered in detail, using a range of velocities (sections 3.1 and 3.2).

The net horizontal flux into the mixed layer is given by:

$$F_{HZ} = H \cdot u \cdot \frac{dC}{dX} \qquad \text{Eqn 7}$$

Where $H$ is the height of the mixed layer, $u$ is the horizontal velocity and $dC/dX$ is the horizontal concentration gradient between profiles. Meridional transport is assumed to be small compared to the zonal transport in this section. For water below the mixed layer and within the PPZ, an estimate of 0.05m/s, based on a high-resolution ocean general circulation model, was used (Masumoto et al., 2004). Including the mixed layer as part of the PPZ, the net horizontal flux into the PPZ is:

$$F_{PPZ} = F_{PPZ} = H \cdot u \cdot \frac{dC}{dX} + (H_{PPZ} - H)u' \cdot \frac{dC}{dX} \qquad \text{Eqn 8}$$

Where $H_{ppz}$ is the base of the PPZ and $u'$ is the is the horizontal velocity between the mixed layer and base of the PPZ.

These calculations will depend on the depths of the MLD and the PPZ, and these parameters may naturally vary in ways that cannot always be predicted or observed. However, as shown below this does not have a great effect on the calculated residence times.

## 2.4 Residence time calculations

Residence time is a useful concept that informs us of several aspects of trace element biogeochemical behavior in the upper ocean, including dissolution and scavenging processes, biological utilization, and the seasonal relationship of surface concentrations to atmospheric input (e.g. Jickells, 1999; Croot et al., 2004; Hayes et al., 2015; Bridgestock et al., 2016; Kadko et al., 2019). For the mixed layer it is defined by the dissolved TE inventory divided by the sum of the input fluxes.

$$\tau_{ML} = [\text{mixed layer TE inventory}]/[F_{atm} + F_D + F_U + F_{HZ}] \qquad \text{Eqn 9}$$

The residence time can also be calculated using the sum of the export fluxes (e.g. Black et al, 2019), since at steady state, the sum of the input fluxes should equal the sum of the output fluxes.

While the effect of variable mixed layer depth (MLD) would affect the horizontal flux term ($F_{HZ}$),

the effect on the residence time calculation is mitigated because the mixed layer TE inventory changes in the opposite sense of the flux term. For example, an increase in MLD might produce a higher mixed layer TE inventory (in the numerator) but also a higher $F_{HZ}$ (eqn. 7) in the denominator. In this way, the effects of variable MLD on residence times tends to cancel out.

While residence times are often reported for the mixed layer, it is also useful to consider the geochemical behavior of TEs within the slightly deeper particle production zone (PPZ), defined from the surface to its base level where the fluorescence signal approaches 10% of the fluorescence maximum. This has recently been adopted as defining the euphotic zone (Owens et al, 2015; Ohnemus et al. 2016; Kadko, 2017). Then

$$\tau_{PPZ} = [\text{PPZ TE inventory}]/[F_{atm} + F_D + F_U + F_{PPZ}] \qquad \text{Eqn. 10}$$

Both calculations will be considered here.

## 3.0 Results and Discussion

**TABLE 1. Average Aerosol Trace Element Concentrations**

| Sta no. | Aerosol no. | $^7$Be (dpm/m$^3$) | V (pmol/m$^3$) | Fe (nmol/m$^3$) | Mn (nmol/m$^3$) | Cu (nmol/m$^3$) | Cd (pmol/m$^3$) | Pb (pmol/m$^3$) | Al (nmol/m$^3$) | Ti (nmol/m$^3$) |
|---|---|---|---|---|---|---|---|---|---|---|
| 1-15 | 1-7 | 0.211 ±0.092 | 6.780 ±7.734 | 0.684 ±0.824 | 0.0136 ±0.0161 | 0.0096 ±0.0113 | 0.372 ±0.448 | 1.392 ±1.667 | 2.140 ±2.695 | 0.071 ±0.081 |
| 18-36 | 8-17 | 0.133± 0.039 | 0.288 ±0.139 | 0.058 ±0.026 | 0.0008 ±0.0004 | 0.00118 ±0.0004 | 0.028 ±0.024 | 0.377 ±0.160 | 0.147 ±0.040 | 0.015 ±0.005 |

### 3.1. Flux calculations

i) *Atmospheric flux*. The GEOTRACES transect crossed a significant gradient in atmospheric deposition driven by dust input into the eastern transect near the continental shelf (stations 1-15), coincident with the area of upwelling (Table 1, Buck et al., 2019). Moving westward over the open ocean (stations 18-36), the aerosol and TE concentrations were substantially lower, although this is not as apparent for $^7$Be. Here the region is characterized by the strong stratification and oligotrophic conditions of the subtropical gyre (Fig 2a).

Continuing west of 140$^o$W, the rainfall is considerably higher than over the mid-gyre stations which is manifested by decreasing surface salinity and increasing $^7$Be inventories (Fig 2b); it has been observed that $^7$Be deposition rates correlate with the rate of precipitation (e.g. Young and Silker, 1980; Olsen et al., 1985; Uematsu et al., 1994; Kim et al., 1999; Kadko and Prospero, 2011; Peng et al., 2019). Accordingly, the higher $^7$Be inventories result in higher deposition velocities towards the western stations compared to stations to the east (Eqn. 2). This results in a minimum in atmospheric TE deposition in the central gyre, with higher fluxes to the east due to higher aerosol TE loads (Figure 2a), and higher to the

west due to higher $V_b$ values resulting from increased precipitation (Figure 2b, Table 2). Our bulk atmospheric flux estimates of Mn (based on the $^7$Be method) across the transect range between 1 and 16.5 nmol/m$^2$/d which is comparable to the range (0.1-16 nmol/m$^2$/d) of atmospheric particulate flux presented in Black et al (2019) who used dust-model estimates combined with upper crust ratios for each element. Buck et al. (2019) estimated bulk aerosol Mn deposition to range between 0.45 – 68 nmol/m$^2$/d by assuming a constant deposition velocity of 1500 m/d applied to observed aerosol TE concentrations but those estimates are susceptible to the short-term variability of aerosol concentrations and the episodic nature of dust transport.

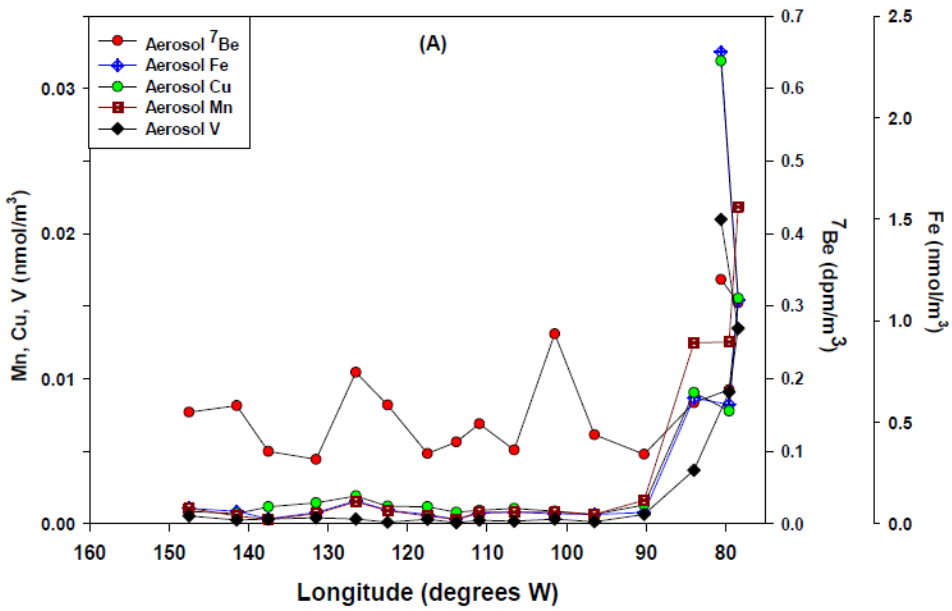


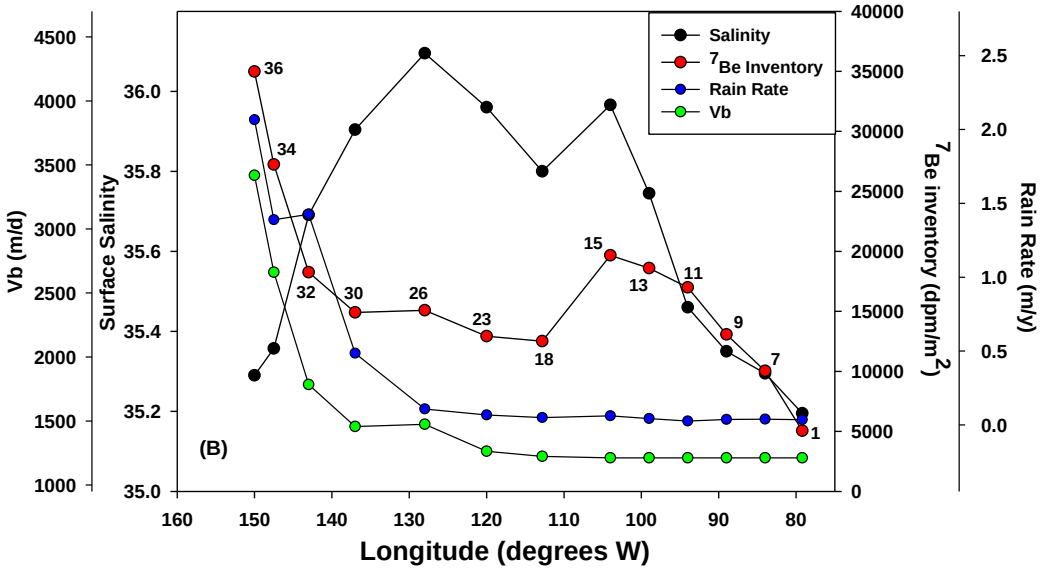

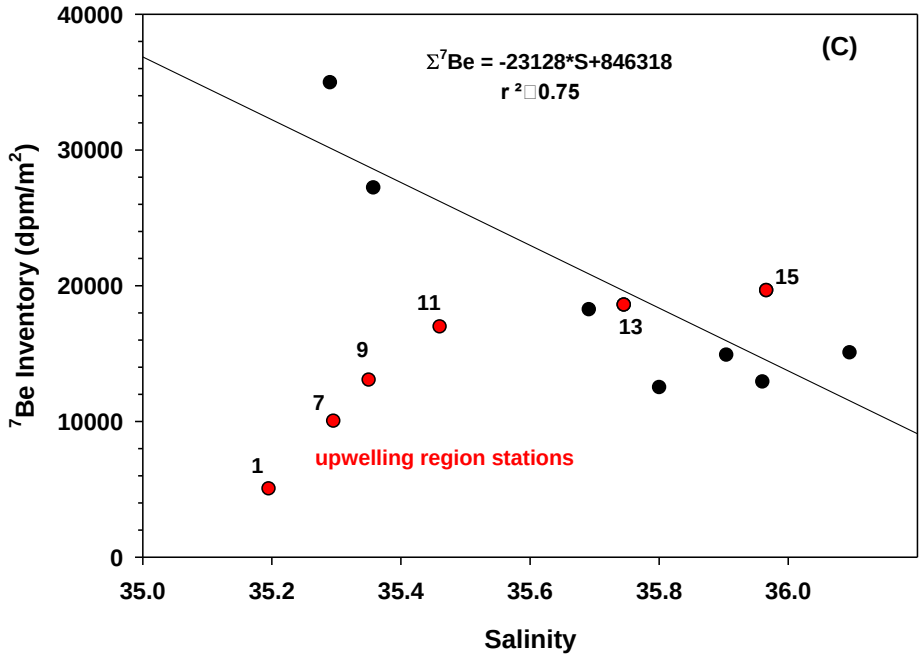


**Figure 2. A) Aerosol TE and $^{7}$Be concentrations along the EPZT transect. Note the high TE concentrations towards the eastern portion of the transect. This is not as apparent for $^{7}$Be. B) Rainfall (from Global Precipitation Climatology Project, GPCP) for the cruise period across the transect. Note the coincident increase in precipitation, decrease in salinity and increases in $^{7}$Be inventory and bulk deposition velocity ($V_b$) at the westernmost portion of the transect. C) $^{7}$Be inventory plotted against salinity. Stations within the upwelling region are plotted separately in red. The linear regression applies to non-upwelling region stations (black). Despite low rainfall, salinity is low at the eastern portion of the transect because of upwelling of low salinity water. Note that the $^{7}$Be inventory is also lower because of upwelled low-$^{7}$Be water (Kadko, 2017).**

Note that the low salinity in the eastern stations (Fig 2a) is not the result of high precipitation but of upwelling of low salinity water (Fig 2c). Because of upwelling, Eqn. 2 does not hold for the easternmost stations 1-13, as the observed $^{7}$Be inventory does not reflect atmospheric input, but rather upwelling of deep, $^{7}$Be deficient water. For this reason, the inventories of these stations (for use in eqn. 2) are assigned that of station 15, the nearest station not affected by the upwelling process (Kadko, 2017; Buck et al., 2019). Thus, the nearshore stations display a constant deposition velocity and flux (Fig 2b, Table 2).

The fractional solubility for several TEs, determined by the DI and HAc leaches, are presented in Tables 3a and 3b. These were then applied to Eqn. 3 to derive the atmospheric fluxes of soluble (aerosol dissolvable) TEs.

TABLE 2. Bulk Atmospheric TE flux[a,b]

| Sta | $^{7}$Be inventory (dpm/m$^2$) | $^{7}$Be Flux | Vb (m/d) | Fe Flux (nmol/m$^2$/d) | Mn Flux (nmol/m$^2$/d) | Cu Flux (nmol/m$^2$/d) | Cd Flux pmol/m2/d | Pb Flux pmol/m2/d | Al Flux (nmol/m$^2$/d) | V Flux (nmol/m$^2$/d) |
|---|---|---|---|---|---|---|---|---|---|---|
| 1 | 19666 | 256 | 1212 | 828.8 | 16.48 | 11.63 | 450.7 | 1687 | 2593 | 8.2 |
| 7 | 19666 | 256 | 1212 | 828.8 | 16.48 | 11.63 | 450.7 | 1687 | 2593 | 8.2 |
| 9 | 19666 | 256 | 1212 | 828.8 | 16.48 | 11.63 | 450.7 | 1687 | 2593 | 8.2 |
| 11 | 19666 | 256 | 1212 | 828.8 | 16.48 | 11.63 | 450.7 | 1687 | 2593 | 8.2 |
| 13 | 19666 | 256 | 1212 | 828.8 | 16.48 | 11.63 | 450.7 | 1687 | 2593 | 8.2 |
| 15 | 19666 | 256 | 1212 | 828.8 | 16.48 | 11.63 | 450.7 | 1687 | 2593 | 8.2 |
| 18 | 12516 | 163 | 1223 | 71.0 | 0.98 | 1.35 | 34.25 | 461.2 | 179.8 | 0.35 |
| 23 | 12930 | 168 | 1264 | 73.3 | 1.01 | 1.39 | 35.39 | 476.5 | 185.8 | 0.36 |
| 26 | 15085 | 196 | 1474 | 85.5 | 1.18 | 1.62 | 41.29 | 555.9 | 216.2 | 0.42 |
| 30 | 14906 | 194 | 1457 | 84.5 | 1.17 | 1.60 | 40.80 | 549.3 | 214.18 | 0.42 |
| 32 | 18258 | 237 | 1785 | 103.5 | 1.43 | 1.96 | 49.97 | 672.8 | 262.3 | 0.51 |
| 34 | 27230 | 354 | 2662 | 154.4 | 2.13 | 2.93 | 74.52 | 1003 | 391.25 | 0.77 |
| 36 | 34981 | 455 | 3419 | 198.3 | 2.74 | 3.76 | 95.74 | 1289 | 502.6 | 0.98 |

a. Fluxes calculated using average aerosol concentrations reported in Table 1.
b. Soluble atmospheric flux= bulk atmospheric flux x solubility (see table 3).

Table 3a. TE aerosol solubilities in dionized water

| Deployment | Start Date | Start Latitude | Start Longitude | Fe% | % Error | Mn% | % Error | Cu% | % Error |
|---|---|---|---|---|---|---|---|---|---|
| | | °S | °W | | | | | | |
| Aer1 | 26-Oct | 4.07 | 81.99 | 2.42 | 0.12 | 43.7 | 2.2 | 42.8 | 4.0 |
| Aer2 | 29-Oct | 12.01 | 79.20 | 1.99 | 0.59 | 37.0 | 2.2 | 37.7 | 2.0 |
| Aer3 | 1-Nov | 12.05 | 77.66 | 1.27 | 0.54 | 32.1 | 2.0 | 38.2 | 2.6 |
| Aer4 | 4-Nov | 12.00 | 81.50 | 1.94 | 0.50 | 34.2 | 2.7 | 36.6 | 3.9 |
| Aer5 | 7-Nov | 12.00 | 86.50 | 4.75 | 0.50 | 61.7 | 32.4 | 46.0 | 20.8 |
| Aer6 | 10-Nov | 12.00 | 94.00 | 1.55 | 0.61 | 44.4 | 14.2 | 29.9 | 4.1 |
| Aer7 | 13-Nov | 14.00 | 99.00 | 0.94 | 0.52 | 35.5 | 4.4 | 24.7 | 6.4 |
| Aer8 | 16-Nov | 16.00 | 104.00 | 0.69 | 0.13 | 25.1 | 4.7 | 18.8 | 8.5 |
| Aer9 | 19-Nov | 15.00 | 109.19 | 0.56 | 0.11 | 26.0 | 8.6 | 10.3 | 4.1 |
| Aer10 | 22-Nov | 14.99 | 112.75 | 1.47 | 0.13 | 48.8 | 8.4 | 17.8 | 7.3 |
| Aer11 | 25-Nov | 14.77 | 115.00 | 0.83 | 0.15 | 30.2 | 4.6 | 12.8 | 5.7 |
| Aer12 | 28-Nov | 14.00 | 120.00 | 0.49 | 0.21 | 20.5 | 5.5 | 56.8 | 13.8 |
| Aer13 | 1-Dec | 12.54 | 125.00 | 0.35 | 0.27 | 18.2 | 7.5 | 15.7 | 6.2 |
| Aer14 | 4-Dec | 11.67 | 128.00 | 1.27 | 0.32 | 26.5 | 8.1 | 16.9 | 3.3 |
| Aer15 | 7-Dec | 11.60 | 135.00 | 1.23 | 0.25 | 51.8 | 18.0 | 17.3 | 1.7 |
| Aer16 | 10-Dec | 11.31 | 140.00 | 1.68 | 0.84 | NA | NA | 24.9 | 10.8 |
| Aer17 | 13-Dec | 11.03 | 142.95 | 0.69 | 0.34 | 38.8 | 3.5 | 24.7 | 5.4 |
| | | | average | 1.42 ± 1.04 | | 35.9 ± 11.9 | | 27.7 ± 13.2 | |

Table 3b. TE aerosol solubilities by HAc method

| Deployment | Start Date | Start Latitude | Start Longitude | Fe% | % Error | Mn% | % Error | Cu% | % Error |
|---|---|---|---|---|---|---|---|---|---|
| | | °S | °W | | | | | | |
| Aer1 | 26-Oct | 4.07 | 81.99 | 12.52 | 0.88 | 46.59 | 2.22 | 55.35 | 4.06 |
| Aer2 | 29-Oct | 12.01 | 79.20 | 8.45 | 0.48 | 40.25 | 2.05 | 53.44 | 2.33 |
| Aer3 | 1-Nov | 12.05 | 77.66 | 8.32 | 0.85 | 43.42 | 5.18 | 56.95 | 6.63 |
| Aer4 | 4-Nov | 12.00 | 81.50 | 10.45 | 2.40 | 39.27 | 6.01 | 65.57 | 4.82 |
| Aer5 | 7-Nov | 12.00 | 86.50 | 31.63 | 2.63 | 93.65 | 2.17 | 85.71 | 8.16 |
| Aer6 | 10-Nov | 12.00 | 94.00 | 16.54 | 3.14 | 52.78 | 19.16 | 60.98 | 6.43 |
| Aer7 | 13-Nov | 14.00 | 99.00 | 22.86 | 2.90 | 37.78 | 4.75 | 87.50 | 23.63 |
| Aer8 | 16-Nov | 16.00 | 104.00 | 6.88 | 0.97 | 12.89 | 2.55 | 22.06 | 8.93 |
| Aer9 | 19-Nov | 15.00 | 109.19 | 19.45 | 0.00 | 31.11 | 0.00 | 45.21 | 0.00 |
| Aer10 | 22-Nov | 14.99 | 112.75 | 60.66 | 12.92 | 55.56 | 10.80 | 72.55 | 36.92 |
| Aer11 | 25-Nov | 14.77 | 115.00 | 26.72 | 6.62 | 53.33 | 9.75 | 68.00 | 25.25 |
| Aer12 | 28-Nov | 14.00 | 120.00 | 13.03 | 5.41 | 28.00 | 9.01 | 65.38 | 14.37 |
| Aer13 | 1-Dec | 12.54 | 125.00 | 22.96 | 3.96 | 33.33 | 14.92 | 80.00 | 25.62 |
| Aer14 | 4-Dec | 11.67 | 128.00 | 16.08 | 2.29 | 24.19 | 18.95 | 36.96 | 6.80 |
| Aer15 | 7-Dec | 11.60 | 135.00 | - | - | - | - | - | - |
| Aer16 | 10-Dec | 11.31 | 140.00 | 68.21 | 33.06 | 123.91 | 57.45 | 126.67 | 53.00 |
| Aer17 | 13-Dec | 11.03 | 142.95 | 12.88 | 3.83 | 42.37 | 7.67 | 69.09 | 18.58 |
| | | | average | 22.35 ± 17.89 | | 47.40 ± 27.01 | | 65.71 ± 23.62 | |

Table 4. Vertical transport parameters

| Station | upwelling rate | | Diffusion |
|---|---|---|---|
| | W (ML)[a] | W (PPZ)[b] | Kz[c] |
| | (m/d) | (m/d) | ($m^2$/d) |
| 1 | 4.4 | 3.3 | 38 |
| 7 | 1.3 | 0.75 | 39 |
| 9 | 1.5 | 0.68 | 30.65 |
| 11 | 0.04 | 0.005 | 14.7 |
| 13 | -0.12 | -0.007 | 24.1 |
| 15 | 0.15 | 0.01 | 26 |
| 18 | 0 | 0 | 28 |
| 23 | 0 | 0 | 24 |
| 26 | 0 | 0 | 6 |
| 30 | 0 | 0 | 2.5 |
| 32 | 0 | 0 | 2.5 |
| 34 | 0 | 0 | 20 |
| 36 | 0 | 0 | 7 |

a. Upwelling at the base of the mixed layer (Kadko, 2017)
b. Upwelling at the base of the PPZ (Kadko, 2017)
c. Turbulent diffusion coefficient. Values for stations 1-15 from Kadko, (2017); values for stations 18-36 from this work.

ii) *Vertical diffusion.* The turbulent diffusion coefficients for the upwelling stations of the EPZT transect (stations 1-15) based on $^7$Be profiles have been derived previously (Kadko, 2017) and are summarized in Table 4. The $^7$Be profiles for stations 18-36 are shown in supplemental figure S1, and the derived diffusion coefficients presented in Table 4. The $^7$Be-derived $K_z$ values range from 2.5 to 39 $m^2$/d (0.29 x $10^{-4}$ to 4.5 x $10^{-4}$ $m^2$/s) with higher values generally within the nearshore upwelling region and the lowest values within the central gyre. This pattern is consistent with the greater surface ocean stratification of the gyre which is reflected in a plot of $K_z$ vs. Brunt- Väisälä frequency (N) derived for the water column between the base of the mixed layer and the depth of the PPZ (Figure 3A). In addition, the $^7$Be-derived $K_z$ generally decreases as the mixed layer depth increases (Figure 3B) suggesting that the deeper mixed layers here penetrate into more stratified water. In these figures the stations with the most robust upwelling (stations 1, 7, and 9) manifest $K_z$ values greater than the trend for the other stations, which is consistent with the energetic environment of the upwelling regime.

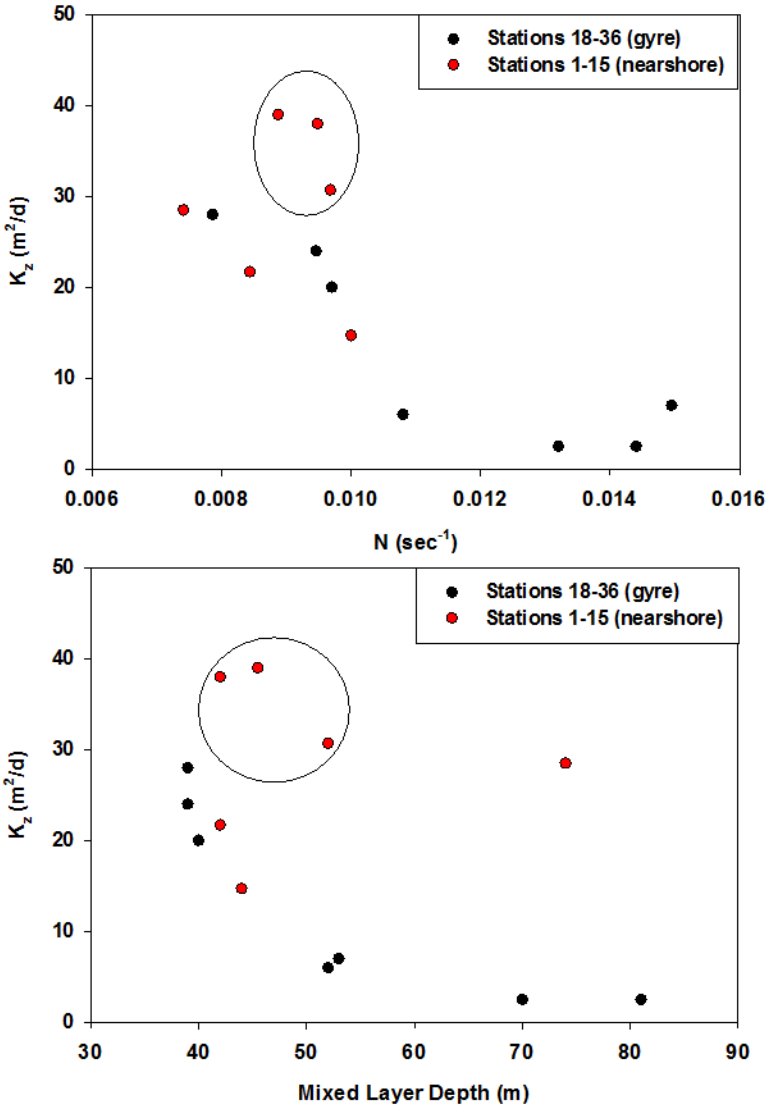


**Figure 3. A). The $^7$Be-derived $K_z$ plotted against Brunt- Väisälä frequency. B). The $^7$Be-derived $K_z$ plotted against mixed layer depth. Nearshore stations 1-15 (red) and offshore stations 18-36 (black) are indicated separately. Nearshore stations 1,7, and 9 with the greatest rates of upwelling are circled and fall off the trend set by the rest of the stations.**

iii) *Upwelling flux*. The upwelling rates for the eastern stations of the EPZT transect (stations 1-15) have been derived elsewhere (Kadko, 2017) and are summarized in Table 4. The upwelling rate is modeled to linearly decrease from the base of the mixed layer to zero at 100 m below the mixed layer. The upwelling TE fluxes are significant for these stations and in some cases are the dominant source of a TE into the mixed layer and the PPZ. A summary of all the input fluxes for the mixed layer and the PPZ are shown in Table 5.

iv). *Horizontal advection*. Horizontal velocities discussed above were combined with horizontal gradients along the EPZT transect to derive horizontal fluxes according to eqns. 7 and 8. These are summarized in Table 5.

*Manganese*- In both the mixed layer and at the depth of the PPZ, Mn shows a clear east-to-west gradient (Figure 4). For this calculation, we choose a current speed of 0.1m/s which is at the lower end of the range of Lumpkin and Johnson (2013) and consistent with the $^{228}$Ra data of Sanial et al. (2018). The data in Table 5 indicate that despite a large atmospheric dust input to the near shore stations, the greatest flux of Mn is upwelled, suggesting a shelf-sediment porewater origin (e.g. Sanial et al., 2018). A similar observation was made off NW Africa, where high Mn occurs in a region associated with both upwelling and dust input, but the dominant source was upwelling (Shiller, 1997). We also note that some dissolved Mn at the easternmost stations is derived from upwelling of waters where *in situ* reduction of particulate Mn(IV) to dissolved Mn(II) is favored due to the oxygen deficient conditions (Cutter et al. 2018; Lee et al. 2018), but this is likely less than the porewater-diffused Mn flux.

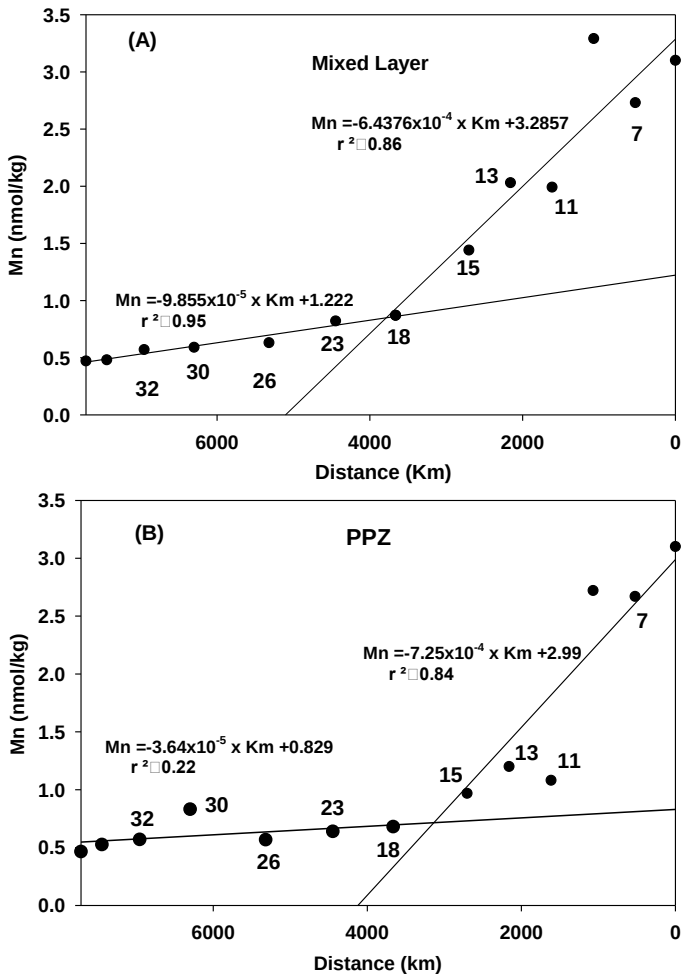


Figure 4.

A) Dissolved Mn plotted against distance from station 1 for the mixed layer across the EPZT.

B) Dissolved Mn plotted against distance from station 1 for the PPZ across the EPZT.

For the offshore gyre stations, horizontal transport is the dominant flux term. Dissolved Mn profiles of most stations display a maximum below the mixed layer suggestive of this advective input (supplemental Figure S2). The horizontal Mn concentration gradient between stations is steepest for the near-shore stations, indicating removal as the Mn, diffused from sediments, is transported offshore and begins to be oxidized (Figure 4). Towards the open ocean (west of station 15 at 104ºW) the gradient is diminished suggesting a slower removal rate. This will be apparent in the residence time calculations discussed below. Sanial et al. (2018) found a similar discontinuity in the upper 200m $^{228}$Ra distribution across the transect but noted that even in the gyre stations $^{228}$Ra was still above the detection limit which suggested these surface waters had recently (years) been in contact with the continental margin. They suggested that the correlation between dissolved Mn and $^{228}$Ra over the transect indicates that Mn was transported over considerable length scales into the open ocean. They also used $^{228}$Ra as a "flux gauge" to derive a Mn flux from the shelf into the open water of 9000 nmol/m$^2$/d from the upper 200 m, but they noted that estimates of Mn benthic flux (the ultimate source of Mn for offshore transport) have been as low as 1100 nmol/m$^2$/d from this area (Scholz et al., 2011). Black et al (2019) derived an offshore flux of 1,960 nmol/m$^2$/d. Normalizing our PPZ water column to 200m, we derive an average offshore Mn flux of ~750 nmol/m$^2$/d.

*Iron*- Unlike dissolved Mn, there is no discernable horizontal gradient in the dissolved Fe

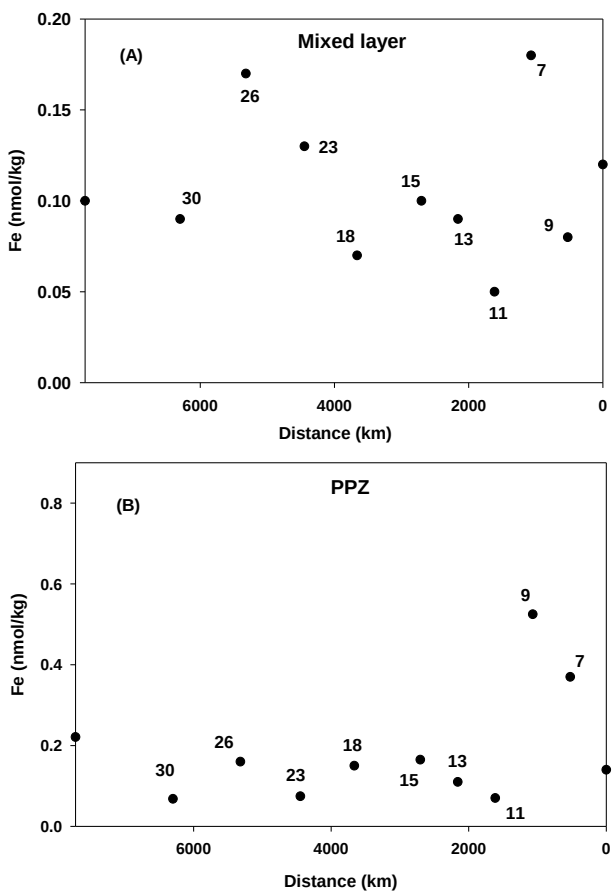


Figure 5.

A) Dissolved Fe plotted against distance from station 1 for the mixed layer across the EPZT.

B) Dissolved Fe plotted against distance from station 1 for the PPZ across the EPZT.

concentration field. (Figure 5). Therefore, there is no horizontal component of flux. Nearshore removal processes are more intense for dissolved Fe than for dissolved Mn (Landing and Bruland, 1987). Fe(II), supplied by porewater diagenesis, is rapidly oxidized via abiotic reactions in the presence of oxygen (Millero et al. 1987) and is thus rapidly attenuated nearshore to the South American continent, while the kinetically inhibited dissolved Mn must await microbially-catalyzed oxidation and thus persists farther offshore.

*Copper*- For the mixed layer, as with Mn, there is a relatively steep gradient in concentrations leaving the coastal zone, with a diminished gradient further offshore into the open ocean (Figure 6). At the depth of the PPZ there is also a steep decline in concentration nearshore, although the gradient is not as well-defined as in the mixed layer. Further offshore, there appears to be a small increase in Cu concentration

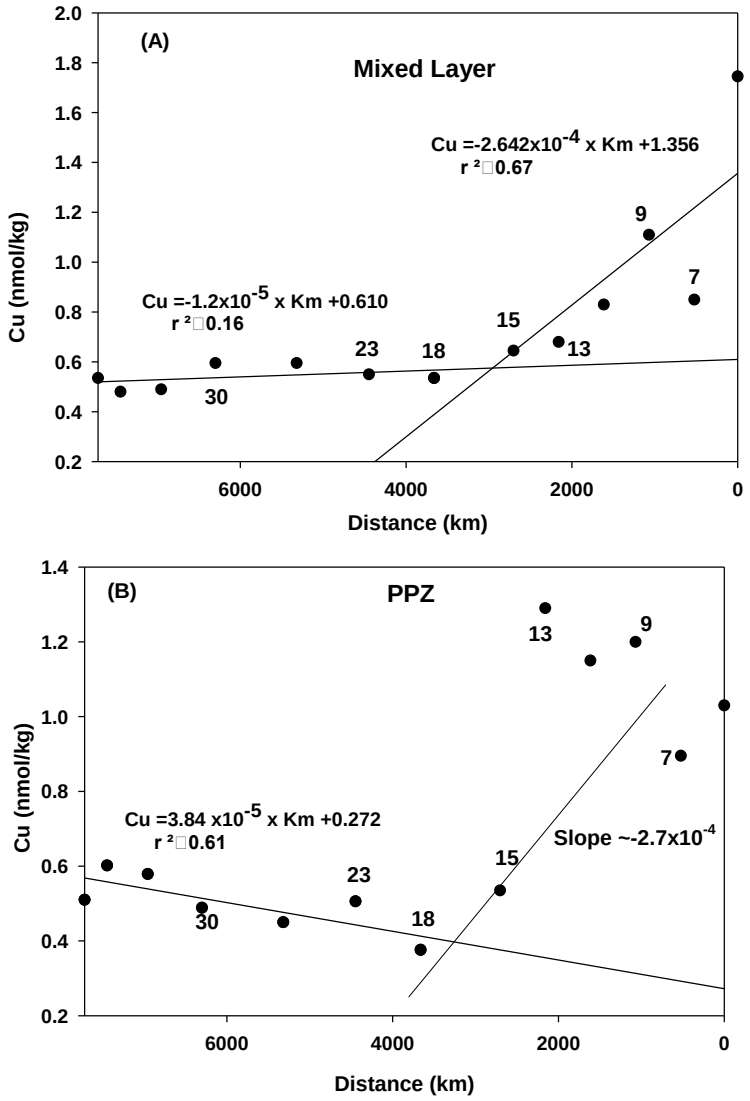


Figure 6.

A) Dissolved Cu plotted against distance from station 1 for the mixed layer across the EPZT.

B) Dissolved Cu plotted against distance from station 1 for the PPZ across the EPZT.

going westward, which may be related to the fact that the seaward transect is bearing somewhat northwest, back above more Cu-rich subsurface waters.

*Lead* – As with Mn and Cu, within the mixed layer there is a relatively steep gradient in dissolved Pb concentrations leaving the coastal zone, with a diminished gradient further offshore into the open ocean (Figure 7). At the depth of the PPZ there is also a steep near-shore decline in Pb concentration although the gradient is less well-defined.

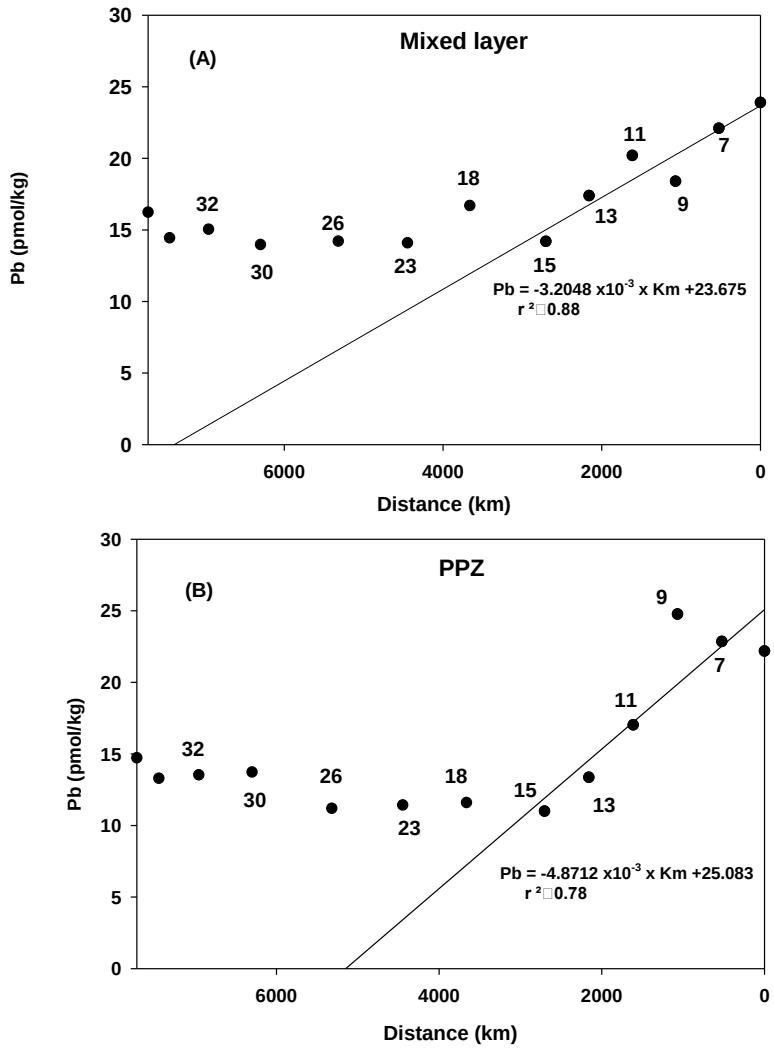


Figure 7.

A) Dissolved Pb plotted against distance from station 1 for the mixed layer across the EPZT.

B) Dissolved Pb plotted against distance from station 1 for the PPZ across the EPZT.

*Cadmium* – Dissolved Cd concentrations within the mixed layer and the PPZ show a relatively steep gradient in dissolved Cd concentrations leaving the coastal zone, with no discernible gradient offshore into the open ocean (Supplemental Figure 3).

*Vanadium* - The dissolved V concentration field has no discernable horizontal gradient (Supplemental Figure 4).

**Table 5a TE fluxes into the mixed layer**

| | ML flux **Fe** nmol/m2/d | | | | ML Flux **Mn** nmol/m2/d | | | | ML Flux **Cu** nmol/m2/d | | | | ML Flux **Pb** nmol/m2/d | | | |
|---|---|---|---|---|---|---|---|---|---|---|---|---|---|---|---|---|
| | Diffusive | Upwelling | atmosphere | Horizontal | Diffusive | Upwelling | atmosphere | Horizontal | Diffusive | Upwelling | atmosphe | Horizontal | Diffusive | Upwelling | atmosphe | Horizontal |
| sta | | | (BULK) | | | | (BULK) | | | | (BULK) | | | | (BULK) | |
| 1 | 198 | 968 | 829 | 0 | 257 | 13024 | 16.48 | 0 | 367 | 3872 | 11.63 | 0 | -3.2 | 105 | 1.69 | 0 |
| 7 | 0 | 117 | 829 | 0 | -119 | 3627 | 16.48 | 253 | 109 | 1131 | 11.63 | 104 | -0.29 | 29 | 1.69 | 1258 |
| 9 | 0.0 | 195 | 829 | 0 | 392 | 5070 | 16.48 | 289 | -318 | 1545 | 11.63 | 119 | -2.4 | 27.6 | 1.69 | 1438 |
| 11 | 8.4 | 2 | 829 | 0 | 122 | 82 | 16.48 | 245 | -112 | 40.6 | 11.63 | 100 | -17.6 | 0.8 | 1.69 | 1217 |
| 13 | 12.7 | -12 | 829 | 0 | 38.1 | -243.6 | 16.48 | 234 | 622 | -79.2 | 11.63 | 96 | 1.3 | -2 | 1.69 | 1161 |
| 15 | 34.8 | 15 | 829 | 0 | 0.0 | 237 | 16.48 | 406 | 4.4 | 87.8 | 11.63 | 167 | -0.8 | 2 | 1.69 | 2018 |
| 18 | -12.0 | 0 | 70.96 | 0 | 178 | 0 | 0.98 | 217 | -6.0 | 0 | 1.35 | 89 | -1.12 | 0 | 0.46 | 0 |
| 23 | -40.1 | 0 | 73.3 | 0 | 64.1 | 0 | 1.01 | 33 | 0.0 | 0 | 1.39 | 4 | -0.6 | 0 | 0.48 | 0 |
| 26 | 0.0 | 0 | 85.52 | 0 | 8.6 | 0 | 1.18 | 44 | -4.1 | 0 | 1.62 | 5 | 0.07 | 0 | 0.56 | 0 |
| 30 | -9.8 | 0 | 84.5 | 0 | 17.9 | 0 | 1.17 | 60 | -4.2 | 0 | 1.6 | 7 | -0.04 | 0 | 0.55 | 0 |
| 32 | 4.6 | 0 | 103.51 | 0 | 13.0 | 0 | 1.43 | 69 | -1.1 | 0 | 1.96 | 8 | -0.05 | 0 | 0.67 | 0 |
| 34 | 25.6 | 0 | 154.37 | 0 | 6.4 | 0 | 2.13 | 34 | 0.0 | 0 | 2.93 | 4 | -0.44 | 0 | 1.00 | 0 |
| 36 | 42.3 | 0 | 198.31 | 0 | 43.0 | 0 | 2.74 | 45 | -19.3 | 0 | 3.76 | 5 | -0.1 | 0 | 1.29 | 0 |

**Table 5b TE fluxes into the PPZ**

| | PPZ Flux Fe nmol/m2/d | | | | PPZ Flux Mn nmol/m2/d | | | | PPZ Flux Cu nmol/m2/d | | | | PPZ Flux Pb nmol/m2/d | | | |
|---|---|---|---|---|---|---|---|---|---|---|---|---|---|---|---|---|
| | Diffusive | Upwelling | atmosphere | Horizontal | Diffusive | Upwelling | atmosphere | Horizontal | Diffusive | Upwelling | atmosphe | Horizontal | Diffusive | Upwelling | atmosphe | Horizontal |
| | | | (BULK) | | | | (BULK) | | | | (BULK) | | | | (BULK) | |
| sta | | | | | | | | | | | | | | | | |
| 1 | 144 | 462 | 829 | 0 | -558 | 10230 | 16.48 | 0 | 252 | 3399 | 11.63 | 0 | 120 | 73.2 | 1.69 | 0 |
| 7 | 702 | 277.5 | 829 | 0 | -2049 | 2002.5 | 16.48 | 405 | 72.5 | 671.25 | 11.63 | 158.0 | 2.80 | 17.1 | 1.69 | 2278 |
| 9 | 444 | 357 | 829 | 0 | 913 | 1849.6 | 16.48 | 471 | 383 | 816 | 11.63 | 119 | -0.31 | 16.8 | 1.69 | 2658 |
| 11 | 50.0 | 0.35 | 829 | 0 | 71.9 | 5.4 | 16.48 | 514 | -55.3 | 5.75 | 11.63 | 100 | 0.26 | 0.1 | 1.69 | 3026 |
| 13 | 84.1 | -0.77 | 829 | 0 | 337 | -8 | 16.48 | 559 | -13.3 | -9 | 11.63 | 96 | 3.28 | -0.1 | 1.69 | 3349 |
| 15 | 109 | 2 | 829 | 0 | -413 | 10 | 16.48 | 436 | -22 | 5.35 | 11.63 | 277 | -1.22 | 0.1 | 1.69 | 4017 |
| 18 | -33.3 | 0 | 71.0 | 0 | -229 | 0 | 0.98 | 259 | 2.8 | 0 | 1.35 | 246 | 0.76 | 0 | 0.46 | 0 |
| 23 | 12.0 | 0 | 73.3 | 0 | -267 | 0 | 1.01 | 53.7 | -2.0 | 0 | 1.39 | 4 | -0.41 | 0 | 0.48 | 0 |
| 26 | 0.0 | 0 | 85.5 | 0 | -21.5 | 0 | 1.18 | 62.7 | -7.2 | 0 | 1.62 | 5.4 | -0.09 | 0 | 0.56 | 0 |
| 30 | -1.6 | 0 | 84.5 | 0 | -4.8 | 0 | 1.17 | 92.1 | -4.8 | 0 | 1.6 | 7.3 | 0.03 | 0 | 0.55 | 0 |
| 32 | 0.935 | 0 | 103.5 | 0 | -6.1 | 0 | 1.43 | 80.3 | -1.1 | 0 | 1.96 | 8.4 | -0.05 | 0 | 0.67 | 0 |
| 34 | 5.12 | 0 | 154 | 0 | -59.4 | 0 | 2.13 | 55.3 | -10.6 | 0 | 2.93 | 4.1 | -0.26 | 0 | 1.00 | 0 |
| 36 | 13.0 | 0 | 198 | 0 | -32.3 | 0 | 2.74 | 65.0 | -7.2 | 0 | 3.76 | 5.5 | -0.17 | 0 | 1.29 | 0 |

a. Horizontal fluxes based on an east-to-west mixed layer velocity of 0.1m/s.

## 3.2. Residence Time Calculations.

The residence time of the TEs were calculated using eqns. 9 and 10, the flux data from Table 5, the aerosol solubility data of Table 3, and the TE inventories in Table 6. The results are presented in Table 7. Note that only the positive flux values in Table 5 are used to calculate the residence times with respect to input fluxes. We consider the residence time of each element within the mixed layer and PPZ, using solubilities based on both the DI and HAc leaching methods.

*Manganese*- There is not a significant difference between the solubility of aerosol Mn determined by the DI and HAc leach methods, and as discussed below, the atmospheric input of soluble Mn along this transect is minor compared to the other inputs. Consequently, the residence times based on solubilities determined by either method are nearly identical (Table 7).

For nearshore stations 1,7, and 9 the dissolved Mn residence times within the mixed layer range from 10 to 29 days and average 22 ±10 days, requiring intense removal processes in the nearshore upwelling zone to keep the dissolved Mn distribution at steady-state. The Mn residence times within the

mixed layer for stations 11-18 range from 89 to 294 days, with an average of 188 ±84 days. This is comparable to the 0.4 y nearshore scavenging residence time derived by Landing and Bruland (1987) for the Central California coast using a one-dimensional advection-diffusion approach and to the 0.22-1.8 y residence time for the upper 150 m of the central North Pacific calculated by comparing surface inventories to sediment trap fluxes (Martin & Knauer, 1980).

However, residence times based on the $^{234}$Th-derived particulate export flux of Mn at 100m depth along the EPZT transect ranged from 1.5 - 3 y, considerably longer than this (Black et al. 2019). This is likely because the Mn flux determined by the $^{234}$Th method cannot account for lateral removal of Mn from upwelling zones which would lead to a lower apparent total Mn export flux. It has been suggested for example that the export flux of POC determined by the $^{234}$Th method underestimates primary production (Kadko, 2017), as export production can become spatially decoupled from new production. This is because a fraction of the newly produced organic material can be transported laterally before leaving the euphotic zone, a process known to be particularly important in dynamic coastal upwelling systems (Plattner et al., 2005). Here we calculate the input flux (upwelling, atmospheric deposition, and diffusion) of Mn at station 1 to be ~13300 nmol/m$^2$/d (Table 5a) while Black et al., (2019) report an export flux of only 1000 nmol/m$^2$/d. Clearly, there is a decoupling between surface production and export flux at these eastern sites. These authors acknowledge that if net dissolved TE removal via offshore transport exceeds the particulate TE export flux, then their residence times would be an upper limit. Their residence time applies only to the specific removal process arising from the vertical export of particles.

For the offshore stations 23-36, dissolved Mn residence times increase to the range of 337 to 572 days with an average of 490 ± 150 days. This is comparable to the 1.9 y reported by Black et al. (2019) for the gyre region of this study where decoupling of new production and export flux does not occur. This estimate is shorter than the 19 y residence time presented in Landing and Bruland (1987) where the lack of strong westward advection off the Central California coast into the North Pacific results in much longer Mn residence times. Our results are consistent with Figure 4a, where the steeper gradient for the nearshore stations suggests more rapid Mn removal within the upwelling environment. The longer Mn residence time at the open ocean stations is comparable to the advective timescale of 580 days for the transport 5000 km offshore to the central gyre (with a velocity of 0.1m/s) and is consistent with the diminishment of the $^{228}$Ra signal (Sanial et al., 2018).

Over the PPZ, nearshore (stations 1,7, and 9) residence times range from 20 to 111 days, with an average of 79 ± 51 days. For the stations 11-18, residence times range from 297 to 757 days averaging 506 ± 197days. For the gyre stations 23-36, residence times of the PPZ range from 1180 to 2970 days with an average of 1780 ± 690 days. The average residence times of Mn for the open ocean mixed layer (1.3 y) and the PPZ (5 y) are comparable to the lower end of the 5-20 year Mn residence times discussed in Shiller (1997) and the 5-6 year range modeled by Wu et al (2014) for a depth of 200m (~depth of the

PPZ in this study) in the N. Pacific and the N. Atlantic based on Mn oxidation rates. The maximum PPZ residence times are more comparable to the 9.6-11 y residence times estimated by comparing dissolved Mn seawater inventories with aerosol fluxes (Jickells 1999).

As described in section 3.1, a value of 0.1 m/s has been chosen for the ocean horizontal velocity (hence the horizontal flux) calculations. The sensitivity of the residence times to this parameter is illustrated in Figure 8. For current speeds between 0.05 and 0.5 m/s (range of a factor of 10), the Mn residence times for the mixed layer (Figure 8a) of upwelling stations 1,7, and 9 range within a factor of only ≤ 1.2 as vertical transport terms dominate the input flux. For stations to the west (11-36), the residence time range is between a factor of 2.8-7.5 since the horizontal flux term has greater relative importance. As current speed increases the residence time decreases for all stations. For the PPZ (Figure 8b), the Mn residence times for upwelling stations 1,7, and 9 range over a factor of ≤ 1.5. For stations to the west (11-36) the range is between a factor of 2.3-8.4.

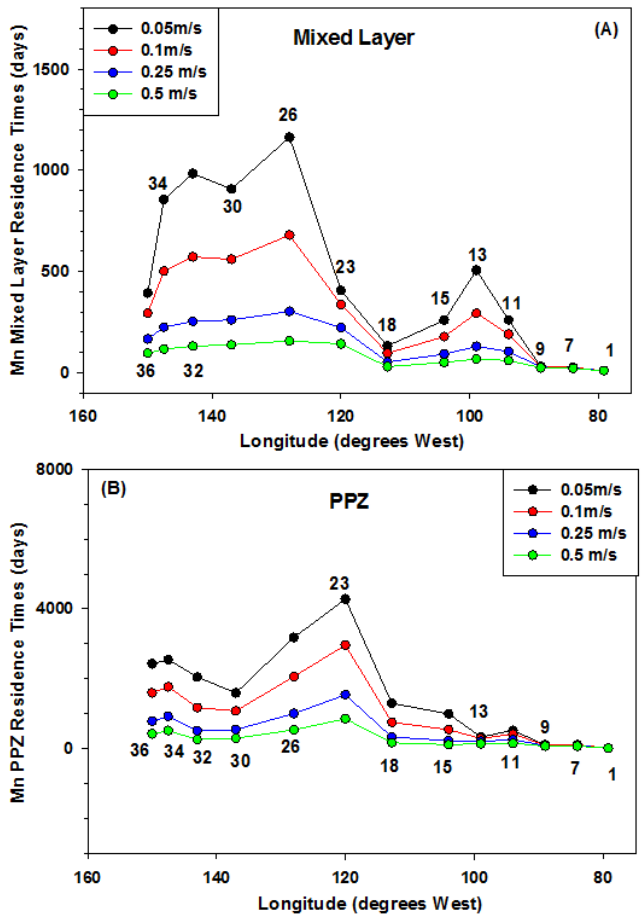


Figure 8.
The relationship of the residence time of dissolved Mn to surface horizontal current velocity for A) the mixed layer and B) the PPZ.

Relative to other inputs the atmospheric input of soluble Mn is only of minor consequence in these calculations. Nearshore, where the atmospheric input of TEs are greatest, the upwelling Mn source is dominant. Within the gyre, the total input flux decreases and horizontal flux dominates Mn input into

these surface waters (Sanial et al., 2018; Black et al., 2019). Zheng et al. (2019) suggest sources other than aerosols are more significant contributors to Mn in the N. Pacific as well, and Kadko et al (2019) show that atmospheric deposition of Mn is insignificant relative to other inputs in the Arctic Ocean

*Iron*- The observed Fe characteristics differ from those of Mn in two distinct ways. First, the DI and HAc aerosol Fe solubilities are appreciably different. Second, atmospheric Fe input is significant relative to other input terms within the gyre. For nearshore stations 1, 7, and 9 the Fe residence times within the mixed layer using the two leaching methods are similar because the upwelling input of Fe is more significant than the atmospheric input. Using the DI water solubility, residence times range from 5 to 40 days, averaging 25 ± 18 days, and using the HAc solubility the range is from 4.6 to 22 days, averaging 13.0 ± 8.6 days. These short residence times indicate intense removal processes in the nearshore upwelling zone. Despite the relatively large dust input for these stations, the DI soluble atmospheric Fe input is < 4%, and the HAc soluble input is <60% of the total input from all sources. A similar conclusion was drawn by Buck et al. (2019) for these same stations and by Fitzsimmons et al. (2016) for stations farther south but equally close to the South American continent.

Moving offshore, but still in the zone of upwelling (stations 11,13, and 15), the average residence time increases to 140 ± 100 and 23 ± 8.5 days with the DI and HAc solubilities, respectively. Upwelling is diminished in importance, and the atmospheric soluble input is ~6% of the total Fe input flux using the DI solubility and as high as 94% with the HAc solubility. For the stratified mid-gyre stations 18-32 upward turbulent diffusion is limited (Fig 3) and the total Fe input is relatively small compared to the inshore stations. The choice of solubility in the residence time calculation is therefore critical as the atmospheric delivery of Fe becomes the dominant input term. The resulting average residence time using the DI solubility ~ 11 y which is much longer than the 290±110 days based on the HAc solubility. The shorter HAc-based residence time is more consistent with most surface dissolved Fe residence times reported in the literature (e.g. Jickells et al. 1999; Croot et al., 2004; Boyle et al., 2005; Bergquist and Boyle 2006; Hayes et al. 2015) except for that reported in the Arctic (Kadko et al., 2019) where low particle scavenging likely occurs.

As discussed elsewhere (e.g., Aguilar-Islas et al., 2010; Sholkovitz et al. 2012), provenance, more than leaching methodology, determines the fractional solubility of aerosol Fe, with anthropogenic Fe being more readily soluble relative to mineral Fe. In the gyre area of this region characterized by minimal mineral dust deposition, the soluble Fe is likely dominated by highly soluble anthropogenic or pyrogenic sources (Conway et al., 2019; Ito et al., 2019). Higher solubilities obtained from the HAc method might be more representative of the actual solubility of aerosol Fe in seawater, as the heating step, reducing conditions, and lower pH of the HAc method may artificially account for time-dependent Fe dissolution pathways, such as those supported by naturally occurring organic Fe-binding ligands in seawater, and the

conditions particles experience during passage through a zooplankton gut or inside a fecal pellet or organic aggregate (Shelley et al., 2018).

In the westernmost stations, moving out of the gyre, atmospheric input increases, and stratification is relaxed resulting in enhanced turbulent diffusion. These factors contribute to shorter dissolved Fe residence times for stations 34 and 36. Using the DI solubility, these are 113 and 71 days, respectively, and with the HAc solubility, 52 and 37 days.

For the PPZ, using the DI solubility, the Fe residence times for the nearshore stations 1,7, and 9 range from 11-29 days, and average 19 ± 9 days, and using the HAc solubility range from 9 to 24 days, and average 16 ± 8 days. These residence times are similar because of the dominance of the upwelling and diffusive terms compared to the atmospheric input. As with the mixed layer calculation, the residence time increases for stations 11, 13, and 15, averaging 153 ± 6 days using the DI solubility and 53 ± 13 days using the HAc solubility. For the stratified mid-gyre stations 18-32 the average residence time increases to 30 ± 34 y using the DI solubility and to 2.3 ± 1.2 y using the HAc solubility. Moving out of the gyre, the residence times for stations 34 and 36 are 6.6 and 4.4 y, respectively using the DI solubility. Both stations have a residence times of 1.2 y with the HAc leach. As discussed above, the HAc solubilities appear to be more appropriate for Fe in these calculations.

*Copper*-The HAc solubility is ~twice that based on the DI leach but the soluble atmospheric flux across the transect is relatively small compared to other inputs into the mixed layer, contributing < 1% to 16% of the total Cu input into the mixed layer using the DI solubility, and < 1% to 31% with the HAc solubility, increasing in both cases towards the western edge of the transect. Thus the choice of aerosol leach solubility is not critical in these calculations.

The average mixed layer residence time of Cu for nearshore stations 1,7, and 9 is 25 ± 11 days using both the DI and HAc solubilities. Moving offshore, but still in the zone of upwelling (stations 11, 13, and 15), the average residence time increases to 0.50 ± 0.37 y for both solubilities. For the stratified mid-gyre stations 18-32 the average residence time increases to 11.5 ± 6.2 y using the DI solubility which is not significantly greater than the 10.4 ± 5.6 y using the HAc solubility. The increase of residence time within the gyre reflects diminished input from upward diffusion and a smaller advective input term (smaller gradient, Figure 6a). For stations 34 and 36, just outside of the gyre to the west, the residence time based on the DI leach is 11.4 ± 1.35 y which again is not significantly different than the 9.3 ± 1.1 y based on the HAc solubility. For comparison, Bruland (1980) derived a dissolved Cu surface residence time with respect to atmospheric deposition of 10 years, and Boyle et al. (1977) estimated 2.1-50 years with respect to scavenging, both for surface waters of the North Pacific.

For the PPZ, there is generally a similar pattern, with the nearshore stations 1, 7, and 9 manifesting an average Cu residence time of 66 ± 40 days, using both solubilities. The residence times increase to an average of 2.5 ± 1.3 y for offshore stations 11, 13, and 15, again using both solubilities. For stations 18-

36, using the DI solubility, the residence times range from 0.9-62 y, averaging 38 ± 22y. For the HAc solubility, the residence times range from 0.9-56 y, averaging 33 ± 20y.

The upwelling of Cu at stations 1, 7 and 9 is the largest component of Cu flux anywhere along the EPZT transect. It has been reported that the stability constant for Cu-binding ligands at these nearshore stations is an order of magnitude greater than those of stations further offshore (Boiteau et al., 2016) suggesting the possibility that organisms have upregulated genes to produce these high-K ligands to protect against Cu toxicity associated with the high rate of Cu supply by upwelling.

*Lead*- The concentrations of aerosol Pb across the EPZT were too low to allow reliable determination of solubilities. We use instead the aerosol solubilities of marine background samples presented in Shelley et al. (2018). Average DI and HAc solubilities were respectively, 33% and 63%. The average mixed layer residence time of Pb for nearshore stations 1-15 was 2 ± 3.5 days using both the DI and HAc solubilities. These very short residence times are indicative of intense scavenging removal processes in the nearshore upwelling zone as observed for other TEs discussed here. Upwelling and horizontal advection were the dominant input components for these stations. Moving out to the open ocean gyre stations 18-36, the total input of Pb to the upper ocean was very small compared to the inshore stations (Table 5) with atmospheric input dominant. With the HAc solubility, average residence times were 5.2 ± 2.1 y which is consistent with estimates of 2-3 y presented elsewhere (Bruland, 1980; Nozaki et al., 1976). With the DI solubility the average residence time was 9.8 ± 5.1 y.

**Table 6. Mixed layer and PPZ TE inventories (nmol/m²)**

| station | Fe ML | Fe PPZ | Mn ML | Mn PPZ | Cu ML | Cu PPZ | Pb ML | Pb PPZ |
|---|---|---|---|---|---|---|---|---|
| 1 | 6145 | 10863 | 131375 | 202680 | 52137 | 73867 | 972 | 1518 |
| 7 | 3796 | 10608 | 124786 | 269037 | 41167 | 84228 | 950 | 2023 |
| 9 | 8290 | 23901 | 169883 | 341952 | 53471 | 112356 | 990 | 2225 |
| 11 | 3155 | 9091 | 86439 | 250776 | 43451 | 132174 | 740 | 2180 |
| 13 | 3785 | 15264 | 81531 | 267501 | 27792 | 122892 | 650 | 2325 |
| 15 | 7646 | 18666 | 115687 | 248070 | 55085 | 107899 | 1090 | 2280 |
| 18 | 2635 | 17193 | 37990 | 196395 | 85932 | 21609 | 645 | 2380 |
| 23 | 4806 | 12776 | 32916 | 160501 | 24723 | 100809 | 549 | 2220 |
| 26 | 8585 | 26786 | 36231 | 130590 | 32650 | 95026 | 740 | 2246 |
| 30 | 3970 | 8327 | 43677 | 100201 | 34758 | 68028 | 986 | 1913 |
| 32 | 8575 | 18017 | 47165 | 95115 | 44667 | 85736 | 1195 | 2224 |
| 34 | 3145 | 17436 | 20706 | 99552 | 18917 | 92410 | 590 | 2525 |
| 36 | 3218 | 25217 | 26207 | 105635 | 29501 | 98935 | 817 | 2777 |

For the PPZ, there is generally a similar pattern, with the residence time of Pb for nearshore stations 1-15 manifesting an average of 1.9 ± 2.9 days, using both solubilities. The residence times increase to an

| | Table 7. Trace Element Residence Times (days) | | | | | | | | | | | | | | | |
|---|---|---|---|---|---|---|---|---|---|---|---|---|---|---|---|---|
| | Mixed Layer[b] | | | | | | | | PPZ[b] | | | | | | | |
| Station | Fe | | Mn[a] | | Cu[a] | | Pb[a] | | Fe | | Mn[a] | | Cu[a] | | Pb[a] | |
| | DI | HAc | DI | HAc | DI | HAc | DI | HAc | DI | HAc | DI | HAc | DI | HAc | DI | HAc |
| 1 | 5.2 | 4.6 | 9.9 | 9.9 | 12.3 | 12.3 | 9.2 | 9.2 | 17.6 | 13.7 | 19.8 | 19.8 | 20.2 | 20.2 | 9.2 | 9.2 |
| 7 | 29.5 | 13 | 32.1 | 32.1 | 30.6 | 30.5 | 0.8 | 0.8 | 10.7 | 9.1 | 111 | 111 | 93 | 93 | 0.8 | 0.7 |
| 9 | 40.1 | 22 | 29.4 | 29.5 | 32.1 | 32.0 | 0.7 | 0.7 | 29.4 | 24.2 | 106 | 105 | 85 | 85 | 0.7 | 0.7 |
| 11 | 143 | 16 | 190 | 189 | 301 | 292 | 0.6 | 0.6 | 147 | 39 | 420 | 419 | 1209 | 1162 | 0.6 | 0.6 |
| 13 | 156 | 20 | 294 | 292 | 38.5 | 38.3 | 0.6 | 0.6 | 159 | 57 | 297 | 296 | 1241 | 1188 | 0.6 | 0.6 |
| 15 | 125 | 33 | 178 | 178 | 210 | 207 | 0.6 | 0.6 | 153 | 63 | 550 | 547 | 377 | 372 | 0.6 | 0.5 |
| 18 | 2652 | 166 | 89 | 89 | 242 | 241 | 4249 | 2226 | 17307 | 1084 | 757 | 756 | 344 | 344 | 4249 | 2226 |
| 23 | 4683 | 293 | 337 | 337 | 5583 | 4988 | 3466 | 1815 | 981 | 450 | 2968 | 2962 | 22763 | 20337 | 3466 | 1815 |
| 26 | 7170 | 449 | 680 | 678 | 5591 | 5057 | 2882 | 1742 | 22370 | 1400 | 2068 | 2064 | 16270 | 20228 | 2882 | 1742 |
| 30 | 3356 | 210 | 560 | 559 | 4490 | 4162 | 5433 | 2846 | 7037 | 441 | 1083 | 1082 | 8852 | 8187 | 5433 | 2846 |
| 32 | 1418 | 309 | 572 | 572 | 4996 | 4611 | 5405 | 2831 | 7670 | 750 | 1177 | 1174 | 9589 | 8852 | 5405 | 2831 |
| 34 | 113 | 52 | 502 | 499 | 3815 | 3115 | 1788 | 937 | 2400 | 440 | 1774 | 1767 | 18636 | 15218 | 1788 | 937 |
| 36 | 71.4 | 37 | 294 | 293 | 4513 | 3704 | 1919 | 1007 | 1600 | 440 | 1600 | 1593 | 15136 | 12420 | 1919 | 1005 |

a. Based on horizontal mixed layer velocity of 0.1 m/s

b. In each column residence times are shown based on the DI and HAc solubility.

average of 13.2 ± 4.9 y for offshore stations 18-36 using the HAc solubility and 24.3± 10.5 y using the DI solubility.

*Cadmium and Vanadium*- The relevant information for these elements are shown in Supplemental Tables 1-3.

## 4.0 Conclusions

The TE fluxes from atmospheric deposition, vertical mixing, and upwelling into the mixed layer and the PPZ along the GEOTRACES EPZT were evaluated with $^{7}$Be-based methods developed in earlier works. Horizontal advection velocity from east to west, driven by the South Equatorial Current, was estimated from literature values and when horizontal gradients in the TE distributions were observed, fluxes due to horizontal advection were determined. Atmospheric deposition is lowest in the central gyre, with higher fluxes to the east due to large near-shore aerosol TE loads, and higher to the west due to higher deposition velocities ($V_b$) driven by greater precipitation. The $^{7}$Be-derived $K_z$ values range from 2.5 to 39 $m^2/d$ (0.29 x $10^{-4}$ to 4.5 x $10^{-4}$ $m^2/s$) with higher values generally within the nearshore upwelling region and the lowest values within the stratified central gyre. Mn displayed a well-defined gradient extending from the nearshore stations into the central gyre. Even with a modest choice of horizontal velocity the advective term was a major component of the total input flux, particularly within the central gyre. Relative to other inputs the atmospheric input of soluble Mn was minor. Unlike manganese, there

was no discernable horizontal gradient in the Fe concentration field and therefore there is no horizontal component of flux. Nearshore removal processes were more intense for dissolved Fe than for dissolved Mn and as a result, dissolved Mn remained elevated much farther offshore than dissolved Fe. For the stratified mid-ocean gyre stations upward turbulent diffusion of Fe was limited and atmospheric deposition became dominant, although the total input from all sources was relatively small compared to the inshore stations. Aerosol Fe solubility determined by a 25% acetic acid leach with hydroxylamine hydrochloride was much greater than that derived from a leach using ultrapure deionized water. This led to significant differences in the residence time of Fe calculated for the mid-ocean gyre depending on the aerosol fractional solubility chosen for the calculation. For Cu, Cd, and Pb, as with Mn, within the mixed layer there is a relatively steep gradient in concentrations leaving the coastal zone.

The residence times of the TEs calculated with the measured water column inventories and the input fluxes discussed above reflected the significantly different physical and geochemical conditions encountered across the zonal transect. Generally, each element displayed realtively short (days-weeks) residence times within the nearshore region of intense upwelling, reflecting large input terms and rapid removal. Moving offshore, total input fluxes decreased and the residence times of the TEs increased markedly until the western edge of the transect. There, relaxtion of ocean stratification permited greater upward turbulent flux and greater rainfall led to greater atmospheric input of the trace elements. These results suggest that one size does not fit all when considering ocean residence times as there is a range of scavenging removal pathways for different elements as well as natural gradients in oceanic fluxes. Regional difference should be expected.

As discussed in Twining and Baines (2013), trace metals can influence the growth and structure of natural phytoplankton communities and, conversely, the composition and structure of phytoplankton communities influence the distribution of metals in the ocean. The metal contents of phytoplankton reflect biochemical demands and environmental availability. The ambient trace metal distributions reflect the complex interplay between external sources, microbial uptake and recycling, and physical mixing. Studies of the sources and residence times of these elements across diverse oceanic settings, as discussed here, will provide further insight into the relationship between trace element abundance and phytoplankton community structure.

**Acknowledgements.** The authors thank the captain and crew of R/V Thomas G. Thompson, and the Chief Scientists Dr. Chris German and Dr. Jim Moffett for their support. Dr. Mark Stephens provided important at-sea and laboratory technical assistance. Data has been submitted to The Biological and Chemical Oceanography Data Management Office (BCO-DMO) and is accessible at: http://www.bco-dmo.org/dataset/665158. This work was supported by the Chemical Oceanography Program of the NSF,

grants OCE-1232794 (DK), OCE-1454368 (CB), OCE-1234417 (AAI), OCE-1234646 (WML) and OCE 1233502 (KWB)..

## References

Aguilar-Islas A.M, Wu J, Rember R., Johansen A.M., Shank L.M. (2010) Dissolution of aerosol-derived iron in seawater: Leach solution chemistry, aerosol type, and colloidal iron fraction. Mar Chem;120:25-33, doi:10.1016/j.marchem.2009.01.011.

Anderson, R. F., H. Cheng, R. L. Edwards, M. Q. Fleisher, C. T. Hayes, K.-F. Huang, D. Kadko, P. J. Lam, W. M. Landing, Y. Lao, Y. Lu, C. I. Measures, P. L. Morton, S. B. Moran, D. C. Ohnemus, L. F. Robinson, R. U. Shelley (alphabetical order) (2016), How well can we quantify dust deposition to the ocean? Philosophical Transactions of the Royal Society A 374, DOI: 10.1098/rsta.2015.0285.

Berger, C. J. M., Lippiatt, S. M., Lawrence, M. G., and Bruland, K. W.: Application of a chemical leach technique for estimating labile particulate aluminum, iron, and manganese in the Columbia River plume and coastal waters off Oregon and Washington, J. Geophys. Res., 113, C00B01, https://doi.org/10.1029/2007JC004703, 2008.

Bergquist, B. A., and E. A. Boyle (2006), Dissolved iron in the tropical and subtropical Atlantic Ocean, Global Biogeochem. Cycles, 20, GB1015, doi:10.1029/2005GB002505.

Biller, D.V. and Bruland, K.W. (2012) Analysis of Mn, Fe, Co, Ni, Cu, Zn, Cd, and Pb in seawater using the Nobias-chelate PA1 resin and magnetic sector inductively coupled plasma mass spectrometry (ICP-MS). Marine Chemistry 130-131, 12-20.

Black, E. E., Lam, P. J., Lee, J.-M., and Buesseler, K. O. (2019). Insights from the 238U-234Th method into the coupling of biological export and the cycling of cadmium, cobalt, and manganese in the Southeast Pacific Ocean. Global Biogeochemical Cycles, 33, 15–36. https://doi.org/10.1029/2018GB005985.

Boiteau, R.M, Till C.P, Ruacho A, Bundy R.M., Hawco N.J, McKenna A.M, Barbeau K.A., Bruland K.W., Saito M.A., Repeta D.J. 2016. Structural characterization of natural nickel and copper binding ligands along the US GEOTRACES Eastern Pacific Zonal Transect. Frontiers in Marine Science. 3:243.

Boyle, E.A., F.R. Sclater and J.M. Edmond (1977). The distribution of dissolved copper in the Pacific. Earth and Planetary Science Letters, 37, 38-54.

Boyle E., Bergquist B., Kayser R, Mahowald N. (2005). Iron, manganese and lead at Hawaii Ocean Time-Series Station ALOHA: temporal variability and intermediate water hydrothermal plume. Geochim. Cosmochim. Acta 69:933–52.

Bridgestock, L., van de Flierdt, T. V., Rehkamper, M., Paul, M., Middag, R., Milne, A., Lohan, M. C., Baker, A. R., Chance, R., Khondoker, R., Strekopytov, S., Humphreys-Williams, E., Achterberg, E. P., Rijkenberg, M. J. A., Gerringa, L. J. A., and de Baar, H. J. W. (2016) Return of naturally sourced Pb to Atlantic surface waters, Nat. Commun., 7, 10.1038/ncomms12921.

Bruland, K. Oceanographic distributions of cadmium, zinc, nickel, and copper in the north Pacific (1980). Earth and Planetary Science Letters, 47, 176-198.

Buck, C.S., W.M. Landing, J.A. Resing, G.T. Lebon (2006). Aerosol iron and aluminum solubility in the northwest Pacific Ocean: Results from the 2002 IOC Cruise. Geochem. Geophys. Geosyst., 7, Q04M07, doi:10.1029/2005GC000977.

Buck, C.S., A. Aguilar-Islas, C. Marsay, D. Kadko, W. M. Landing (2019). Trace element concentrations, elemental ratios, and enrichment factors observed in aerosol samples collected during the US GEOTRACES eastern Pacific Ocean transect (GP16). Chemical Geology 511, 212–224.

Carr, M.-E. (2001) Estimation of potential productivity in Eastern Boundary Currents using remote sensing. Deep Sea Research Part II: Topical Studies in Oceanography 49, 59-80.

Claustre, H., Sciandra, A. and Vaulot, D. (2008) Introduction to the special section bio-optical and biogeochemical conditions in the South East Pacific in late 2004: the BIOSOPE program. Biogeosciences 5, 679-691.

Conway, T.M., D.S. Hamilton, R.U. Shelley, A.M. Aguilar-Islas, W.M. Landing, N.M. Mahowald, and S.G. John. (2019). Tracing and constraining anthropogenic aerosol iron fluxes to the North Atlantic Ocean using iron isotopes. Nature Communications 10(1). https://doi.org/10.1038/s41467-019-10457-w

Croot, P.L., P. Streu, and A. R. Baker (2004) Short residence time for iron in surface seawater impacted by atmospheric dry deposition from Saharan dust events. Geophysical res. let, vol. 31, doi:10.1029/2004GL020153.

Cutter, G.A. and Bruland, K.W. (2012) Rapid and noncontaminating sampling system for trace elements in global ocean surveys. Limnol. Oceanogr. Meth. 10, 425–436.

Cutter, G.A., Moffett, J.W., Nielsdóttir, M.C. and Sanial, V. (2018) Multiple oxidation state trace elements in suboxic waters off Peru: In situ redox processes and advective/diffusive horizontal transport. Marine Chemistry 201, 77-89.

GEOTRACES_Planning_Group (2006), Science Plan, Scientific Committee on Oceanic Research, Baltimore, Maryland.

Fitzsimmons, J.N., Conway, T.M., Lee, J.-M., Kayser, R., Thyng, K.M., John, S.G. and Boyle, E.A. (2016) Dissolved iron and iron isotopes in the Southeastern Pacific Ocean. Global Biogeochem. Cycles 30.

Fitzsimmons, J.N., John, S.G., Marsay, C.M., Hoffman, C.L., Nicholas, S.L., Toner, B.M., German, C.R., Sherrell, R.M. (2017) Iron persistence in a distal hydrothermal plume supported by dissolved-particulate exchange. Nature Geoscience 10 (3), 195.

Haskell, W.Z., Kadko, D., Hammond, D.E., Knapp, A.N., Prokopenko, M.G., Berelson, W.M., Capone, D.G., (2015). Upwelling velocity and eddy diffusivity from 7Be measurements used to compare vertical nutrient flux to export POC flux in the Eastern Tropical South Pacific. Mar. Chem. 168, 140–150.

Hayes, C.T., J.N. Fitzsimmons, E.A. Boyle, D. McGee, R.F. Anderson, R. Weisend, P. L. Morton (2015) Thorium isotopes tracing the iron cycle at the Hawaii Ocean Time-series Station ALOHA. Geochimica et Cosmochimica Acta, 169, 1-16. doi.org/10.1016/j.gca.2015.07.019.

Ho, P., J. Lee, M. Heller, P. Lam, and A.M. Shiller. The distribution of dissolved and particulate Mo and V along the U.S. GEOTRACES East Pacific Zonal Transect (GP16): the roles of oxides and biogenic particles in their distributions in the oxygen deficient zone and the hydrothermal plume. Marine Chemistry 201: 242-255; doi: 10.1016 /j.marchem.2017.12.003.

Ito A., S. Myriokefalitakis, M. Kanakidou, N. Mahowald, R. Scanza, D. Hamilton, A. Baker, T. Jickells, M. Sarin, S. Bikkina, Y. Gao, R. Shelley, C. S. Buck, W. Landing, A. Bowie, M. Perron, C. Guieu, N. Meskhidze, M. Johnson, Y. Feng, J. Kok, A. Nenes, R. Duce. Pyrogenic iron: The missing link to high iron solubility in aerosols. Science Advances, 5 (5), eaau7671, doi: 10.1126/sciadv.aau7671

John, S.G., J. Helgoe, E. Townsend, T. Weber, T. DeVries, A. Tagliabue, K. Moore, P. Lam, C.M. Marsay, C.Till (2018) Biogeochemical cycling of Fe and Fe stable isotopes in the Eastern Tropical South Pacific. Marine Chemistry 201, 66-76

Jickells, T.D. (1999) The inputs of dust derived elements to the Sargasso Sea; a synthesis. Mar. Chem. 68, 5-14.

Haskell W.Z., D. Kadko, D.E. Hammond, M.G. Prokopenko, W.M. Berelson, A.N. Knapp and D. Capone (2015) Upwelling velocities and eddy diffusivity from 7Be measurements used to compare vertical nutrient fluxes to export POC flux in the Eastern Tropical South Pacific. Marine Chemistry. doi: 10.1016/j.marchem.2014.10.004. 168, 140–150.

Kadko, D. and D. Olson (1996) Be-7 as a tracer of surface water subduction and mixed layer history. Deep Sea Res. 43, 89-116.

Kadko, D., and W. Johns (2011) Inferring upwelling rates in the equatorial Atlantic using $^{7}$Be measurements in the upper ocean. Deep-Sea Res. I, 58, 247-257, doi:10.1016 /j.dsr. 2011. 03.004.

Kadko D., W. M. Landing, and R. U. Shelley (2015) A novel tracer technique to quantify the atmospheric flux of trace elements to remote ocean regions. Journ. Geophy. Res. Oceans, 119, doi:10.1002/2014JC010314.

Kadko D., B. Galfond, W. M. Landing, and R. U. Shelley (2016) Determining the Pathways, Fate, and Flux of Atmospherically Derived Trace Elements in the Arctic Ocean/Ice System. Marine Chemistry. 182, 38-50, doi:10.1016/j.marchem.2016.04.006.

Kadko, D. (2017) Upwelling and Primary Production during the U.S. GEOTRACES East Pacific Zonal Transect. Global Biogeochem. Cycles. 31, doi:10.1002/2016GB005554.

Kadko D., A. Aguilar-Islas, C. Bolt, C.S. Buck, J. N. Fitzsimmons, L. T. Jensen, W.M. Landing, C.M. Marsay, R. Rember, A. M. Shiller, L. M. Whitmore, and R. F. Anderson (2019) The residence times of trace elements determined in the surface Arctic Ocean during the 2015 US Arctic GEOTRACES expedition. Mar. Chem. 208, 56-69. doi.org /10.1016/ j.marchem. 2018.10.011.

Kadko, D., and J. Prospero (2011), Deposition of 7Be to Bermuda and the regional ocean: Environmental factors affecting estimates of atmospheric flux to the ocean, J. Geophys. Res., 116, C02013, doi:10.1029/2010JC006629.

Karstensen, J., Stramma, L. and Visbeck, M. (2008) Oxygen minimum zones in the eastern tropical Atlantic and Pacific oceans. Progress In Oceanography 77, 331-350.

Kim, G., L. Alleman, and T. Church (1999) Atmospheric depositional fluxes of trace elements, 210Pb and 7Be into the Sargasso Sea. Global Biogeochem. Cycles, 13, 1183-1192.

Krishnaswami, S., Lal, D., Somayajulu, B.L.K., Dixon, F.S., Stonecipher, S.A., and H. Craig, (1972). Silicon, radium, thorium and lead in seawater: in-situ extraction by synthetic fibre. Earth Planet. Sci. Lett. 16, 84–90.

Lal, D., Chung, Y., Platt, T., Lee, T., 1988. Twin cosmogenic radiotracer studies of phosphorus recycling and chemical fluxes in the upper ocean. Limnol. Oceanogr. 336, 1559–1567.

Lee, T., Barg, E., Lal, D., 1991. Studies of vertical mixing in the Southern California Bight with cosmogenic radionuclides 32P and 7Be. Limnol. Oceanogr. 365, 1044–1053.

Lee, J.-M., Boyle, E.A., Echegoyen-Sanz, Y., Fitzsimmons, J.N., Zhang, R. and Kayser, R.A. (2011) Analysis of trace metals (Cu, Cd, Pb, and Fe) in seawater using single batch Nitrilotriacetate resin extraction and isotope dilution inductively coupled plasma mass spectrometry. Analytica Chimica Acta 686, 93-101.

Lee, J.-M., Heller, M.I. and Lam, P.J. (2018) Size distribution of particulate trace elements in the U.S. GEOTRACES Eastern Pacific Zonal Transect (GP16). Marine Chemistry 201, 108-123.

Landing W.M. and K.W. Bruland (1987) The contrasting biogeochemistry of iron and manganese in the Pacific Ocean. Geochimica et Cosmochimica Acta, 51, Issue 1, 29-43.

Lumpkin, R., and G. C. Johnson (2013), Global ocean surface velocities from drifters : Mean, variance, El Nino–Southern Oscillation response, and seasonal cycle, J. Geophys. Res. Oceans, 118, 2992–3006, doi:10.1002/jgrc.20210.

Marsay, C.M., D. Kadko, W. M. Landing, P. L. Morton, B. A. Summers, C. S. Buck (2018) Concentrations, provenance and flux of aerosol trace elements during US GEOTRACES Western Arctic cruise GN01. Chem. Geol. doi:10.1016/j.chemgeo.2018.06.007.

Martin, J.H. and Knauer, G.A. (1980) Manganese cycling in northeast Pacific waters. Earth and Planetary Science Letters 51, 266-274.

Martin, J.H., Coale, K.H., Johnson, K.S., Fitzwater, S.E., Gordon, R.M., Tanner, S.J., Hunter, C.N., Elrod, V.A., Nowicki, J.L., Coley, T.L., Barber, R.T., Lindley, S., Watson, A.J., Van Scoy, K., Law, C.S., Liddicoat, M.I., Ling, R., Stanton, T., Stockel, J., Collons, C., Anderson, A., Bidigare, R.R., Ondrusek, M., Latasa, M., Millero, F.J., Lee, K., Yao, W., Zhang, J.Z., Friederich, G.E., Sakamato, C., Chavez, F.P., Buck, K., Kolber, Z., Greene, R., Falkowski, P.G., Chisholm, S.W., Hoge, F., Swift, R., Yungel, J., Turner, S., Nightingale, P.D., Hatton, A., Liss, P.S. and Tindale, N.W. (1994) Testing the iron hypothesis in ecosystems of the equatorial Pacific Ocean. Nature 371, 123-129.

Masumoto, Y., H. Sasaki, T. Kagimoto, N. Komori, et al., 2004: A fifty-year eddy-resolving simulation of the world ocean–Preliminary outcomes of OFES (OGCM for the Earth Simulator), J. Earth Simulator, 1, 35-56.

Moffett, J.W and C.R German (2018)- The US GEOTRACES Eastern Tropical Pacific Transect (GP16) Marine Chemistry, 201, 1-5. Doi.org/10.1016/j.marchem.2017.12.001.

Millero, F.J., Sotolongo, S. and Izaguirre, M. (1987) The oxidation kinetics of Fe(II) in seawater. Geochimica et Cosmochimica Acta 51, 793-801.

Nozaki, Y., J. Thomson and K.K. Turekian, (1976) The distribution of 210Pb and 210Po in the surface waters of the Pacific Ocean, Earth Planet. Sci. Lett. 32 , 304-312.

Ohnemus, D. C., Rauschenberg, S., Cutter, G. A., Fitzsimmons, J. N., Sherrell, R. M. and Twining, B. S. (2016) Elevated trace metal content of prokaryotic communities associated with marine oxygen deficient zones. Limnology and Oceanography, 62, 3-25, doi:10.1002/lno.10363.

Olsen, C.R., Larsen, I.L., Lowry, P.D., Cutshall, N.H., Todd, J.F., (1985). Atmospheric fluxes and marsh-soil inventories of 7Be and 210Pb. J. Geophys. Res. 90 (10), 487–495.

Owens, S. A., S. Pike, and K. O. Buesseler. (2015). Thorium- 234 as a tracer of particle dynamics and upper ocean export in the Atlantic Ocean. Deep-Sea Res., Part II 116: 42–59. doi:10.1016/j.dsr2.2014 .11.010.

Parker, C., Brown, M. and Bruland, K. (2016) Scandium in the open ocean: A comparison with other group 3 trivalent metals. Geophysical Research Letters 43, 2758-2764.

Peng, A., G. Liu, Z. Jiang, G. Liu, M. Liu (2019) Wet depositional fluxes of 7Be and 210Pb and their influencing factors at two characteristic cities of China. Applied Radiation and Isotopes, 147, 21-30.

Plattner, G.-K., N. Gruber, H. Frenzel, and J. C. McWilliams (2005), Decoupling marine export production from new production, Geophys. Res. Lett., 32, L11612, doi:10.1029/2005GL022660.

Rashan S. and J. Wu (2018) Dissolved and colloidal copper in the tropical South Pacific. Geochimica et Cosmochimica Acta. 233, 81–94.

Resing, J.A., P.N. Sedwick, C.R. German, W.J. Jenkins, J.W. Moffett, B.M. Sohst, and A. Tagliabue (2015): Basin-scale transport of hydrothermal dissolved metals across the South Pacific Ocean. Nature, 523, 200–203, doi: 10.1038/nature14577.

Sanial, V., L.E. Kipp, P.B.Henderson, P.van Beek, J.-L. Reyss, D.E. Hammond, N.J. Hawco, M.A. Saito, J.A. Resing, P. Sedwick, W.S. Moore, M.A. Charette (2018) Radium-228 as a tracer of dissolved trace element inputs from the Peruvian continental margin. Mar. Chem. 201, 20-34.

Shiller, A.M., (1997). Manganese in surface waters of the Atlantic Ocean. Geophysical Res. Lett. 24, 1495–1498

Schlitzer, R., Anderson, R.F., Dodas, E.M., Lohan, M., Geibert, W., Tagliabue, A., Bowie, A., Jeandel, C., Maldonado, M.T., Landing, W.M., Cockwell, D., Abadie, C., Abouchami, W., Achterberg, E.P., Agather, A., Aguliar-Islas, A., van Aken, H.M., Andersen, M., Archer, C., Auro, M., de Baar, H.J., Baars, O., Baker, A.R., Bakker, K., Basak, C., Baskaran, M., Bates, N.R., Bauch, D., van Beek, P., Behrens, M.K., Black, E., Bluhm, K., Bopp, L., Bouman, H., Bowman, K., Bown, J., Boyd, P., Boye, M., Boyle, E.A., Branellec, P., Bridgestock, L., Brissebrat, G., Browning, T., Bruland, K.W., Brumsack, H.-J., Brzezinski, M., Buck, C.S., Buck, K.N., Buesseler, K., Bull, A., Butler, E., Cai, P., Mor, P.C., Cardinal, D., Carlson, C., Carrasco, G., Casacuberta, N., Casciotti, K.L., Castrillejo, M., Chamizo, E., Chance, R., Charette, M.A., Chaves, J.E., Cheng, H., Chever, F., Christl, M., Church, T.M., Closset, I., Colman, A., Conway, T.M., Cossa, D., Croot, P., Cullen, J.T., Cutter, G.A., Daniels, C., Dehairs, F., Deng, F., Dieu, H.T., Duggan, B., Dulaquais, G., Dumousseaud, C., Echegoyen-Sanz, Y., Edwards, R.L., Ellwood, M., Fahrbach, E., Fitzsimmons, J.N., Russell Flegal, A., Fleisher, M.Q., van de Flierdt, T., Frank, M., Friedrich, J., Fripiat, F., Fröllje, H., Galer, S.J.G., Gamo, T., Ganeshram, R.S., Garcia-Orellana, J., Garcia-Solsona, E., Gault-Ringold, M., George, E., Gerringa, L.J.A., Gilbert, M., Godoy, J.M., Goldstein, S.L., Gonzalez, S.R., Grissom, K., Hammerschmidt, C., Hartman, A., Hassler, C.S., Hathorne, E.C., Hatta, M., Hawco, N., Hayes, C.T., Heimbürger, L.-E., Helgoe, J., Heller, M., Henderson, G.M., Henderson, P.B., van Heuven, S., Ho, P., Horner, T.J., Hsieh, Y.-T., Huang, K.-F., Humphreys, M.P., Isshiki, K., Jacquot, J.E., Janssen, D.J., Jenkins, W.J., John, S., Jones, E.M., Jones, J.L., Kadko, D.C., Kayser, R., Kenna, T.C., Khondoker, R., Kim, T., Kipp, L., Klar, J.K., Klunder, M., Kretschmer, S., Kumamoto, Y., Laan, P., Labatut, M., Lacan, F., Lam, P.J., Lambelet, M., Lamborg, C.H., Le Moigne, F.A.C., Le Roy, E., Lechtenfeld, O.J., Lee, J.-M., Lherminier, P., Little, S., López-Lora, M., Lu, Y., Masque, P., Mawji, E., McClain, C.R., Measures, C., Mehic, S., Barraqueta, J.-L.M., van der Merwe, P., Middag, R., Mieruch, S., Milne, A., Minami, T., Moffett, J.W., Moncoiffe, G., Moore, W.S., Morris, P.J., Morton, P.L., Nakaguchi, Y., Nakayama, N., Niedermiller, J., Nishioka, J., Nishiuchi, A., Noble, A., Obata, H., Ober, S., Ohnemus, D.C., van Ooijen, J., O'Sullivan, J., Owens, S., Pahnke, K., Paul, M., Pavia, F., Pena, L.D., Peters, B., Planchon, F., Planquette, H., Pradoux, C., Puigcorbé, V., Quay, P., Queroue, F., Radic, A., Rauschenberg, S., Rehkämper, M., Rember, R., Remenyi, T., Resing, J.A., Rickli, J., Rigaud, S., Rijkenberg, M.J.A., Rintoul, S., Robinson, L.F., Roca-Martí, M., Rodellas, V., Roeske, T., Rolison, J.M., Rosenberg, M., Roshan, S., Rutgers van der Loeff, M.M., Ryabenko, E., Saito, M.A., Salt, L.A., Sanial, V., Sarthou, G., Schallenberg, C., Schauer, U., Scher, H., Schlosser, C., Schnetger, B., Scott, P., Sedwick, P.N., Semiletov, I., Shelley, R., Sherrell, R.M., Shiller, A.M., Sigman, D.M., Singh, S.K., Slagter, H.A., Slater, E., Smethie, W.M., Snaith, H., Sohrin, Y., Sohst, B., Sonke, J.E., Speich, S., Steinfeldt, R., Stewart, G., Stichel, T., Stirling, C.H., Stutsman, J., Swarr, G.J., Swift, J.H., Thomas, A., Thorne, K., Till, C.P., Till, R., Townsend, A.T., Townsend, E., Tuerena, R., Twining, B.S., Vance, D., Velazquez, S., Venchiarutti, C., Villa-Alfageme, M., Vivancos, S.M., Voelker, A.H.L., Wake, B., Warner, M.J., Watson, R., van Weerlee, E., Alexandra Weigand, M., Weinstein, Y., Weiss, D., Wisotzki, A., Woodward, E.M.S., Wu, J., Wu, Y., Wuttig, K., Wyatt, N., Xiang, Y., Xie, R.C., Xue, Z., Yoshikawa, H., Zhang, J., Zhang, P., Zhao, Y., Zheng, L., Zheng, X.-Y., Zieringer, M., Zimmer, L.A., Ziveri, P., Zunino, P. and Zurbrick, C. (2018) The GEOTRACES Intermediate Data Product 2017. Chemical Geology 493, 210-223.

Scholz, F., Hensen, C., Noffke, A., Rohde, A., Liebetrau, V., & Wallmann, K. (2011). Early diagenesis of redox-sensitive trace metals in the Peru upwelling area—Response to ENSO-related oxygen fluctuations in the water column. Geochimica et Cosmochimica Acta, 75(22), 7257–7276. https://doi.org/10.1016/j.gca. 2011.08.007.

Scholz, F., Severmann, S., McManus, J. and Hensen, C. (2014) Beyond the Black Sea paradigm: The sedimentary fingerprint of an open-marine iron shuttle. Geochimica et Cosmochimica Acta 127, 368-380.

Shelley, R. U., Roca-Martí, M., Castrillejo, M., Sanial, V., Masqué, P., Landing, W. M., van Beek, P., Planquette, H., and Sarthou, G. (2017) Quantification of trace element atmospheric deposition fluxes to the Atlantic Ocean (> 40 N; GEOVIDE, GEOTRACES GA01) during spring 2014, Deep-Sea Res. Pt I, 119, 34–49, https://doi.org/10.1016/j.dsr.2016.11.010.

Shelley, R.U., Landing, W.M., Ussher, S.J., Planquette, H. and Sarthou, G. (2018) Regional trends in the fractional solubility of Fe and other metals from North Atlantic aerosols (GEOTRACES cruises GA01 and GA03) following a two-stage leach. Biogeosciences 15, 2271-2288.

Twining, B. S. B., and S. B. S. Baines. 2013. The trace metal composition of marine phytoplankton. Annu. Rev. Mar. Sci. 5: 191–215. doi:10.1146/annurev-marine-121211-172322.

Uematsu, M., R. A. Duce and J. M. Prospero (1994) Atmosphere beryllium-7 concentrations over the Pacific Ocean. Geophy. Res. Lett. 21, 561-564.

Wagener, T., Guieu, C., Losno, R., Bonnet, S. and Mahowald, N. (2008) Revisiting atmospheric dust export to the Southern Hemisphere ocean: Biogeochemical implications. Global Biogeochem. Cycles 22, GB2006.

Young, J. A., and W. B. Silker (1980), Aerosol deposition velocities on the Pacific and Atlanic Oceans calculated from 7Be measurements, Earth Planet. Sci. Lett., 50, 92–104, doi:10.1016/ 0012-821X(80)90121-1

Wu, J., Roshan, S., & Chen, G. (2014). The distribution of dissolved manganese in the tropical–subtropical North Atlantic during US GEOTRACES 2010 and 2011 cruises. Marine Chemistry, 166, 9–24. doi:10.1016/j.marchem.2014.08.007.

Zheng, L., Minami, T., Konagaya, W., Chan, C.-Y., Tsujisaka, M., Takano, S., Norisuye, K., Sohrin, Y. (2019). Distinct basin-scale-distributions of aluminum, manganese, cobalt, and lead in the North Pacific Ocean. Geochimica et Cosmochimica Acta, 254, 102–121. DOI: http://doi.org/10.1016/J. GCA. 2019. 03.038

Supplemental Figure 1. $^{7}$Be profiles and plot of eqn. 5 for stations 26-36. The derived Kz is indicated. The horizontal line indicates base of the mixed layer. The vertical dashed line indicates mixed layer $^{7}$Be activity.

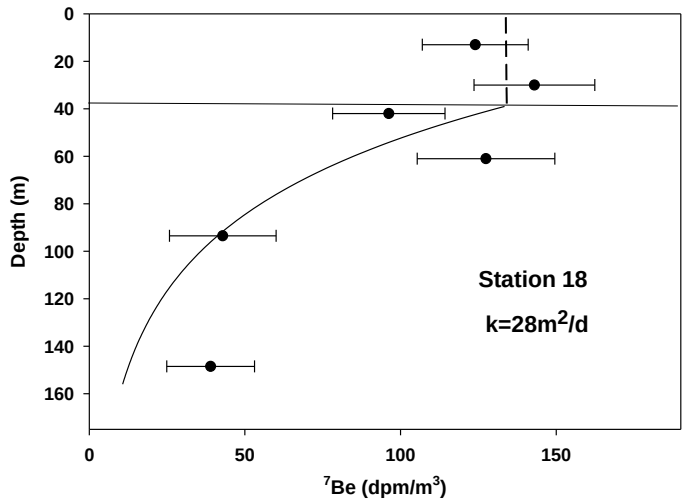


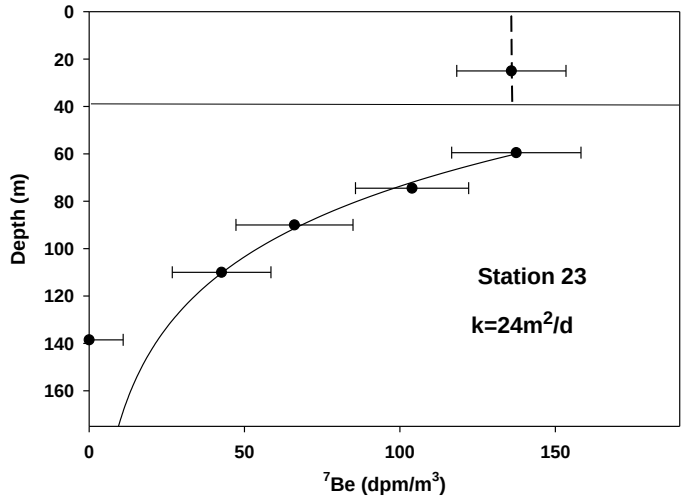


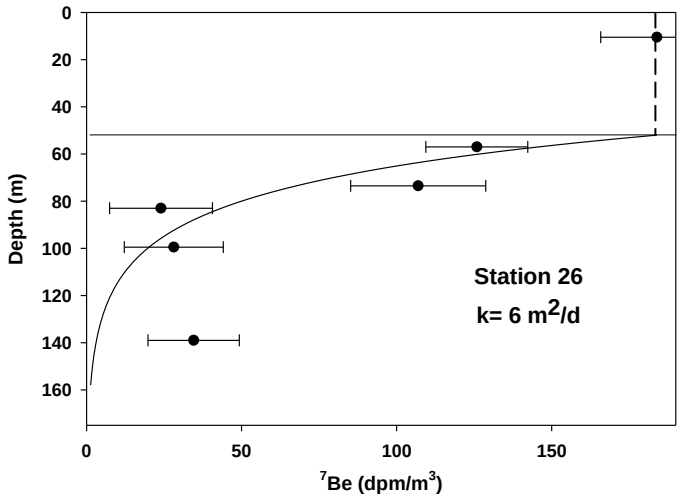

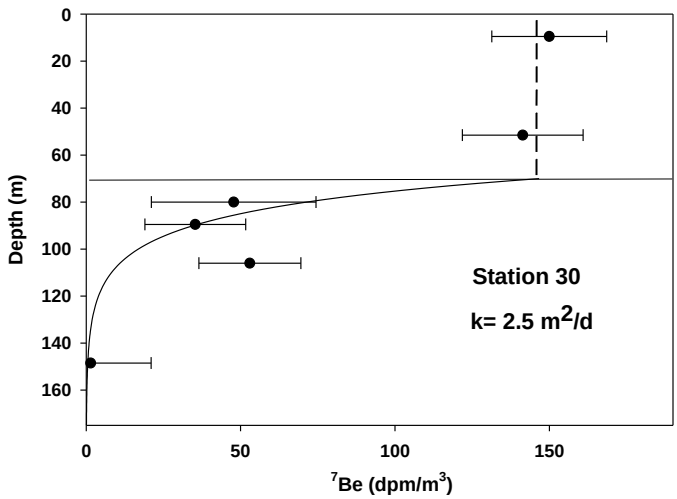
Depth (m)
0
20
40
60
80
100
120
140
160
0
50
100
150
$^7$Be (dpm/m$^3$)
Station 30
k= 2.5 m$^2$/d

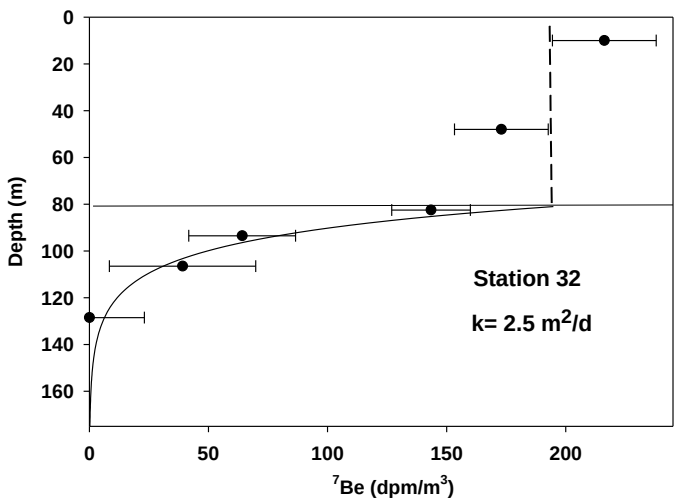
Depth (m)
0
20
40
60
80
100
120
140
160
0
50
100
150
200
$^7$Be (dpm/m$^3$)
Station 32
k= 2.5 m$^2$/d

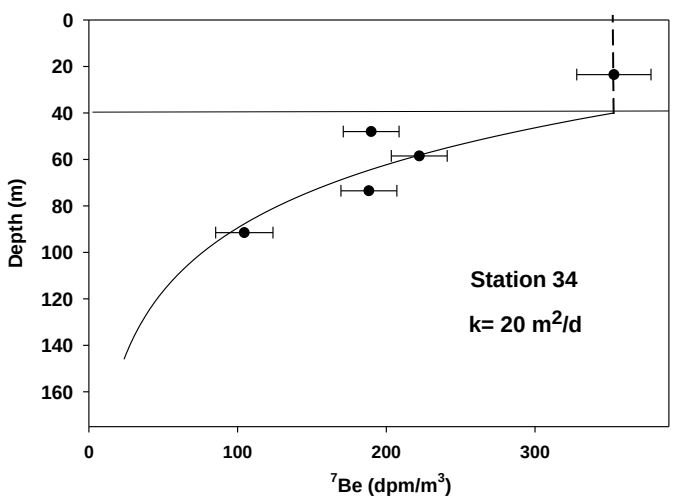
Depth (m)
0
20
40
60
80
100
120
140
160
0
100
200
300
$^7$Be (dpm/m$^3$)
Station 34
k= 20 m$^2$/d

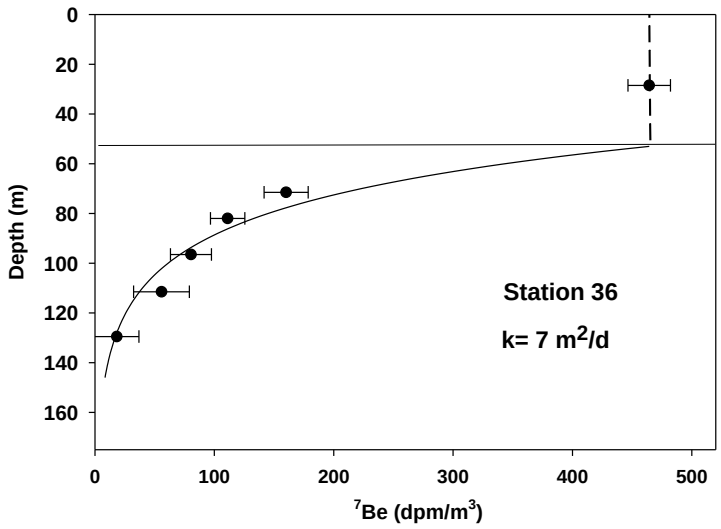


Supplemental Figure 2

Left: $^{7}$Be, density, and fluorescence profiles. Right: Selected TE concentration profiles. The solid horizontal line indicates the mixed layer depth. The dashed horizontal line indicates the depth of the PPZ.

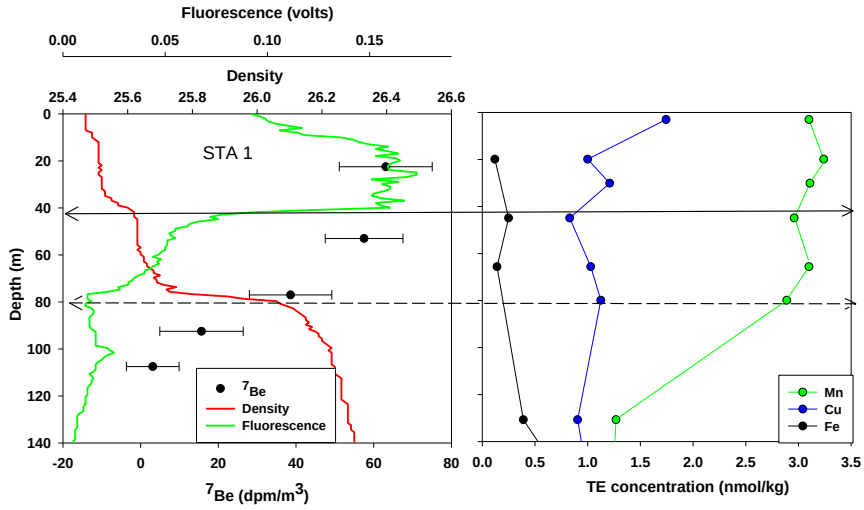


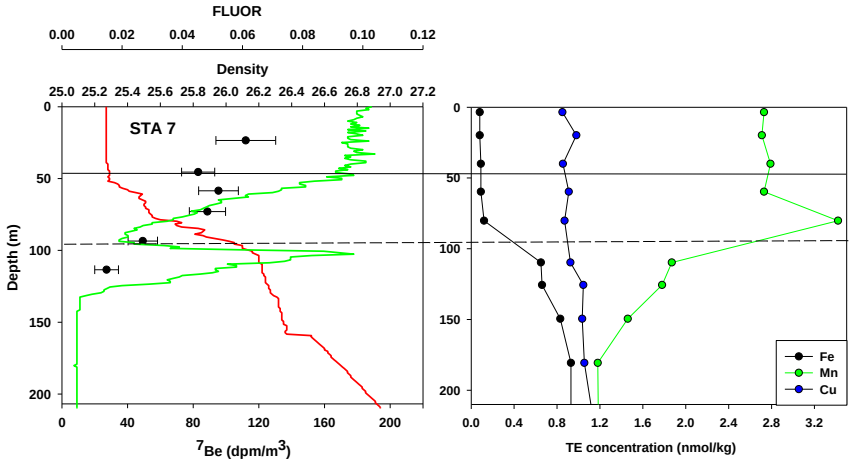

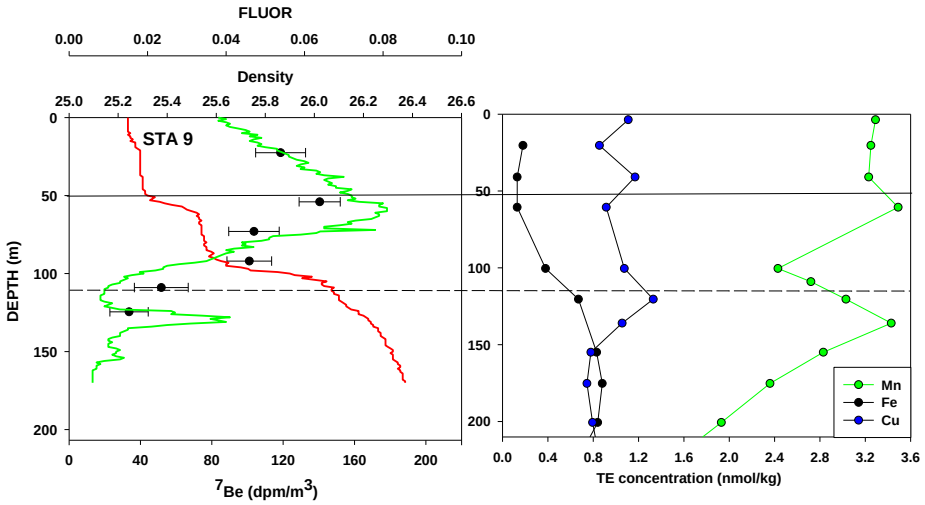


1004

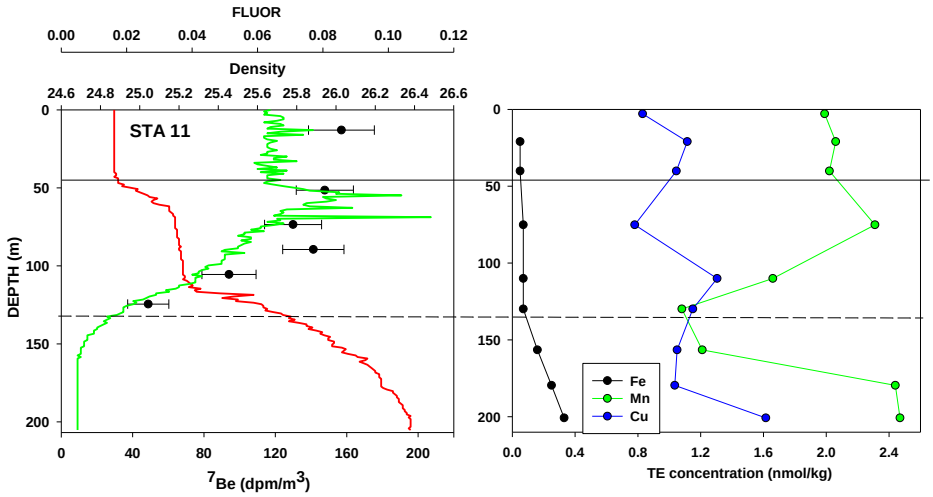


1005

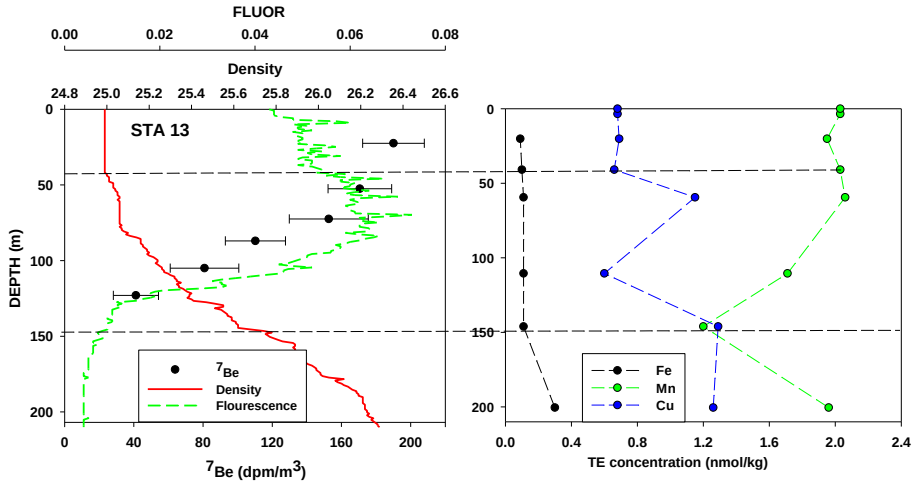


1006

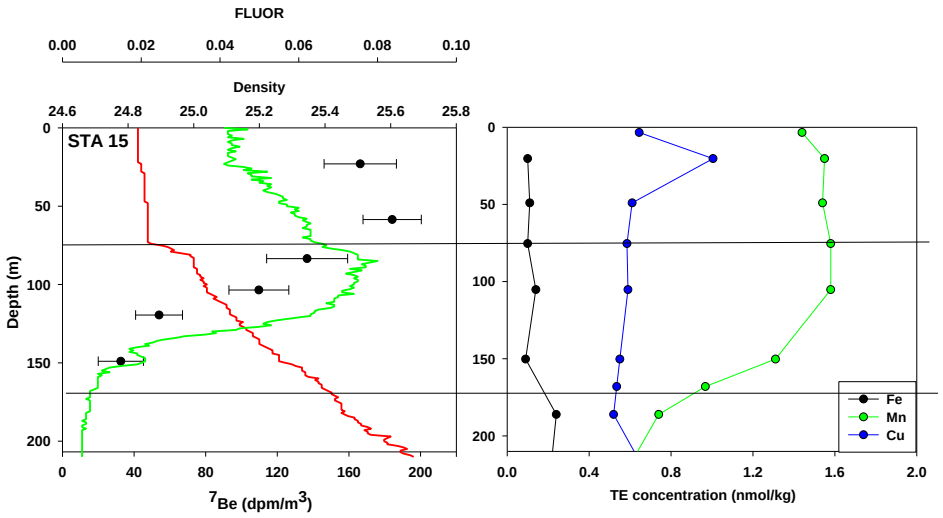


1007

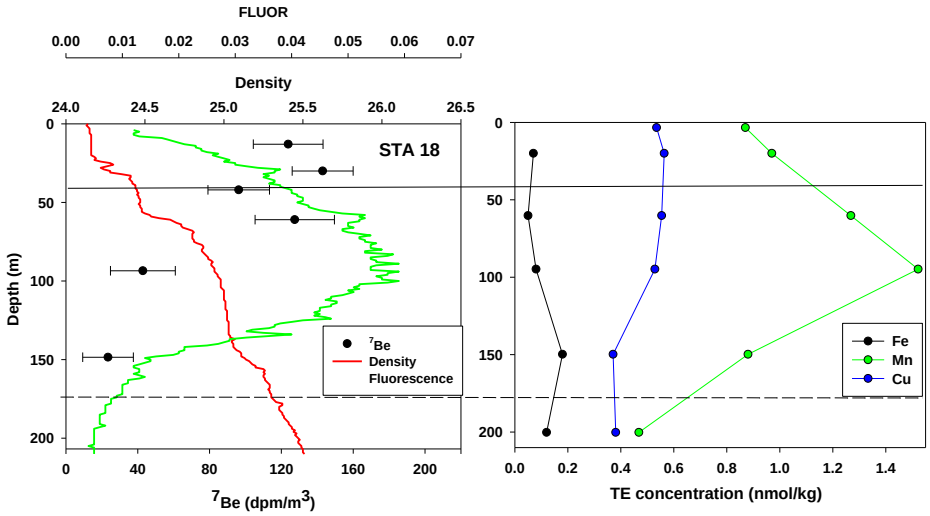


1008

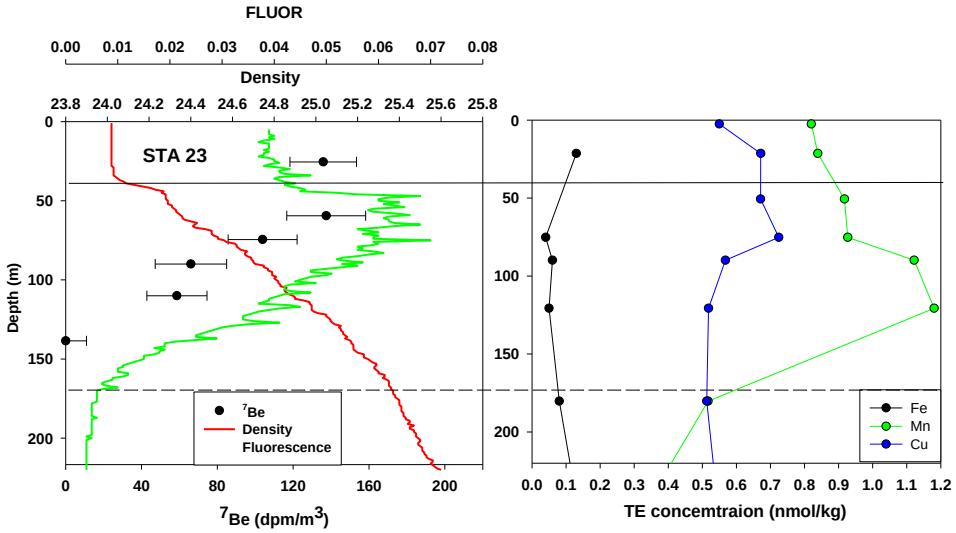


1009

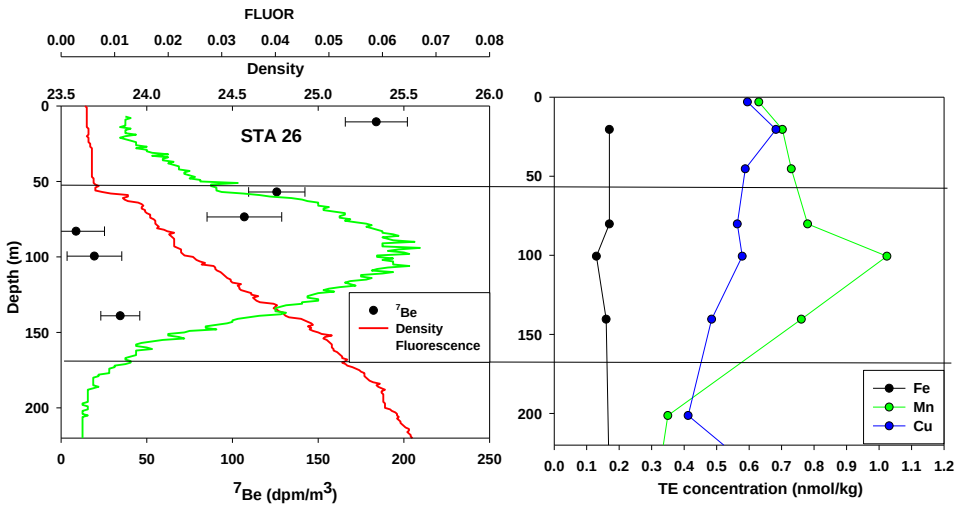


1010

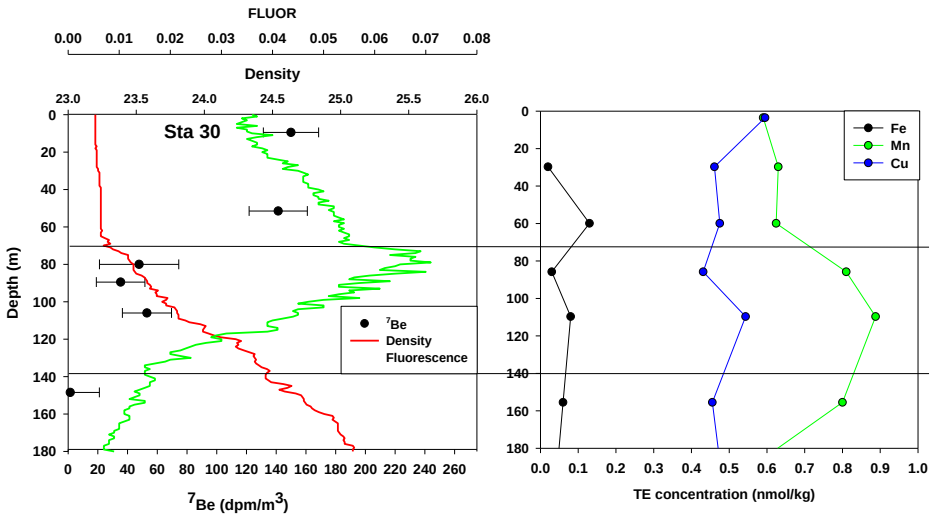


1011

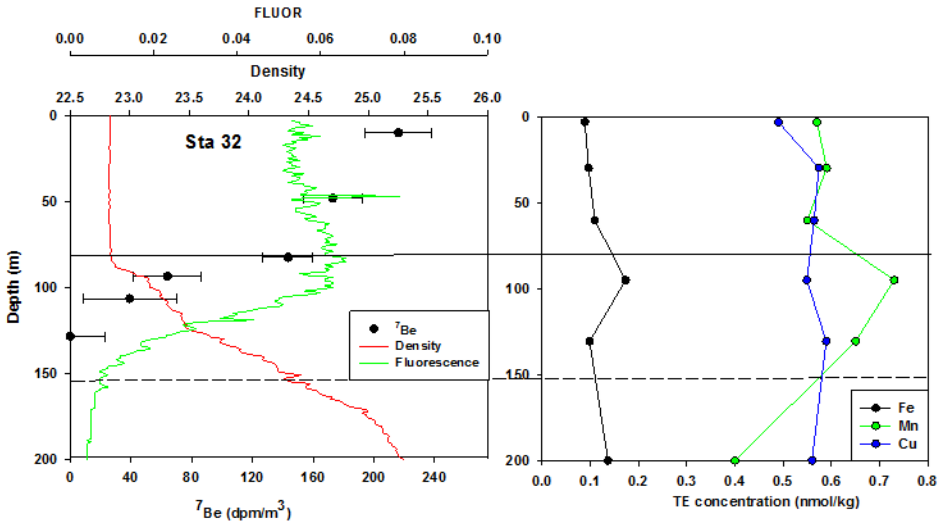


1012

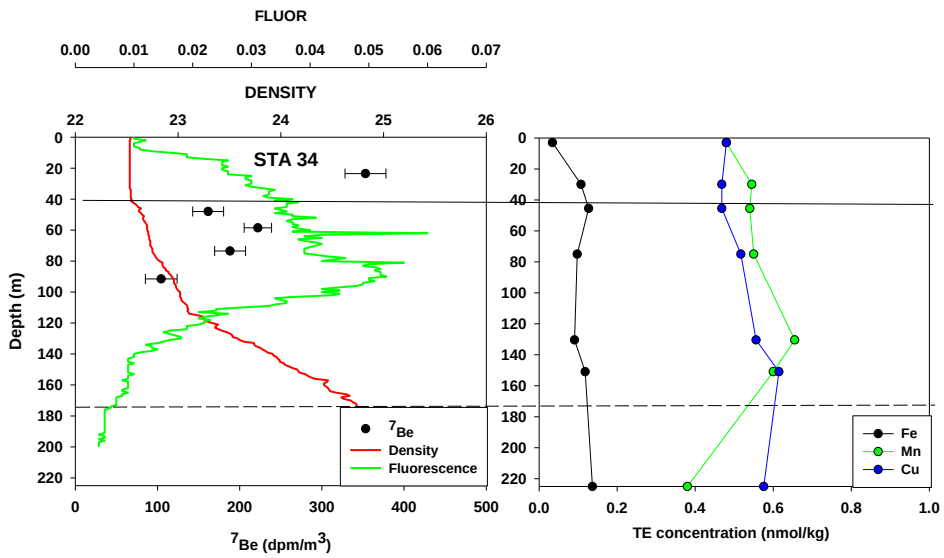
FLUOR
DENSITY
STA 34
Depth (m)
7Be
Density
Fluorescence
7Be (dpm/m3)
Fe
Mn
Cu
TE concentration (nmol/kg)

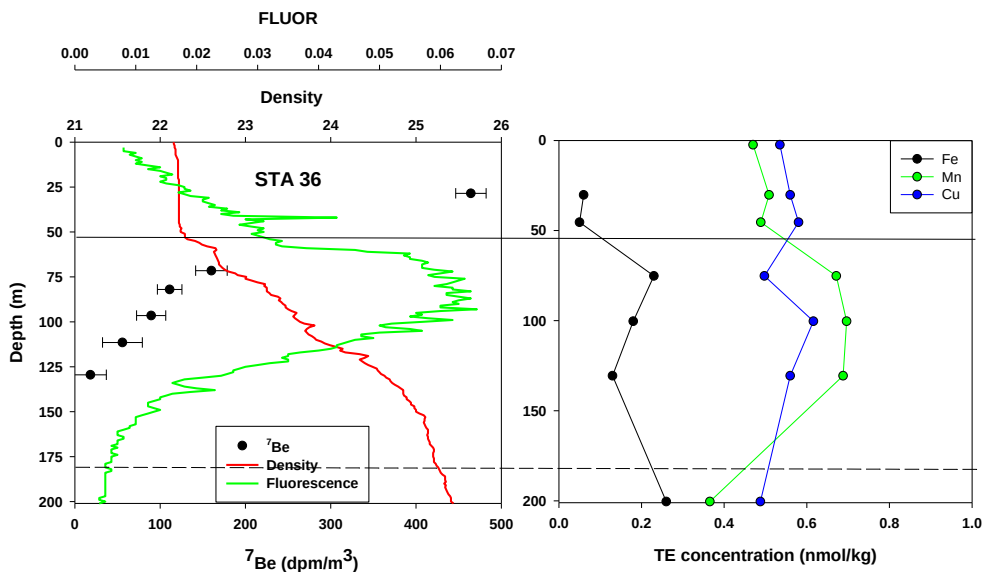
FLUOR
Density
STA 36
Depth (m)
7Be
Density
Fluorescence
7Be (dpm/m3)
Fe
Mn
Cu
TE concentration (nmol/kg)

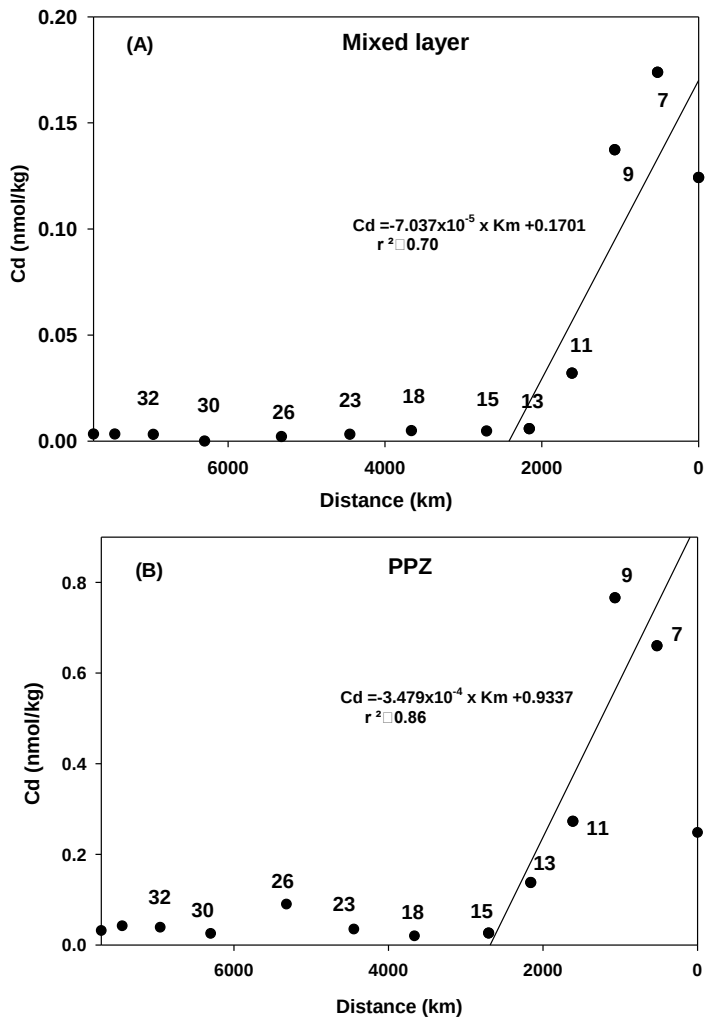


Supplemental Figure 3.

A) Dissolved Cd plotted against distance from station 1 for the mixed layer across the EPZT.

B) Dissolved Cd plotted against distance from station 1 for the PPZ across the EPZT.

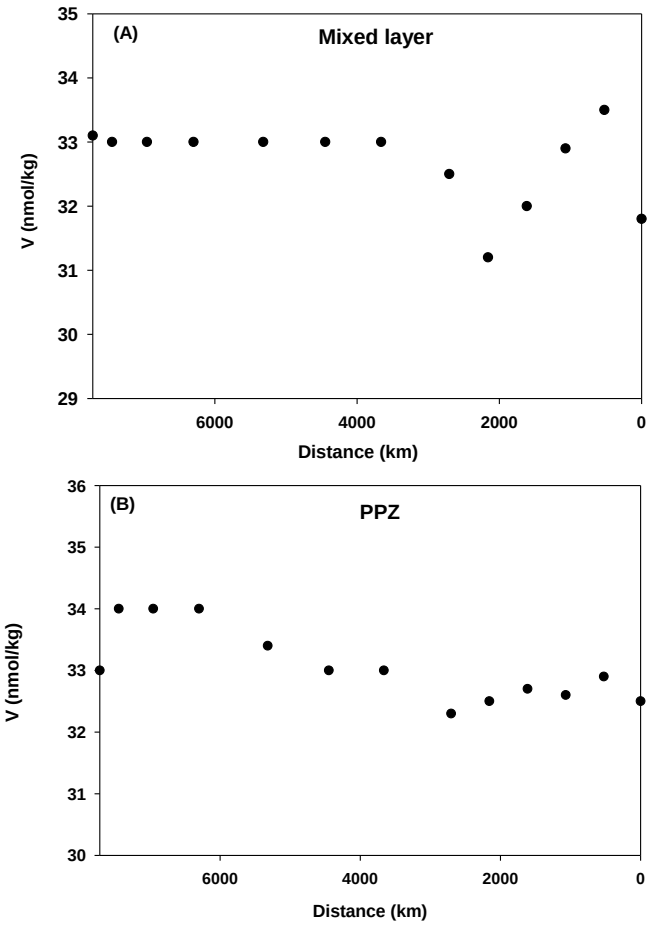


Supplemental Figure 4.

A) Dissolved V plotted against distance from station 1 for the mixed layer across the EPZT.

B) Dissolved V plotted against distance from station 1 for the PPZ across the EPZT.

Supplemental Table 1a. Cd and V fluxes into the mixed layer

| | Cd ML Flux (nmol/m²/d) | | | | | V ML Flux (nmol/m²/d) | | | |
|---|---|---|---|---|---|---|---|---|---|
| STATION | Diffusive | Upwelling | Atmosphere (BULK) | Horizontal | | Diffusive | Upwelling | Atmosphere (BULK) | Horizontal |
| 1 | 154 | 682 | 0.45 | 0 | | -182 | 143440 | 8.21 | 0 |
| 7 | -25.4 | 161.2 | 0.45 | 28 | | -593 | 43160 | 8.21 | 0 |
| 9 | 138 | 319.5 | 0.45 | 32 | | -828 | 48900 | 8.21 | 0 |
| 11 | 19.4 | 1.19 | 0.45 | 27 | | 250 | 1280 | 8.21 | 0 |
| 13 | -1.0 | -0.81 | 0.45 | 26 | | 1015 | -3900 | 8.21 | 0 |
| 15 | 2.4 | 0.44 | 0.45 | 44 | | 0.0 | 4950 | 8.21 | 0 |
| 18 | -1.1 | 0 | 0.03 | 24 | | 0.0 | 0 | 0.35 | 0 |
| 23 | 7.9 | 0 | 0.04 | 0 | | 0.0 | 0 | 0.36 | 0 |
| 26 | -3.4 | 0 | 0.04 | 0 | | 170 | 0 | 0.42 | 0 |
| 30 | 0.2 | 0 | 0.04 | 0 | | 0.0 | 0 | 0.42 | 0 |
| 32 | -0.4 | 0 | 0.05 | 0 | | 142.5 | 0 | 0.51 | 0 |
| 34 | -2.2 | 0 | 0.07 | 0 | | 0.0 | 0 | 0.77 | 0 |
| 36 | 1.0 | 0 | 0.10 | 0 | | 378 | 0 | 0.98 | 0 |

| Supplemental Table 1b. Cd and V fluxes into the PPZ | | | | | | | | | |
|---|---|---|---|---|---|---|---|---|---|
| | | Cd PPZ Flux (nmol/m²/d) | | | | | V PPZ Flux (nmol/m²/d) | | |
| STATION | Diffusive | Upwelling | Atmosphere (BULK) | Horizontal | | Diffusive | Upwelling | Atmosphere (BULK) | Horizontal |
| 1 | 1971 | 818 | 0.45 | 0 | | 1862 | 107250 | 8.21 | 0 |
| 7 | 308 | 495 | 0.45 | 101 | | 0.0 | 24675 | 8.21 | 0 |
| 9 | -85.8 | 521 | 0.45 | 119 | | -294.5 | 22170 | 8.21 | 0 |
| 11 | 88.2 | 1.365 | 0.45 | 157 | | -764 | 163.5 | 8.21 | 0 |
| 13 | 220.5 | -1 | 0.45 | 184 | | 44.1 | -228 | 8.21 | 0 |
| 15 | 31.2 | 0 | 0.45 | 188 | | 143.0 | 323 | 8.21 | 0 |
| 18 | 9.5 | 0 | 0.03 | 0.0 | | -1070 | 0 | 0.35 | 0 |
| 23 | 8.6 | 0 | 0.04 | 0.0 | | 0.0 | 0 | 0.36 | 0 |
| 26 | 5.6 | 0 | 0.04 | 0.0 | | 111.6 | 0 | 0.42 | 0 |
| 30 | -0.1 | 0 | 0.04 | 0.0 | | 0.0 | 0 | 0.42 | 0 |
| 32 | 1.1 | 0 | 0.05 | 0.0 | | -53.3 | 0 | 0.51 | 0 |
| 34 | 5.6 | 0 | 0.07 | 0.0 | | -400.0 | 0 | 0.77 | 0 |
| 36 | 2.7 | 0 | 0.10 | 0.0 | | -98.0 | 0 | 0.98 | 0 |

| Supplemental Table 2. Mixed layer and PPZ Cd and V inventories (nmol/m²) | | | | |
|---|---|---|---|---|
| STATION | Cd ML inv | Cd PPZ inv | V ML inv | V PPZ inv |
| 1 | 5720 | 10450 | 1363000 | 2131000 |
| 7 | 6140 | 20760 | 1510000 | 3106000 |
| 9 | 8290 | 38780 | 1704000 | 3590000 |
| 11 | 1250 | 10630 | 1412000 | 4200000 |
| 13 | 241 | 4340 | 1306000 | 4762000 |
| 15 | 206 | 1500 | 2450000 | 5491000 |
| 18 | 158 | 1090 | 1287000 | 5742000 |
| 23 | 238 | 3120 | 1287000 | 5639300 |
| 26 | 523 | 5060 | 1717000 | 5641000 |
| 30 | 328 | 1610 | 1977000 | 4568100 |
| 32 | 871 | 2710 | 2647000 | 5048000 |
| 34 | 194 | 2770 | 1320000 | 5847300 |
| 36 | 187 | 1840 | 1731000 | 5891000 |

| Supplemental Table 3. Mixed layer and PPZ Cd and V Residence Times | | | | | | | | |
|---|---|---|---|---|---|---|---|---|
| | Mixed Layer Residence Times (d) | | | | PPZ Residence Times (d) | | | |
| | **Cd** | **Cd** | **V** | **V** | **Cd** | **Cd** | **V** | **V** |
| STATION | HAc[a] | DI[b] | HAc[c] | DI | HAc[a] | DI[d] | HAc[c] | DI[d] |
| 1 | 7 | 7 | 9.5 | 9.5 | 4 | 4 | 19.5 | 19.5 |
| 7 | 32 | 31 | 35.0 | 35.0 | 23 | 23 | 12.6 | 12.6 |
| 9 | 17 | 17 | 34.8 | 34.8 | 61 | 61 | 162 | 162 |
| 11 | 26 | 26 | 920 | 920 | 43 | 43 | 24800 | 24990 |
| 13 | 9 | 9 | 1280 | 1282 | 11 | 11 | 96470 | 99115 |
| 15 | 4.4 | 4.4 | 494 | 495 | 6.8 | 6.8 | 11650 | 11680 |
| 18 | 7 | 7 | 5631150 | 7463250 | 115 | 115 | 25123605 | 33297570 |
| 23 | 30 | 30 | 5474730 | 7255940 | 361 | 362 | 23988855 | 31793630 |
| 26 | 13620 | 20115 | 10084 | 10090 | 897 | 899 | 50240 | 50270 |
| 30 | 1376 | 1451 | 7208490 | 9553770 | 41971 | 62000 | 16656090 | 22075150 |
| 32 | 18150 | 26800 | 18530 | 18540 | 2361 | 2393 | 15157790 | 20089380 |
| 34 | 2887 | 4264 | 262525 | 347940 | 489 | 491 | 11629240 | 15412820 |
| 36 | 171 | 176 | 4570 | 4574 | 657 | 664 | 9205550 | 12200580 |

a. Cd HAc solubility is 96%
b. Cd DI solubility is 65%
c. V HAc solubility is 65.3%
d. V DI solubility is 49.3%